Modeling of the Effects of Wave-Induced Fluid Motion on Seismic Velocity and Attenuation in Porous Rocks

by

Yang Zhang

B.S., Geology (2000)
Peking University
M.S., Geology (2003)
Peking University

Submitted to the Department of Earth, Atmospheric and Planetary Sciences
in partial fulfillment of the requirements for the degree of

Doctor of Philosophy in Geophysics

at the

MASSACHUSETTS INSTITUTE OF TECHNOLOGY

September 2010

Author .....
Department of Earth, Atmospheric and Planetary Sciences
September 7, 2010

Certified by .....
M. Nafi Toksöz
Professor of Geophysics
Thesis Supervisor

Accepted by .....
Maria T. Zuber
E.A. Griswold Professor of Geophysics
Head of the Department

Modeling of the Effects of Wave-Induced Fluid Motion on Seismic Velocity and Attenuation in Porous Rocks

by

Yang Zhang

Submitted to the Department of Earth, Atmospheric and Planetary Sciences
on September 7, 2010, in partial fulfillment of the
requirements for the degree of
Doctor of Philosophy in Geophysics

Abstract

In this thesis, we use the X-ray CT images of Berea sandstones to carry out the numerical study of the effects of wave-induced fluid motion on seismic velocity and attenuation in porous rocks. In numerical modeling, it is possible to control the factors and inputs that are hard to accomplish in laboratory measurements and isolate those of interest that have significant impact on the seismic responses; this can help in understanding the fundamental physics of seismic waves propagating in saturated porous rocks. The ultimate goal of computational rock physics is to supplement the traditional laboratory measurements, that are time consuming and costly, with cheaper numerical experiments that allow the parameter space to be explored more thoroughly.

For this purpose, in this thesis we develop a computational method for time domain simulation of wave propagation in poroelastic medium. The medium is composed of an elastic matrix saturated with a Newtonian fluid. The method operates on a digitized representation of the medium where a distinct material phase and properties are specified at each volume cell. The dynamic response to an acoustic excitation is modeled mathematically with a coupled system of equations: elastic wave equation in the solid matrix and linearized Navier-Stokes equation in the fluid. Implementation of the solution is simplified by introducing a common numerical form for both solid and fluid cells and using a rotated-staggered-grid finite-difference scheme which allows stable solutions without explicitly handling the fluid-solid boundary conditions. A stability analysis is incorporated and can be used to select gridding and time step size as a function of material properties. The numerical results are shown to agree with the analytical solution for an idealized porous medium of periodically alternating solid and fluid layers.

When applying the linear solver to compute the effective elastic properties of 3D digitized porous rocks, we find discrepencies between the numerical results and the laboratory measurements. The reason for such a problem is the loss of small features, such as cracks and micro-pores, in the digitized matrix of rocks during the imaging process of aggregation. A hybrid approach, combining the numerical computation

and the effective media theories, is developed to deduce the lost cracks from a limited number of laboratory measurements. This approach can recover the lost cracks and is capable of predicting the effective elastic properties of the rock matrix. Compared to the traditional inversion schemes based only on the effective media theories, this hybrid scheme has the advantage of utilizing the complex micro-structures of 3D digitized porous rocks that are resolved in the imaging process, and it helps limit the inversion space for crack distribution.

In the study of the dynamic and low-frequency responses of saturated porous rocks, we employ the stress-strain calculation in numerical modeling so as to compute the velocities and attenuations of rock samples, the sizes of which are much smaller than the seismic wavelength of interest. For these cases, transmission measurement cannot be used. Realizing the significant contribution of small cracks to the total attenuation, we extend the hybrid approach by incorporating the modified squirt-flow model where a fluid with frequency-dependent bulk modulus is introduced. Therefore, attenuation due to viscous fluid in stiff pores, that are resolved in the imaging process, can be computed numerically. Attenuation due to viscous fluid in compliant pores can be determined by the modified squirt-flow model since we know the crack distribution. In the inversion for crack distribution, besides using the velocities of P- and S-waves measured in laboratory for the dry and water-saturated cases, measured attenuation data of P-waves are also used so as to further constrain the inversion, and to improve the uniqueness of the inversion results. By using such an extended hybrid approach, we are able to predict both the velocities of saturated porous rocks and the attenuations.

From numerical study with the linear solver, we can conclude that the linear solver is able to accurately couple elastic solid and viscous fluid and handle high material contrast and the complex micro-structures of 3D digitized porous rocks. The stress-strain calculation is capable of computing the velocities and attenuations of saturated porous rocks the sizes of which are much smaller than the wavelength of interest. The hybrid approach is a practical way to study the seismic properties of saturated porous rocks until high enough resolution digitized data and enough computational resources are available. From the computations, we observe that the small features, such as cracks lost in the imaging process, are critical for accurately predicting velocities and attenuations of saturated porous rocks. Generally, attenuation is more sensitive to the viscosity of the saturating fluid than velocity is, and attenuation due to viscous fluid in compliant pores is greater than that due to viscous fluid in stiff pores.

Thesis Supervisor: M. Nafi Toksöz
Title: Professor of Geophysics

Acknowledgments

During the past seven years of my studying at MIT, I have been going through many ups and downs in my life. There are many people I would like to thank for their support and understanding.

First of all, I would like to thank my advisor, Prof. M. Nafi Toksöz. He is a good academic advisor and an excellent educator as well. He really provides an environment with much academic freedom for students such that I am able to choose an interesting thesis topic by myself, reach people outside to collaborate on my research and take courses other than those only related to my research. Whenever I got into trouble regarding to my research, he was always there for giving help and support.

I also would like to thank Dr. Feng Shen, my former advisor in Peking University when I was pursing my master degree there. She is a good academic advisor who always keeps my needs and problems in mind and considers them as her first priority. Her good attitude to work influences me in a profound way, from which I have learned to work hard and pursue the excellence as possible as I can. She is also a very good friend of mine who gives me valuable suggestions and advices that make my life at MIT much easier. Without her support and guidence, I do not think I can achieve the accomplishment so far.

I would like to give my grateful thanks to Chin-Wu Chen and Taiwei Wang, the roommates of mine for most of my life as a graduate student at MIT. I will never forget the men's talks we had gone through and the trips we had done together during these years. The valuable memory of my life at 9B of Tang Hall with you two is the fortune that I need to carefully protect in the rest of my life. Especially thank you two for being with me during the summer of 2010 when I was at the lowest point of my life. I believe the legend of 9B will be going on forever.

I also would like to thank my thesis committee members: Prof. F. Dale Morgan, Dr. William B. Durham, Prof. Bradford Hager, Dr. Michael Prange and Prof. John R. Williams for their valuable suggestions and efforts to make my thesis defense possible in such short time.

I would like to thank Schlumberger-Doll Research for funding my research and ERL Founding Member Consortium for supporting me during these years.

I would like to thank my colleagues and friends at ERL, EAPS and MIT, and friends in Boston and US for their encouragement and help.

Especially, I would like to give my sincere thanks to my parents, family and friends in China for their support and undstanding in the past years.

To all I love and all loving me

Contents

List of Figures

List of Tables

Chapter 1

Introduction

1.1 Objective

The goal of this thesis is to understand the fundamental physics of seismic velocity dispersion and attenuation of porous rocks saturated with viscous fluids by using high resolution digitized sandstones and high-performance computational techniques. This thesis focuses on the dynamic and low-frequency responses of the saturated porous rocks due to wave-induced fluid motion in the pores.

To accomplish this, we have to first develop a multi-physics numerical solver to couple the wave equation in solid grains with the fluid flow of viscous fluids in the pores. This solver has to be able to handle the high material contrast and complex micro-structures of digitized porous rocks, accurately capture the interaction between elastic solid and viscous fluid and be parallelized so as to efficiently deal with large samples. Second, observing the discrepancies between the computed results and laboratory measurements due to ignoring the discontinuities such as cracks in the matrix of rocks, we need to find a solution to resolve this general problem of computing the static and dynamic effective elastic properties of saturated porous rocks by including these cracks lost in the imaging process. We need to develop a framework that combines the computational techniques and theoretical models to take the advantage of the high resolution digitized data that describe the complex micro-structures of porous rocks, while including the effects of lost cracks through the use of effective

medium models, such as the Kuster-Toksöz model. Third, in studying the dynamic and low-frequency responses of saturated porous rock, since the rock samples we can simulate are much smaller than the wavelengths in which we are interested, we have to develop a numerical calculation to extract the velocity and attenuation information from the computed results. We utilize the idea of the stress-strain calculation in our numerical modeling for this purpose. When considering the dynamic responses of saturated porous rocks in terms of attenuation, the contribution of cracks comes into play in a significant way. To compensate for its contribution to the total attenuation, we have to introduce another theoretical model — the modified squirt-flow model, and combine it with the numerically computed results so as to provide a good explanation of the observations in laboratory measurements.

Overall, this thesis introduces a multi-physics numerical solver and a framework to study the effects of wave-induced fluid motion on seismic velocity and attenuation in saturated porous rocks. The framework combines the numerical computation with the theoretical models so as to compensate for the contribution of cracks lost in the imaging process. The thesis demonstrates the merits of the framework for computing the dynamic responses of saturated porous rocks through comparing the computed results with the laboratory measurements. Until we can obtain digitized rock data in high enough resolution and process them with sufficient computational resources, the hybrid framework, combining numerical computation and theoretical models, is a practical way of pursuing this goal.

1.2 Review of the Previous Work

Seismic wave propagation velocities and attenuation in poroelastic materials are of interest in many fields. For example, oil reservoirs are composed of a porous rock matrix with oil contained in the pores. Understanding of the intrinsic mechanisms causing dispersion and attenuation is not only a significant academic topic but also an industrial one, and can guide us to better analyze the seismic data collected and to help decipher the geological information underneath. Accurate models for the elastic

wave velocities and attenuations in such reservoirs are required for depth calibration of surface reflection seismograms, lithology classification, hydrocarbon identification, and reservoir management in oil/gas exploration and production. However, the effect of pore structure and fluid motion on wave propagation in complex rocks is not fully understood at intermediate frequencies between the theoretical low-frequency and high-frequency limits. There is an increasing need for characterizing the frequency-dependent viscoelastic properties of rock to better integrate measurements at different frequency ranges, from seismic to sonic logging to ultrasonic laboratory measurements.

Researchers have been carrying out laboratory and field measurements on different types of rocks from small to large scale so as to gain direct observations and build empirical relationships [e.g., Nur and Simmons, 1969, Toksöz et al., 1976, 1979, Winkler and Nur, 1979a, Winkler et al., 1979, Winkler and Nur, 1979b, Murphy, 1982, Winkler and Plona, 1982, Murphy, 1984, Winkler, 1985, Han, 1986, Murphy et al., 1986, Wang and Nur, 1990, Batzle et al., 2006]. Meanwhile, other investigators have been developing mathematical theories and models to explain what have been observed [e.g., Biot, 1956a,b, Walsh, 1965, Kuster and Toksöz, 1974, O'Connell and Budiansky, 1977, Johnston et al., 1979, Gurevich and Lopatnikov, 1991, Berryman, 1992, Dvorkin and Nur, 1993, Dvorkin et al., 1994, 1995, Gurevich et al., 1997, 1999, Gurevich, 2002, Pride and Berryman, 2003a,b, Pride et al., 2004, Muller and Gurevich, 2005, Galvin and Gurevich, 2006, 2007, Gurevich et al., 2008, Müller et al., 2008, Galvin and Gurevich, 2009, Gurevich et al., 2009a,b].

Amongst this work, laboratory experiments significantly contribute to our knowledge of the dynamic responses of saturated porous rocks. Depending on the frequency range of interest, several different techniques can be used to measure the responses of waves to porous rocks in laboratory. Pulse-echo [Winkler and Plona, 1982] and ultrasonic pulse transmission [Toksöz et al., 1979] techniques have been used in the laboratory for frequencies at the range of 100 kilohertz on small samples. The resonant bar technique [Peselnick and Outerbridge, 1961, Tittmann, 1977, Winkler et al., 1979, Winkler and Nur, 1979a] has been employed for frequencies at the range of one

kilohertz and lower. The method requires longer samples. For frequencies well off the resonance frequency, stress-strain measurement has been carried out in laboratory to record the stress-strain behavior of rocks [Gordon and Davis, 1968, McKavanagh and Stacey, 1974, Peselnick and Outerbridge, 1961, Batzle et al., 2006].

Dispersion and attenuation information of rocks can be extracted from data measured by these different techniques in different ways. Traditionally, researchers formulated empirical relationships from laboratory experiments to help predict properties of rocks [e.g., Wyllie et al., 1956, 1958, Han, 1986]. However, such relationships are too simple to be predictive for a wide range of rocks, and lack the detailed description of the micro-structures of rocks.

Parallel with the laboratory work, different theories and models have been developed to explain the underlying causes of such dispersion and attenuation. Biot [1956a, 1956b] developed a theory of wave propagation in saturated porous rocks based on a macroscopic fluid-flow model. In both low- and high-frequency limits, Biot's theory predicts little dispersion and attenuation [Winkler, 1985, Han, 1986, Winkler, 1986, Wang and Nur, 1990]. Mavko and Nur [1975] and O'Connell and Budiansky [1977] proposed squirt-flow models to accommodate pore scale fluid flow and explained the dispersion and attenuation it induces. Based on the Biot and squirt-flow models, Dvorkin and Nur [1993] developed the BISQ (BIot-SQuirt) model to unify the Biot and squirt-flow mechanisms. Dvorkin et al. [1994] showed special cases of squirt-flow at low and high frequencies and compared them with BISQ model. Dvorkin et al. [1995] extended BISQ model to fully saturated rocks. For heterogeneous rocks, Berryman and Wang [1995, 2000] came up with a double-porosity, dual-permeability model to capture the reality that stiff spherical pores and compliant cracks are coexistent within one rock. Pride and Berryman [2003a,b] derived a system of equations to describe the linear dynamics of double-porosity and dual-permeability materials in terms of acoustic attenuation and fluid transportation. Pride et al. [2004] proposed a unified theory to treat P wave attenuation in sedimentary rocks which covers mesoscopic and microscopic scales. Meanwhile, Gurevich and Lopatnikov [1991], Gurevich et al. [1997], Gurevich [2002], Muller and Gurevich [2005], Galvin and Gurevich [2006,

2007], Müller et al. [2008], Galvin and Gurevich [2009], Gurevich et al. [2009a,b] also developed mathematical theories to study wave dispersion and attenuation due to wave-induced fluid flow in the presence of fractures in otherwise porous rocks. To accurately predict the properties of rocks requires highly precise information of its complex micro-structure since the effective properties of porous rocks depend highly on pore spaces, solid grains and interactions between these two. Usually in the derivations of theoretical models, many simplifications and assumptions have been made to make it possible to reach a set of simple mathematical equations describing the physics. Therefore, it is impossible to include the details of the micro-structures of porous rocks in theoretical models.

Though more laboratory measurements and theoretical research will be needed to provide insight on the frequency-dependent acoustical properties of porous media, recent advances in the numerical simulation of wave propagation at the pore-scale may provide answers to some unresolved questions. The numerical simulation approach, commonly called "computational rock physics", computes the effective physical properties of rocks numerically by solving the relevant equations for the pore-scale digitized rock images acquired from X-ray microtomography.

With current advanced imaging techniques such as micro-computed tomography (μ-CT), micro X-ray CT [Flannery et al., 1987, Spanne et al., 1994], focused ion beam scanning electron microscopy (FIBSEM), laser confocal microscopy [Fredrich et al., 1995], and magnetic resonance imaging (MRI), we are able to generate 3D images of rocks at high resolution. The usual voxel resolution is about 1-10 μm or higher. Such high resolution images provide direct measurements of the complex morphology of porous rocks. Combined with computational techniques, we can calculate the material properties such as diffusivity, elasticity, permeability and conductivity. The ultimate goal of the development of these computational experiments and methods is to supplement the traditional measurements carried out inside laboratories, which are time consuming and costly, with cheaper numerical experiments that allow the parameter space to be explored more thoroughly.

Two fundamental classes of numerical methods have been developed and used for

studying rock properties: static and dynamic methods. Roberts and Garboczi [2000], Arns et al. [2002, 2007], Grechka and Kachanov [2006] and Madadi et al. [2009] used the finite element method (FEM) to study the static effective elastic properties of porous media and rocks. While Saenger and Shapiro [2002], Saenger et al. [2004a,b, 2005, 2006], Masson et al. [2006], Saenger et al. [2007], Masson and Pride [2007], Saenger [2008] and Masson and Pride [2010] used finite difference method (FDM) to study the dynamic effective properties of porous rocks. Arns et al. [2002] carried out extensive numerical computations on 3D digitized rocks of several Fontainebleau sandstones with variable porosities, and compared their numerical predictions to those from Gassmann's model and experimental measurements. They concluded that for such type of clean sandstone as Fontainebleau sandstone, elastic property-porosity relationships can be derived from microtomographic images. Arns et al. [2007] applied the same numerical method on the poorly-cemented granular rocks, and studied the effects of contact moduli on linear effective elastic properties of such rocks. Saenger et al. [2000] developed a finite difference solver using rotated-staggered-grid scheme (RSG) and studied the dynamic responses of cracked rocks [Saenger and Shapiro, 2002, Saenger et al., 2004a], and he compared the numerical results to those estimated by different effective medium theories. Saenger et al. [2005] extended the RSG scheme to incorporate the viscous effect of fluid and studied the Biot's effects of synthetic porous rocks. With the same solver, Saenger et al. [2006] and Saenger [2008] presented a new technique for computing static effective elastic properties and explained discrepancies between some numerical studies in terms of static and dynamic numerical experiments. Based on Biot's poroelasticity theory [Biot, 1956a,b], Masson et al. [2006] and Masson and Pride [2007, 2010] published a series papers about their work on developing time-domain finite-difference solvers to study seismic attenuation and dispersion across all frequencies due to wave-induced fluid flow in rocks with mesoscopic scale heterogeneities. Rubino et al. [2009] studied the same problems for heterogeneous fluid-saturated porous rocks by solving coupled Biot's equations with the finite-element method in the frequency domain. In all of these computations, they claimed the numerical predictions can verify some theoretical models, and even

explain some experimental measurements, which is a good aspect of computational experiments.

The finite difference time-domain solver that Saenger et al. [2005] developed to perform pore-scale simulation of wave propagation in porous materials saturated with a viscous Newtonian fluid handles well the large contrast between solid and fluid material properties found in porous rocks. The problem of handling viscous fluid was solved with minimal modification to an existing elastic wave propagation code by recognizing that the linearized Navier-Stokes equation for the fluid can be regarded as a wave equation where the fluid has an imaginary, frequency-dependent shear modulus. This frequency-dependent shear modulus was approximated in the time-domain simulation by a single-order generalized Maxwell body (GMB) model [Emmerich and Korn, 1987]. Since the approximation used is only exact in the low-frequency limit, small errors are introduced in finite-frequency simulations. Additionally, the GMB approximation may require smaller time steps for stability than the exact solution.

In contrast with the GMB approximation, an exact description of the interaction between a viscous fluid and a solid has already been studied in computational biomechanics [Greenshields and Weller, 2005, Giannopapa and Papadakis, 2008]; in both cases a finite-volume method rather than a rotated-staggered-grid finite-difference method was employed to solve the coupled system. However, Greenshields and Weller [2005] applied this method on simulating the propagation of pressure waves in an artery, where the low contrast of material properties did not create instability. Giannopapa and Papadakis [2008] derived a mathematical formulation for the coupled system, but applied it only on an elastic solid where no coupling between the solid and a fluid was demonstrated.

Even with the X-ray CT imaging technique, we are unable to obtain images of rocks with high enough resolution such that every single crack or micro-pore between and within grains for sandstones or carbonates can be illuminated. Even if we were able to do so, current computational resources would limit our ability to solve such a huge 3D problem on a realistic scale, since the resolution required has to be down to the nanometer scale. Therefore, we generally lose small features of rocks during

the imaging process such as phase separation. Arns et al. [2007] had realized this drawback and tried to remedy it by introducing contact porosity for poorly-cemented sandstones. In their approach, they utilized microtomographic images and grain-partitioning techniques to assign grain moduli, then used effective medium theories locally to calculate contact moduli between grains for phases such as clay.

However, we found that the loss of small features of rocks due to the imaging process not only affects poorly-cemented sandstones as Arns et al. [2007] discussed, but also well-cemented sandstones such as Fontainebleau sandstone and Berea sandstone. For example, in the paper by Arns et al. [2002], though the numerical predictions with 3D digitized rocks of Fontainebleau sandstones using FEM can match Gassmann's equations and experimental measurements well, we found that (1) the computed velocities for both dry and water/oil saturated cases are generally higher than experimental measurements, and (2) velocities of P-wave for dry rocks are higher than those for water/oil saturated cases, which contradicts the intuitions and laboratory observations for sandstones. We also found the same contradicting phenomena in our own computations on digitized 3D Berea sandstones. One explanation Arns [2002] gave to such observations is due to the periodic boundary condition used in the FEM solver. However, we do not think this is the real reason behind these observations.

The low-frequency response of fluid-saturated porous rocks interests the geophysicists the most. In the low-frequency band used in seismic exploration, we can still observe non-negligible dispersion and attenuation, which is highly dependent on fluid mobility and the distributions of heterogeneities in rocks [Gurevich et al., 1997, Gurevich, 2002, Pride and Berryman, 2003a,b, Pride et al., 2004, Muller and Gurevich, 2005, Galvin and Gurevich, 2006, 2007, Müller et al., 2008, Galvin and Gurevich, 2009]. Generally, stress-strain measurement has been used either in laboratory experiments or in numerical computations to obtain such low-frequency responses [Batzle et al., 2006, Masson et al., 2006, Masson and Pride, 2007, Rubino et al., 2009, Masson and Pride, 2010]. However, limited by the assumptions made in Biot's poroelasticity theory, the low-frequency responses obtained from any computation based on poroelasticity theory can represent only the Biot-type mechanism, and the squirt-

flow effect is not included. The porous rocks synthesized statistically as heterogeneous poroelastic media do not preserve the detailed micro-structures of pore spaces as well.

1.3 The Content of the Thesis

In this thesis, we include five chapters, in total, to accomplish the tasks mentioned in the objectives in Section 1.1.

In Chapter 1 we describe the objectives of this thesis and review the past work on the study of rock physics of saturated porous rocks in terms of laboratory work, theoretical developments and very recent developments in computational rock physics. We point out the problems we are facing in this type of research, especially those related to the computational work, and list the tasks we are to accomplish in this thesis.

In Chapter 2 we present a convenient implementation of the full coupled problem, which is stable even with high contrasts in material properties. The linearized Navier-Stokes equation is solved in the fluid and coupled with the elastic wave equation in the solid matrix. A rotated-staggered-grid finite-difference scheme is used to handle the high contrast of material properties between fluid and solid without the inconvenience of explicitly and separately solving the fluid-solid boundary conditions. A single mathematical form is applied to both the solid and fluid cells; this simplifies implementation without resorting to the GMB approximation. This implementation of the coupled problem is validated by comparing the numerical results with analytical solutions for an idealized porous medium of periodically alternating solid and fluid layers. A von Neumann stability analysis is provided to guide selection of the time step.

In Chapter 3 we discuss the observed discrepencies between numerical results and laboratory measurements. The computed velocities of saturated porous rocks are higher than laboratory data. The details of the digitized rock images are limited by the resolution of the imaging process that is usually about 1-10 μm. Therefore, we lose some very fine features such as cracks and micro-pores whose scales are usually

less than 1 μm [Sprunt and Brace, 1974]. Without the cracks, the frame of porous rock becomes stiffer than it should be. To resolve this issue related to the image resolution, we propose a hybrid method — combining numerical computation with the differential effective media theory and the Kuster-Toksöz model. Using only the laboratory data of the velocities of P- and S-waves for dry and water-saturated rocks, a Monte-Carlo inversion has been developed to invert the cracks lost in the imaging process. By using this hybrid method, we are able to compensate for the contribution of lost cracks to the final effective elastic properties of rocks. Finally, we compute the effective elastic properties of rocks and compare these numerical results with laboratory measurements.

In Chapter 4 we first demonstrate the particle motion on microscale for a 2D slice of digitized rock so as to intuit the cause of frequency-dependent seismic responses. Then we introduce the stress-strain calculation, which we utilize in numerical computation to measure the low-frequency response and the effects of fluid viscosity on seismic dispersion and attenuation. Since only two phases — solid matrix and fluid inclusion — are considered in our simulation, friction, the dominant mechanism of attenuation in sandstones due to cracks within and between grains, cannot be captured. To compensate for the missing attenuation due to friction and viscous fluid in compliant pores, we further extend the hybrid method introduced in Chapter 3 by utilizing the modified squirt-flow model. Besides using the velocities of P- and S-waves measured in laboratory, we also use the measured attenuation of P-waves in the Monte-Carlo inversion, which can help further constrain the inversion for crack distribution. The final computed velocities and attenuations for different fluids are compared with laboratory measurements.

In Chapter 5 we first draw conclusions for the work done in this thesis, then to discuss the future work on this topic, especially emphasizing (1) GPU computing to speed up the simulation so as to model large 3D cases at low enough frequencies and (2) the use of the nonlinear solver developed to investigate the issues related to the wave-induced fluid flow in large 3D models at low frequencies.

Chapter 2

Linear Solver for Single Phase Viscous Fluid[1]

Intrinsic wave propagation velocity and attenuation in poroelastic materials are of interest in many fields. For example, oil reservoirs are composed of a porous rock matrix, such as sandstone, with oil contained in the pore space. Accurate models for the elastic wave velocities and attenuations in such reservoirs are required for depth calibration of surface reflection seismograms, lithology classification, hydrocarbon identification, and reservoir management in oil/gas exploration and production. However, the effect of pore structure and fluid motion on wave propagation in complex rocks is not fully understood at intermediate frequencies between the theoretical low-frequency and high-frequency limits. There is an increasing need for characterizing the frequency-dependent viscoelastic properties of rock to better integrate measurements in different frequency ranges, from seismic to sonic logging to ultrasonic laboratory measurements.

It is known that the wave-induced motion of viscous fluid in a porous matrix has a significant frequency-dependent effect on both acoustic velocity and attenuation. Different physical mechanisms and theoretical models have been proposed. Biot [1956a, 1956b] developed a theory of wave propagation in saturated porous rocks based on a

[1] Zhang, Y., L.M. Song, M. Deffenbaugh and M.N. Toksöz. A finite difference method for a coupled model of wave propagation in poroelastic materials, Journal of the Acoustical Society of America, 127(5), 2847-2855, 2010.

macroscopic fluid-flow model. In both low- and high-frequency limits, Biot's theory predicts little dispersion and attenuation. The maximum dispersion and attenuation occur in between, at Biot's characteristic frequency which is proportional to the fluid viscosity. However, experimental work [Winkler, 1985, Wang et al., 1991, Adam et al., 2006] shows that Biot's theory cannot explain all the dispersion and attenuation observed in laboratory and field. Though the experimental results were statistically insufficient to reach general conclusions about physical causes, it seems likely that heterogeneous and compliant pores/micro-fractures in the samples were significantly influencing the interaction between the fluid and the solid matrix at the pore-scale.

Though more laboratory measurements will be needed to provide insight on the frequency-dependent acoustical properties of porous media, recent advances in the numerical simulation of wave propagation at the pore-scale may provide answers to some unresolved questions. This numerical simulation approach, commonly called "computational rock physics", computes the effective physical properties of rocks numerically by solving the relevant pore-scale fundamental physics on pore-scale digitized rock images acquired from X-ray microtomography scans. It has been applied mostly to model the effect of pores, fractures and fluid on static elastic properties using finite element methods [Roberts and Garboczi, 2000, Arns et al., 2002, Grechka and Kachanov, 2006].

Recently Saenger et al. [2005] developed a finite-difference time-domain method to perform pore-scale simulation of wave propagation in porous materials saturated with a viscous Newtonian fluid. A rotated-staggered-grid scheme was used for the finite-difference computation, which handled well the large contrast between solid and fluid material properties found in porous rocks. This problem was solved with minimal modification to an existing elastic wave propagation code by recognizing that the linearized Navier-Stokes equation for the fluid can be regarded as a wave equation where the fluid has an imaginary, frequency-dependent shear modulus. This frequency-dependent shear modulus was approximated in the time-domain simulation by a single-order generalized Maxwell body (GMB) model [Emmerich and Korn, 1987]. Since the approximation used is only exact in the low-frequency limit, some

small errors are introduced in finite-frequency simulations. Additionally, the GMB approximation may require smaller time steps for stability than the exact solution.

In contrast with the GMB approximation, an exact description of the interaction between a viscous fluid and a solid has already been studied in computational biomechanics [Greenshields and Weller, 2005, Giannopapa and Papadakis, 2008]; in both cases a finite-volume method rather than a rotated-staggered-grid finite-difference scheme was employed to solve the coupled system. However, Greenshields and Weller [2005] applied this method on simulating the propagation of pressure waves in an artery, where the low contrast of material properties did not create instability. Giannopapa and Papadakis [2008] derived a mathematical formulation for the coupled system, but applied it only on an elastic solid where no coupling between the solid and a fluid was demonstrated.

This paper presents a convenient implementation of the full coupled problem which is stable even with high contrasts in material properties. The linearized Navier-Stokes equation is solved in the fluid and coupled to the elastic wave equation in the solid matrix. A rotated-staggered-grid scheme is used to handle the high contrast of material properties between fluid and solid without the inconvenience of explicitly and separately solving the fluid-solid boundary conditions. A single mathematical form is applied to both the solid and fluid cells, which simplifies implementation without resorting to the GMB approximation. This implementation of the coupled problem is validated by comparing the numerical results with the analytical solution for an idealized porous medium of periodically alternating solid and fluid layers. A von Neumann stability analysis is provided to guide selection of the time step.

2.1 Governing Equations

Consider a medium consisting of a porous elastic matrix filled with a compressible Newtonian fluid. The displacement vector, $\mathbf{u}$, associated with a small disturbance propagating through the medium is described at any point $\mathbf{x}$ and time t by the elastic

dynamic equation in the solid:

$$\rho_s \frac{\partial^2 \mathbf{u}}{\partial t^2} = (\lambda + \mu) \nabla (\nabla \cdot \mathbf{u}) + \mu \nabla^2 \mathbf{u} + \mathbf{f} \tag{2.1}$$

and the Linearized Navier-Stokes equation (wherein convection acceleration is ignored) in the fluid:

$$\rho_f \frac{\partial^2 \mathbf{u}}{\partial t^2} = K_f \nabla (\nabla \cdot \mathbf{u}) + \frac{\partial}{\partial t} \left[\eta_\mu \nabla^2 \mathbf{u} + (\eta_\mu + \eta_\lambda) \nabla (\nabla \cdot \mathbf{u}) \right] + \mathbf{f} \tag{2.2}$$

In equation (2.1), ρ_s, λ and μ are the density and Lamé elastic constants of the solid phase, and in equation (2.2), ρ_f, K_f, η_μ and η_λ are the density, compressional or bulk modulus, shear viscosity, and second viscosity coefficient of the fluid phase. In both equations, the vector $\mathbf{f}$ is the volumetric force. At the gridding scale, it is assumed that the material properties of the solid and fluid are homogeneous and isotropic, but at a macroscopic scale the medium can be heterogeneous and anisotropic as the material properties vary spatially. Note that the equations above can describe a rock composed of multiple solid or fluid phases. The equations are coupled through the boundary conditions at the interface between adjacent solid and fluid phases. The equilibrium condition requires that the stresses be continuous across the boundary and the no-slip condition (due to non-zero fluid viscosity) requires that there be equal displacement across the boundary.

2.2 Numerical Implementation

2.2.1 Finite difference implementation

For the numerical implementation, it is convenient to solve both the elastic wave equation and the linearized Navier-Stokes equation for the particle velocity vector $\mathbf{v}$ and the stress vector $\boldsymbol{\sigma}$. Both equations may be written in the common form:

$$\rho \frac{\partial \mathbf{v}}{\partial t} = \nabla \cdot \boldsymbol{\sigma} + \mathbf{f} \tag{2.3}$$

For the solid phase, $\rho = \rho_s$, and

$$\frac{\partial \sigma_{ij}}{\partial t} = D^S_{ijkl}\left(\frac{\partial v_k}{\partial x_l} + \frac{\partial v_l}{\partial x_k}\right) \tag{2.4}$$

where D^S_{ijkl} is the stiffness tensor for the solid.
For the fluid phase, $\rho = \rho_f$, and

$$\sigma_{ij} = -p\delta_{ij} + E^F_{ijkl}\left(\frac{\partial v_k}{\partial x_l} + \frac{\partial v_l}{\partial x_k}\right) \tag{2.5}$$

where $E^F_{ijkl} = \eta_\lambda \delta_{ij}\delta_{kl} + \eta_\mu\left(\delta_{ik}\delta_{jl} + \delta_{il}\delta_{jk}\right)$ describes the anelastic contribution of the strain rate to the stress, and the pressure p is expressed in terms of the velocities as,

$$\frac{\partial p}{\partial t} = -D^F_{ijkl}\left(\frac{\partial v_k}{\partial x_l} + \frac{\partial v_l}{\partial x_k}\right) \tag{2.6}$$

where $D^F_{ijkl} = K_f \delta_{ij}\delta_{kl}$ is the stiffness tensor for the fluid.

Equations (2.3)-(2.6) are solved by starting from given initial conditions and stepping the solution forward in time. For time-domain finite-difference solvers, the standard-staggered-grid (SSG) scheme is usually used, but this scheme needs to average the shear moduli or shear viscosities diagonally between cells. As shown in Figure 2-1. when the cell edges align with the grid and the velocities are defined on cell edges, the numerical derivatives for compressional strains (e.g., $\frac{\partial v_x}{\partial x}$) approximate values at the cell centers, while the numerical derivatives for shear strains (e.g., $\frac{\partial v_x}{\partial z}$) approximate values at the cell corners. Shear moduli (for solid cells) or shear viscosities (for fluid cells) must then be determined for the cell corners, which is accomplished by averaging these properties diagonally between cells. When this averaging combines properties between solid and fluid cells, a third expression for stress is needed which is more complicated than either equation (2.4) or (2.5) alone. Due to this averaging of properties, the stress in cells along a fluid-solid boundary would depend on the shear moduli like a solid cell and on the viscosities like a fluid cell. Furthermore, because of the high contrast of material properties between fluid and solid, numerical noise due to instability is usually generated along the interface. To

avoid the inconvenience of handling this third equation for stress and the numerical instability, a rotated-staggered-grid (RSG) scheme [Saenger et al., 2000; see details in Appendix A] is used. As shown in Figure 2-2, in the RSG scheme, the axes are oriented at 45 degrees with respect to the cell edges and all velocity components are defined at every cell corner. The numerical derivatives for both compressional and shear strains require only differences between velocities at diagonal corners of the same cell and the numerical derivatives approximate strains at the cell centers. Thus material properties are only required at the cell centers. The advantages of using the RSG scheme are that it does not require averaging of material properties across solid/fluid boundaries and the coupling between the two phases is fulfilled naturally by the continuities of velocities and stresses on the boundaries without explicitly and separately handling the boundary conditions.

A finite difference method for solving the elastic wave equation using the RSG scheme has been established by Saenger et al. [2000]. Here a method for solving the linearized Navier-Stokes equation is described. For the coupled model, Saenger's method would be applied in the solid cells and this method in the fluid cells. To solve the linearized Navier-Stokes equations using the RSG scheme, it is useful to define the pressure and stresses at staggered time steps. Assume the pressure and stresses are known at time $t-\frac{\Delta t}{2}$ and velocities are known at time t, the pressure and stresses field at time $t+\frac{\Delta t}{2}$ are found from the velocities at time t using equations (2.5) and (2.6). Then, the velocities are updated to time $t+\Delta t$ from the pressure and stresses at time $t+\frac{\Delta t}{2}$ using equation (2.3).

2.2.2 Relationship between the fluid and solid equations

By comparing the Fourier transforms of equations (2.4) and (2.5), it is clear that the correct dynamics for the system could be produced at angular frequency ω by solving only the elastic wave equation (equations (2.3) and (2.4)) in every cell, while replacing the stiffness tensor D^S_{ijkl} with,

$$D^{S-Fluid}_{ijkl} = D^F_{ijkl} + i\omega E^F_{ijkl} \tag{2.7}$$

in the fluid cells. In other words, the linearized Navier-Stokes equation can be thought of as the elastic wave equation with frequency-dependent elastic moduli. Indeed, an elastic wave propagation code can be modified to solve the coupled equations by simply adding an anelastic term for the fluid cells which depends on the time derivative of the strain. This can be seen by comparing equations (2.4) and (2.5).

A wave propagation code can also be modified to approximately handle Newtonian fluids using the Generalized Maxwell Body (GMB) approximation [Emmerich and Korn, 1987], though this offers no benefits over directly implementing equation (2.5). The GMB approximation sets up an ordinary differential equation in time for each cell which is forced by the strain tensor and generates a tensor of anelastic terms. The anelastic tensor is added to Hooke's law to approximate arbitrary frequency-dependent elastic moduli. Unfortunately, the form of the GMB approximation cannot provide the derivative of strain as required for a Newtonian fluid. Nevertheless, it can approximate the strain derivative and has been applied to the present problem with good results [Ciz et al., 2006]. When the GMB approximation uses one relaxation mechanism and is constrained to be correct at zero frequency [e.g., Saenger et al., 2005] it amounts to replacing the true frequency-dependent stiffness tensor of equation (2.7) with,

$$D_{ijkl}^{GMB} = D_{ijkl}^{F} + i\omega \left[\frac{\omega_r}{\omega_r + i\omega} \right] E_{ijkl}^{F} \tag{2.8}$$

for constant relaxation frequency ω_r. From equation (2.8), it is clear that the approximation becomes exact in the low-frequency (small ω) limit, as the term in the square brackets approaches unity. At higher frequencies, the approximation introduces four kinds of modeling errors. First, it creates a non-zero real shear modulus at finite frequencies, allowing propagating shear waves which cannot actually exist in a fluid. Second, it reduces the imaginary part of the shear modulus, creating an effective viscosity that is always lower than the true viscosity. Third, it creates an imaginary part in the bulk modulus causing attenuation of compressional waves beyond that due to poroelastic effects. Fourth, it makes the compressional wave velocity artificially large, asymptotically approaching $\sqrt{\frac{K_f + \omega_r(\eta_\lambda + 2\eta_\mu)}{\rho_f}}$ at high frequency. Within a

frequency band of interest, all of these errors can be made insignificant by making ω_r sufficiently large. However, if the spurious compressional wave velocity at high frequency becomes the fastest velocity in the model, it controls the finite difference time step required to maintain von Neumann stability. At this point, further error reduction comes at the price of smaller time steps and thus slower execution speed. The GMB approximation has the additional disadvantage of requiring for each cell the introduction of a tensor with six anelastic parameters and a first order differential equation to describe their time evolution. By contrast, handling the fluid exactly according to equation (2.5) requires only retaining the time derivative of the existing strain tensor. For a Newtonian pore fluid, the GMB approximation offers no benefits over the full coupled model. It is slightly less accurate, potentially less stable at the same time step, has a larger memory footprint due to storing the anelastic parameters and their derivatives, and is slower due to computing the dynamics of the anelastic parameters.

2.3 Numerical Validation

The numerical solution was tested on a model with periodically alternating solid and viscous fluid layers. The layered model is an idealized porous medium which has analytic solutions for the velocity and attenuation of the compressional wave [Ciz et al., 2006; see also Appendix B]. As shown in Figure 2-3, a two-layered model with one solid layer and one viscous fluid layer was used. Periodic boundary conditions were applied on both the top and bottom to represent alternating layers of solid and fluid extending to infinity. The modeling parameters are listed in Table 2.1. A compressional plane wave source was used and four lines of receivers were deployed perpendicular to the direction of propagation at different ranges from the source. Lines R1, R2 and R3 were separated by 1000 grid points between each other, and lines R1 and R4 were separated by one wavelength. The effective velocity between R1 and R2 was estimated from the difference in arrival times of the waveform peak at R1 and R2. Attenuation ($1/Q$) was estimated from the amplitude change between

R1 and R4, assuming a constant Q on this interval. An image of a wave propagating through this idealized porous medium is shown at one time step in Figure 2-4. Note that the compressional wave propagating in the solid induces particle motion in the fluid along the interface. This relative motion between the solid and fluid plays an important role in causing dispersion and attenuation.

The computed results from the coupled model are compared with the analytical solution for effective velocities (Figure 2-5) and for attenuation (Figure 2-6). As shown in Figure 2-5, the computed results agree well with the analytic solution at high viscosity, but diverge at low viscosity. This is attributed to insufficient sampling of the viscous boundary layer which becomes much thinner at low viscosity. According to Ciz et al. [2006], at least 3 grids inside the boundary layer are needed to minimize this kind of numerical dispersion. However, in the case with $\eta_\mu = 0.01\,\mathrm{kg/m \cdot s}$, for example, there is less than one grid sampling the boundary layer for $\Delta x = 10^{-5}\,\mathrm{m}$, which is not sufficient according to this criterion. Increasing the sampling within the boundary layer by using smaller $\Delta x = 2 \times 10^{-6}\,\mathrm{m}$ improves the computed values. For higher viscosities, the computed results agree well with the analytic solutions because of sufficient sampling in the boundary layer.

2.4 Numerical Comparison with the GMB Approximation

As we have discussed previously, our method has advantages over other methods [Saenger et al., 2005, Greenshields and Weller, 2005, Giannopapa and Papadakis, 2008] in terms of solving fully coupled system without approximation and handling high material contrast. Among the other three methods, the one with the GMB approximation [Saenger et al., 2005] is the one most similar to ours. Also due to difficulty in accessing to the other two methods [Greenshields and Weller, 2005, Giannopapa and Papadakis, 2008], we only compare our method to the one with the GMB approximation in this section with an extreme case in which the viscosity of

fluid was chosen to be $100\,\mathrm{kg/m \cdot s}$.

As shown in Figure 2-7, we recorded traces of compressional wave along middle axis of solid layer at the lines of R1, R2 and R3, which were computed from our method (solid line) and the one with GMB approximation (dash line), respectively. We can see that as the wave propagates further, the amplitudes of waves decrease with both methods. However, it is obvious that energy computed using the GMB approximation is attenuated much faster. According to our discussion, the GMB approximation usually overestimates the attenuation of compressional wave for finite frequency due to its simplified approximation, which is demonstrated by our numerical comparison.

2.5 Stability Analysis

For numerical stability, the finite-difference gridding must satisfy a certain relationship between grid spacing Δx, time increment Δt and material properties. The required relationship is well known for solving the wave equation [Saenger et al., 2000]. The relationship for solving the linearized Navier-Stokes equations is derived for the 2D case in Appendix C and descibed here. Numerically solving the quartic equation (C.8) by using the eigenvalue method [Press et al., 1992] gives four roots $g = \{\lambda_1, \lambda_2, \lambda_3, \lambda_4\}$, which are real or complex values. The stability criterion requires the absolute values of these four roots to be less than one.

Figure 2-8 and Figure 2-9 show the distribution of the four roots in the complex coordinate plane for a sampling of wavenumbers (k_x, k_z) . Given the same physical properties of the viscous fluid and grid spacing Δx, all four roots can be within the unit circle for small enough Δt (Figure 2-9) and the computation will be stable. For larger Δt, some roots, like λ_1 and λ_3 in Figure 2-8, move outside of the unit circle for certain wavenumbers and the computation becomes unstable. The stable region for solving the linearized Navier-Stokes equations also depends on the fluid viscosity. As shown in Figures 2-9 to 2-11, keeping Δx and Δt the same while increasing the fluid viscosity, changes the distribution of the roots from the case where all roots are

within the unit circle to the case where some roots are outside of it, which means that the computation becomes unstable with increasing viscosity.

The von Neumann analysis is more complicated for the linearized Navier-Stokes equation. The stable and unstable combinations of Δx and Δt for the example material properties were found numerically and are shown in Figure 2-12. In the stable region, the absolute values of all roots are less than one, and in the unstable region, the absolute value of at least one root is larger than one. For small viscosity, the linearized Navier-Stokes equation approaches the acoustic wave equation, and the stability region is bounded by $\Delta t = c^{-1}\Delta x$, where $c = \sqrt{\frac{K_f}{\rho_f}}$ is the compressional wave velocity, 1483 m/s in Figure 2-12. When the viscosity is large, the linearized Navier Stokes equation approaches a diffusion equation, and the stable region is bounded by $\Delta t = d^{-1}\frac{(\Delta x)^2}{2}$ where $d = \frac{(\eta_\lambda + 2\eta_\mu)}{\rho_f}$ is the diffusion coefficient. For example, $d = 233\,\mathrm{m}^2/\mathrm{s}$ on the curve for $\eta_\mu = 100\,\mathrm{kg/m \cdot s}$ in Figure 2-12. The boundary of the stable region is seen to approach these small-viscosity and large-viscosity asymptotes in Figure 2-12. Note that the small viscosity case applies for typical viscosities, densities, and bulk moduli of pore liquids in nature ($\eta_\mu \leq 0.1\,\mathrm{kg/m \cdot s}$,$\rho_f \sim 1000\,\mathrm{kg/m}^3$,$K_f \sim 2\,\mathrm{GPa}$) when the grid spacing is $10^{-6}\,\mathrm{m}$ or larger. For a model with given source frequency and material properties, the grid spacing Δx is selected to provide enough grid cells within the smallest wavelength. Then, the finite difference time step Δt is chosen to satisfy the stability criterion.

Table 2.1: Material properties for numerical modeling with the coupled model (In all the cases, we only consider the situation where $\eta_\lambda = \eta_\mu$).

	Vp (m/s)	Vs (m/s)	Density (kg/m^3)	Viscosity (kg/m $\cdot$ s)
Solid	5100	2944	2540	
Fluid	1483	0	1000	0.001,0.01,0.1,1,10,100

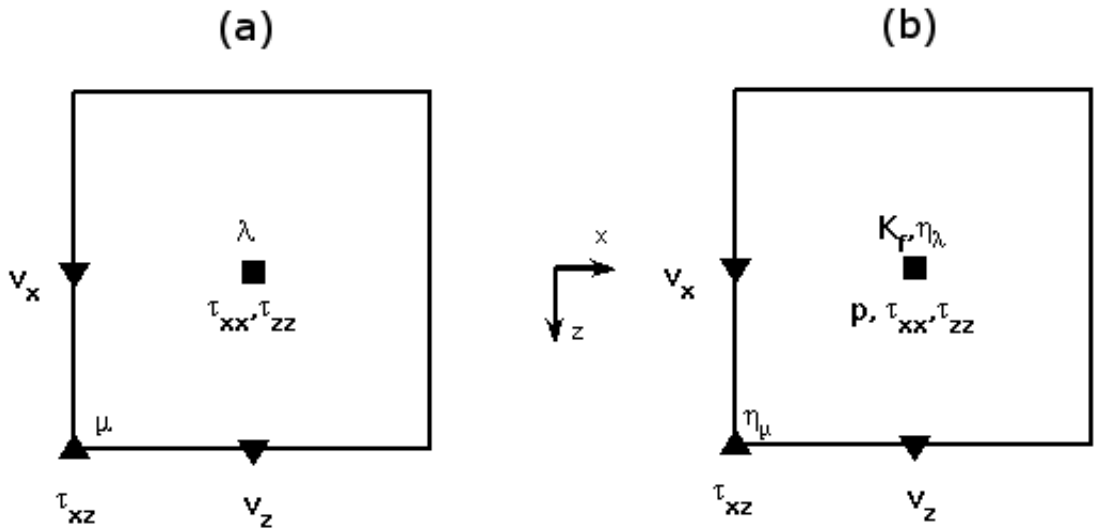

Figure 2-1: Standard-staggered-grid scheme for (a) cells in the solid and (b) cells in the viscous fluid.

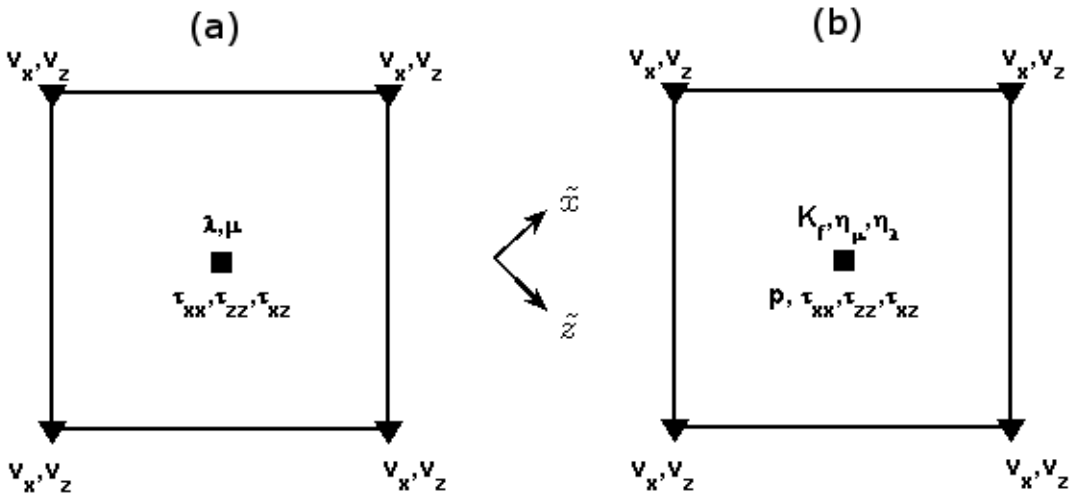

Figure 2-2: Rotated-staggered-grid scheme for (a) cells in the solid and (b) cells in the viscous fluid.

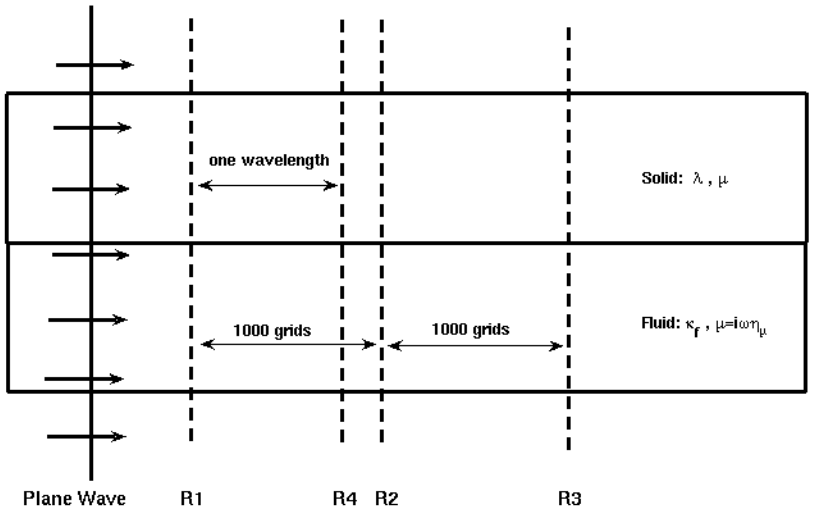

Figure 2-3: Model with periodically alternating solid and fluid layers. A compressional plane wave is used as the source. Four receiver lines R1, R2, R3 and R4 are deployed. Periodic boundary conditions are applied at the top and bottom of the model.

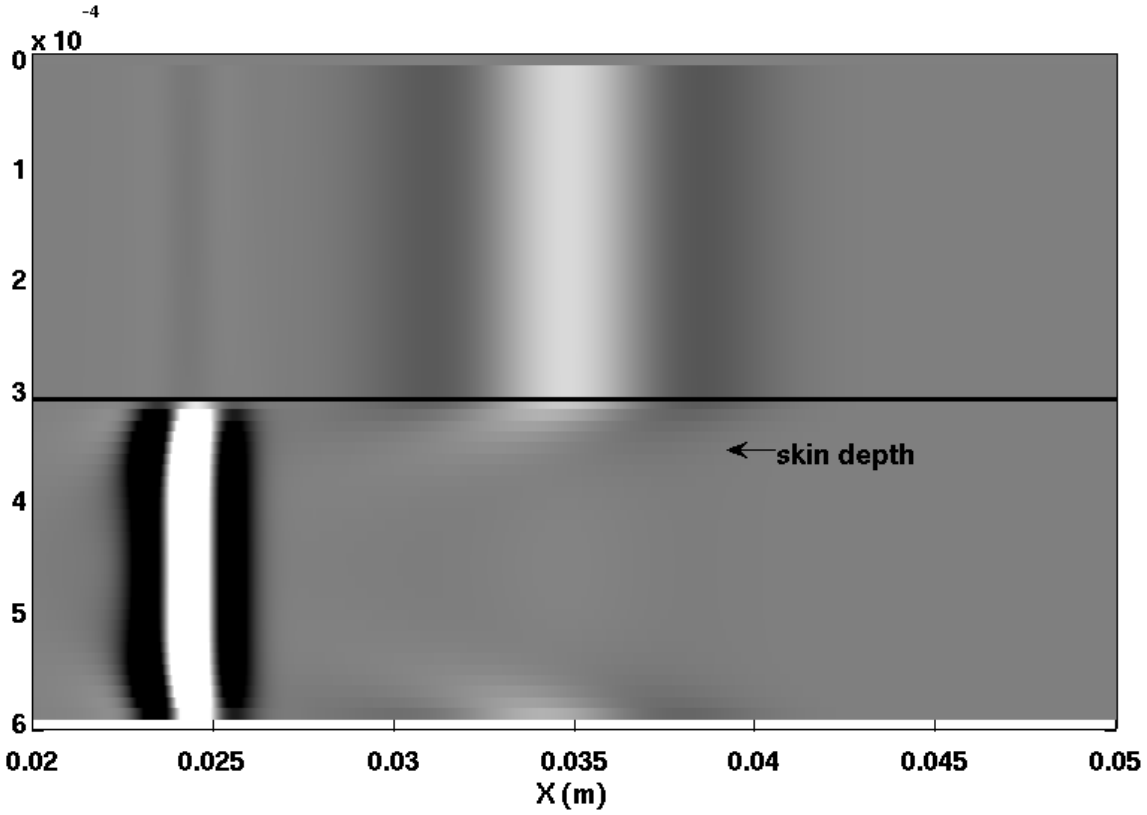

Figure 2-4: A snapshot of the compressional wave propagating in an idealized porous medium at some time step. Waves travel faster in the solid (upper half) than in the fluid (lower half). The wave traveling in the solid induces motion of the fluid within a certain skin depth along the interface.

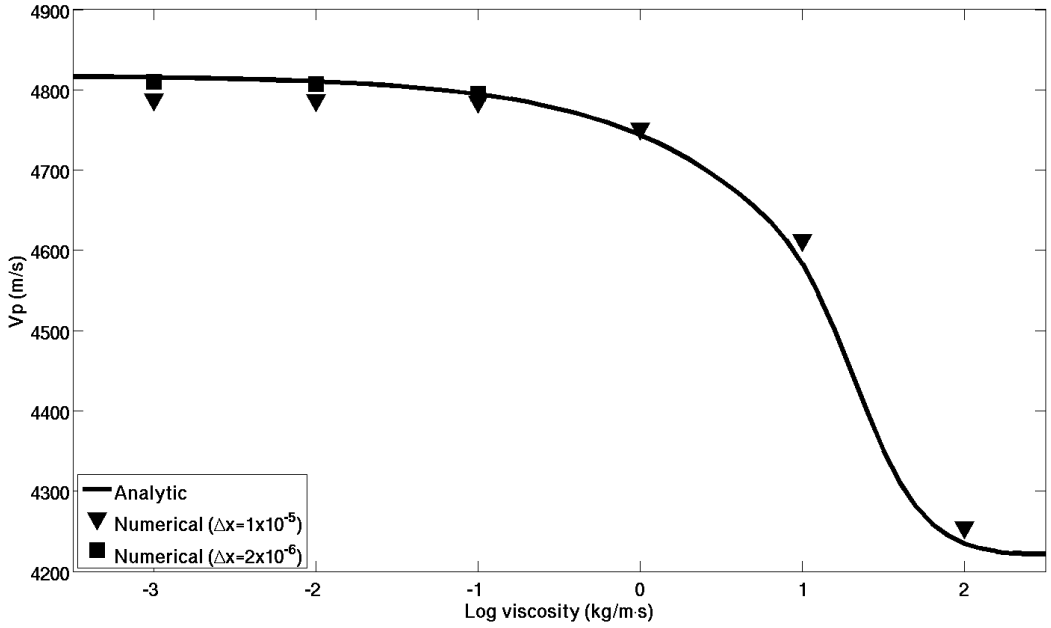

Figure 2-5: Variation of the compressional wave velocity with fluid viscosity. Numerical results calculated at a coarser grid ($\Delta x = 1 \times 10^{-5}$ m, shown by triangles) and a finer grid ($\Delta x = 2 \times 10^{-6}$ m, shown by squares) are compared to the analytic solution (solid curve). At lower viscosities, numerical dispersion is caused by insufficient sampling of the viscous boundary layer. This is remedied by finer gridding.

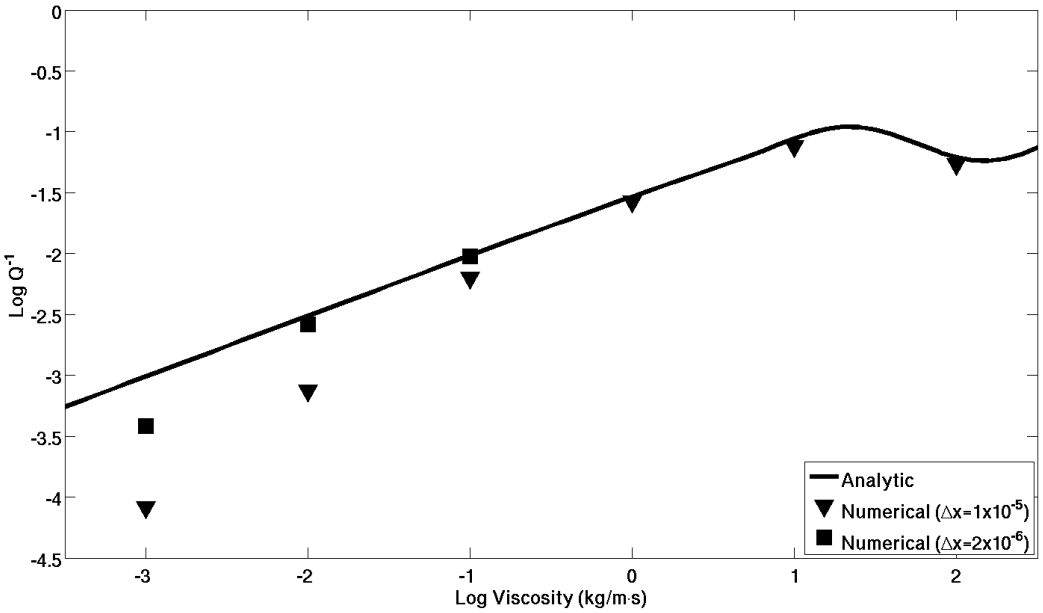

Figure 2-6: Variation of the compressional wave attenuation with fluid viscosity. Numerical results calculated at a coarser grid ($\Delta x = 1 \times 10^{-5}$ m, shown by triangles) and a finer grid ($\Delta x = 2 \times 10^{-6}$ m, shown by squares) are compared to the analytic solution (solid curve). At lower viscosities, numerical dispersion occurs because of insufficient sampling of the viscous boundary layer. This is remedied by finer gridding.

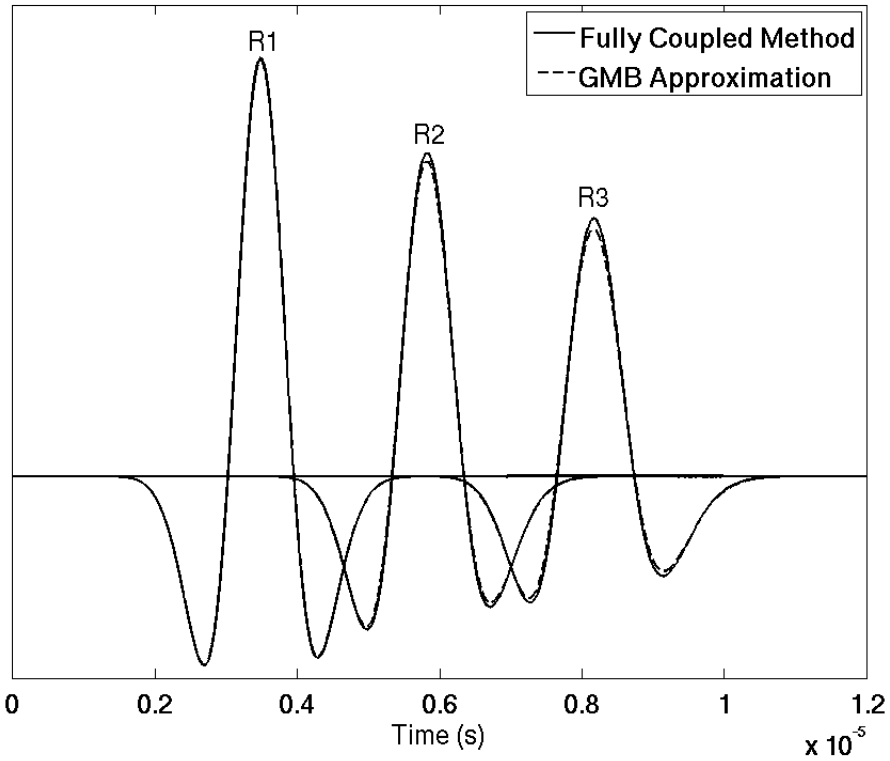

Figure 2-7: Comparisons between compressional waves computed from the fully coupled method (solid) and the one with GMB approximation (dash). The method with GMB approximation overestimates the attenuation of compressional wave.

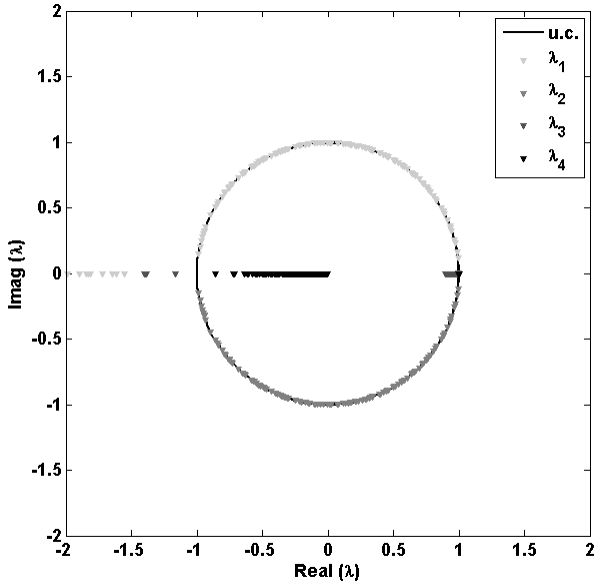

Figure 2-8: Distribution of the four roots in the complex plane for a sampling of wavenumbers. The roots λ_1 and λ_3 are outside the unit circle for some wavenumbers. The model considered has $\Delta x = 2 \times 10^{-6}$ m, $\eta_\mu = 0.01\,\mathrm{kg/m \cdot s}$, and a relatively large $\Delta t = 1 \times 10^{-8}$ s.

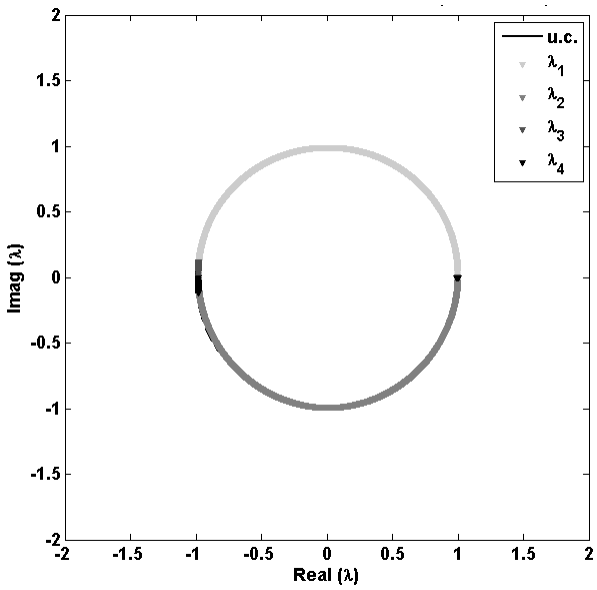

Figure 2-9: Distribution of the four roots in the complex plane for a sampling of wavenumbers. All four roots remain within the unit circle at all wavenumbers. The model considered has $\Delta x = 2 \times 10^{-6}$ m, $\eta_\mu = 0.01\,\mathrm{kg/m \cdot s}$, and a relatively small $\Delta t = 1.338 \times 10^{-9}$ s.

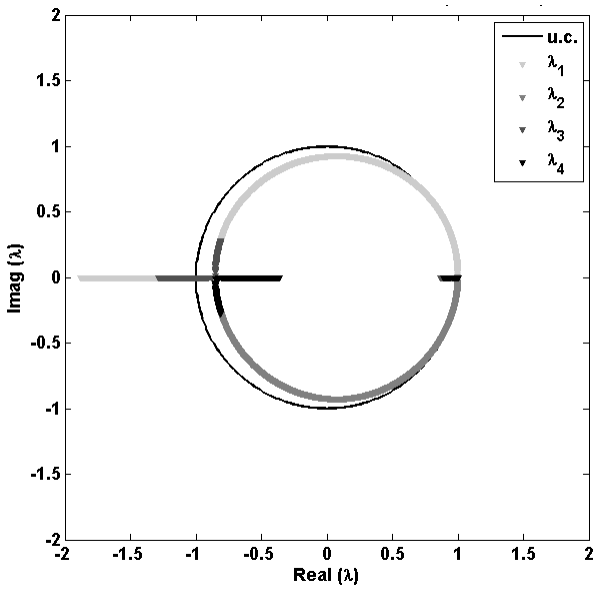

Figure 2-10: Distribution of the four roots in the complex plane for a sampling of wavenumbers. The model considered has $\Delta x = 2 \times 10^{-6}$ m, $\Delta t = 1.338 \times 10^{-9}$ s, and a large viscosity $\eta_\mu = 0.1\,\mathrm{kg/m \cdot s}$.

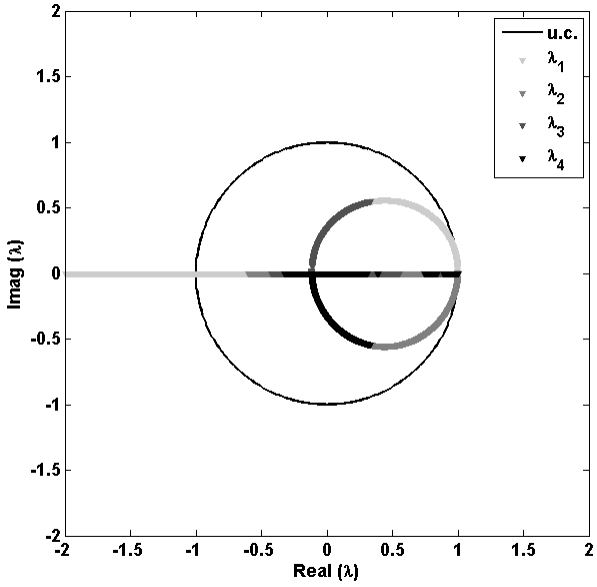

Figure 2-11: Distribution of the four roots in the complex plane for a sampling of wavenumbers. The model considered has $\Delta x = 2 \times 10^{-6}$ m, $\Delta t = 1.338 \times 10^{-9}$ s, and a large viscosity $\eta_\mu = 1\,\mathrm{kg/m \cdot s}$.

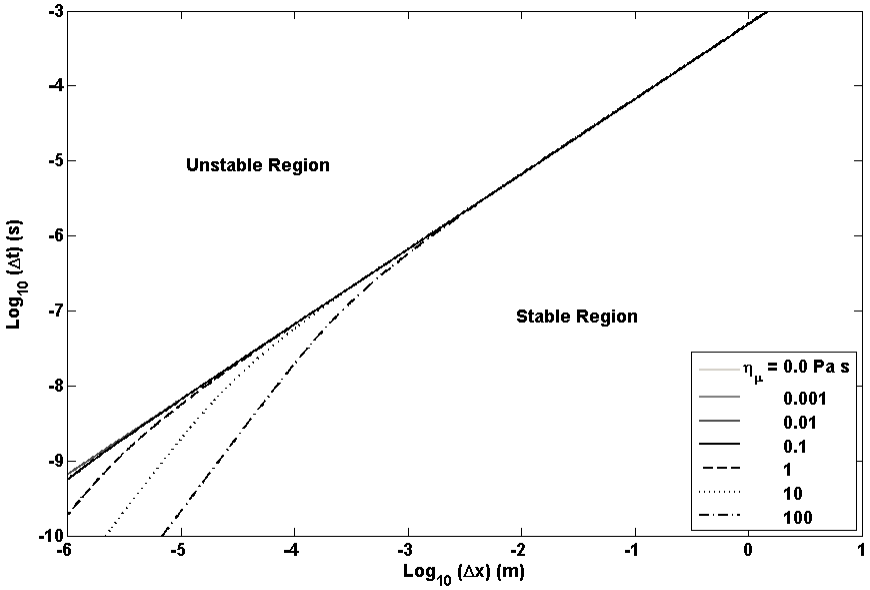

Figure 2-12: The stable and unstable regions for the linearized Navier-Stokes equations according to the von Neumann analysis.

Chapter 3

Determination of the Effective Elastic Properties of Digitized Rock Matrix

In seismic data interpretation, understanding the relationships between elastic properties of rocks, pore spaces and fluids is critical, and forms the basis for reservoir characterization and monitoring. Effective properties of porous rocks depend highly on pore spaces, solid phases and interactions between these two. To accurately predict the properties of rocks requires precise information of their complex micro-structures and the ability to computationally solve the large 3D problems.

Traditionally, researchers formulate empirical relationships statistically from laboratory experiments to help predict properties of rocks [e.g., Wyllie et al., 1956, 1958, Han, 1986]. However, such relationships are too simple to be predictive for a wide range of rocks and lack the detailed description of the micro-structures of rocks. Recently, the emergence of computational rock physics fills this gap and expands the research on rock physics in a new direction [e.g., Roberts and Garboczi, 2000, Arns et al., 2002, Grechka and Kachanov, 2006, Saenger, 2008].

With current advanced imaging techniques such as micro-computed tomography (μ-CT), micro X-ray CT [Flannery et al., 1987, Spanne et al., 1994], focused ion beam scanning electron microscopy (FIBSEM), laser confocal microscopy [Fredrich et al., 1995], and magnetic resonance imaging (MRI), we now are able to generate 3D digitized images of rocks in high resolution, the usual voxel resolution of which

is about 1-10 μm or even higher. Such high resolution images provide direct measurements of the complex morphology of porous rocks. Combining these with computational techniques, we can calculate the material properties such as diffusivity, elasticity, permeability and conductivity. The ultimate goal of the development of these computational experiments and methods is to supplement experiments, which have traditionally been carried out in laboratories and are time consuming and costly, with cheaper numerical experiments that allow the parameter space to be explored more thoroughly.

Two fundamental classes of numerical methods have been developed and used for studying rock properties: static and dynamic methods. Roberts and Garboczi [2000], Arns et al. [2002, 2007], Grechka and Kachanov [2006] and Madadi et al. [2009] used the finite-element method (FEM) to study the static effective elastic properties of porous media and rocks, while Saenger and Shapiro [2002], Saenger et al. [2004a,b, 2005, 2006], Masson et al. [2006], Saenger et al. [2007], Masson and Pride [2007], Saenger [2008] and Masson and Pride [2010] used the finite-difference method (FDM) to study the dynamic effective properties of porous and cracked rocks. Arns et al. [2002] carried out extensive numerical computations on 3D digitized rock samples of Fontainebleau sandstones with variable porosities and compared their numerical predictions to those from Gassmann's model and experimental measurements. They concluded that for such types of clean sandstone as Fontainebleau sandstone, elastic property-porosity relationships can be derived from microtomographic images. Arns et al. [2007] applied the same numerical method on poorly-cemented granular rocks and studied the effects of contact moduli on linear effective elastic properties of such rocks. Saenger et al. [2000] developed a finite-difference solver using rotated-staggered-grid scheme (RSG) and studied the dynamic responses of cracked rocks [Saenger and Shapiro, 2002, Saenger et al., 2004a], comparing the numerical results to those estimated by different effective medium theories. Saenger et al. [2005] extended the RSG scheme to incorporate the viscous effect of fluid and studied the Biot's effects of synthetic porous rocks. With the same solver, Saenger et al. [2006] and Saenger [2008] presented a new technique for computing the static effective elastic

properties and explained discrepancies between some numerical studies in terms of static and dynamic numerical experiments. In all of these computations, they claimed the numerical predictions can verify some theoretical models and even explain some experimental measurements.

The X-ray CT imaging technique is unable to obtain images of rocks with high enough resolution to illuminate every crack or micro-pore between and within grains for sandstones or carbonates. Even if it were able to do so, current computational resources limits our ability to solve such huge 3D problems on a realistic scale since the resolution required would be down to nanometer scale. Therefore, we generally lose small features of rocks during the imaging process, such as phase separation. Arns et al. [2007] realized this drawback of our current technique and tried to remedy it by introducing contact porosity for poorly-cemented sandstones. In their approach, they utilized microtomographic images and grain-partitioning techniques to assign grain moduli, then used effective medium theories locally to calculate the contact moduli between grains for phases such as clay.

However, we found that the loss of small features of rocks due to the imaging process not only affects poorly-cemented sandstones as Arns et al. [2007] discussed, but also well-cemented sandstones such as Fontainebleau sandstones and Berea sandstones. For example, in the paper by Arns et al. [2002], though the numerical predictions with 3D digitized rocks of Fontainebleau sandstones using FEM can match Gassmann's equations and experimental measurements well, we found that (1) the computed velocities for both dry and water/oil saturated cases are generally higher than experimental measurements; (2) velocities of P-waves for dry rocks are higher than those for water/oil saturated ones; this contradicts the intuitions and laboratory observations for sandstones. We also found the same contradicting phenomena in our own computations on digitized 3D Berea sandstones. One explanation Arns [2002] gave for such observations is that the periodic boundary condition is used in the FEM solver. However, we show below that this is not the real reason behind these observations.

In this chapter, we will discuss this problem and give an explanation for it. Then

we will propose a hybrid method — combining numerical computation with the differential effective media theory and the Kuster-Toksöz model — to resolve this issue. Finally, we will compute the effective elastic properties of rocks and compare these numerical predictions to laboratory measurements.

3.1 Numerical Predictions without Cracks

3.1.1 3D X-ray CT images of Berea sandstone

3D X-ray CT images for a cylindrical plug of Berea sandstone were obtained. The images have a total size of $1840 \times 1840 \times 1940$ pixels with resolution of 2.8 μm per pixel. Gray scale images from X-ray CT have been thresholded so as to separate them into two main phases: solid grain and pore space, respectively. From the original cylindrical plug, we extracted a cubic subset in the center with the size of $250 \times 250 \times 250$ pixels for analysis. In Figure 3-1, we show the gray scale CT images of the 250^3 pixels cubic subset, and in Figure 3-2, we show the corresponding segmented images for this same subset, in which grains are represented in red and pores are in blue. The porosity (ϕ) of this sample is about 19.2%. As concluded by Arns et al. [2002], the representative image volume for well-cemented Fontainebleau sandstone should be a 120^3 pixels cubic subset at resolution of 5.7 μm, which exactly corresponds to our sample with size of a 250^3 pixels at 2.8 μm.

3.1.2 Property predictions

We focus on the static effective properties of porous rocks as Arns et al. [2002] did on digitized 3D rocks with the finite-element method (FEM). We use the finite-element solver from NIST (National Institute of Standards and Technology) [Garboczi and Day, 1995, Garboczi, 1998] to estimate the effective elastic properties of the Berea sandstone represented by the 250^3 pixels cubic subset. FEM solves the weak form of the linear elastic equations and utilizes iterative solvers such as conjugate-gradient method to find the solutions. In FEM, each pixel is taken to be a trilinear finite

element and constant strain boundary conditions are applied. The effective elastic properties are obtained from average stresses and strains.

In the computation, we first assume the grains are occupied by pure quartz with bulk modulus $K = 37$ GPa, shear modulus $\mu = 44$ GPa and mineral density $\rho = 2650\,\mathrm{kg/m^3}$ [Mavko et al., 1998]. We model dry and water-saturated cases at 40 MPa pressure where $K_{\mathrm{water}} = 2.2$ GPa, $\mu_{\mathrm{water}} = 0$ GPa and $\rho_{\mathrm{water}} = 1000\,\mathrm{kg/m^3}$ [Han, 1986]. The numerically predicted results for effective bulk $\langle K \rangle$ and shear $\langle \mu \rangle$ moduli and velocities of P- and S-waves are listed in Table 3.1. In Table 3.2, we list some laboratory measurements on Berea sandstones with similar porosities at 40 MPa as the one we used in this study for comparison where pulse-echo technique was employed to measure the velocities [Winkler, 1985, Han, 1986]. At 40 MPa pressure, Winkler [1985] and Han [1986] both concluded that velocity dispersion due to fluids was so small as to be able to be ignored. Although the numerical predictions for dry and water-saturated cases satisfy Gassmann's equation as Arns et al. [2002] demonstrated, we can see that the numerical predictions from FEM generally overestimate the effective elastic properties resulting in large velocities in general. Also P-wave velocity predicted in water-saturated case is less than that for dry case, which usually occurs only for well-sintered glass beads packs. This indicates that in our numerical computations, the bulk modulus of water contributes less to the final effective properties, but the effect of density takes over in the computation.

3.2 Crack Loss in Imaging Process

The reason for the overestimates of numerical predictions is the loss of micro-structures of rocks in X-ray CT scanning and the image segmentation afterwards. As we know, small features like cracks or micro-pores in rocks are mostly in nanometer scale [Murphy et al., 1986]. Although the X-ray CT technique can provide high resolution images in micrometer scale, compared to small features in nanometer scale, its resolution is still too low to resolve the micro-structures when we digitize rocks into CT images and separate phases afterwards. Realizing these issues with the imaging

process, Arns et al. [2007] introduced the concept of contact porosity to estimate the contact moduli between grains with effective medium theories, and Knackstedt et al. [2009] utilized SEM images, which have much higher resolution than CT images, to recover lost micro-pores. For the samples of Berea sandstone we used in our study, we are facing the same issues. Shown in Figure 3-3a is a 2D slice of X-ray CT image cut from the 3D volume of the digitized Berea sandstone. The arrows in Figure 3-3a indicate cracks between grain contacts that are lost during the segmentation process. As shown in Figure 3-3b, after segmentation, we obtain a rock with continuous matrix where no micro-structures between grains are resolved. As expected, the continuous matrix without cracks resulting from segmentation strengthens the rock frame and contributes to the over-predicted effective elastic properties of digitized rocks. Besides cracks, although there should have been other micro-structures lost in the imaging process, we only study the effects of cracks since we believe they have the most impact on the effective elastic properties of rocks as already discussed by many researchers [e.g., Walsh, 1965, Kuster and Toksöz, 1974, O'Connell and Budiansky, 1977, Hudson, 1980].

3.3 Effects of Cracks on Digitized Rock Matrix

As discussed in the previous section, we believe that the loss of cracks during the imaging process is the main cause of higher predicted effective elastic properties of rocks. Therefore, we have to modify the continuous matrix of digitized rocks by taking the cracks into account. To accomplish this, effective medium theories are used along with computational approach. In Section 3.1.2, we have calculated the velocities of P- and S-waves of Berea sandstone for dry and water-saturated cases with the continuous rock matrix without cracks; the results are much higher than the laboratory measurements. In order to recover cracks in the continuous matrix, we carry out a Monte-Carlo inversion on numerical predicted properties of rocks listed in Table 3.1.

3.3.1 Effective medium theories

Note that instead of working on the continuous matrix directly to invert crack distribution, we first start with the numerically predicted effective moduli of the rock frame. According to the differential effective medium theory (DEM), for a composite consisting of two phases, by choosing a preferred host material, we can incrementally add other phases or inclusions into the host. For the composite host medium at some porosity value ϕ , the effective moduli $K^*(\phi + d\phi)$ and $\mu^*(\phi + d\phi)$ after a small portion of the composite host has been replaced by inclusions of the other phase can be obtained by

$$(1-\phi)\frac{d}{d\phi}\left[K^*(\phi)\right] = (K_i - K^*)P^* \tag{3.1}$$

$$(1-\phi)\frac{d}{d\phi}\left[\mu^*(\phi)\right] = (\mu_i - \mu^*)Q^* \tag{3.2}$$

where $K^*(\phi)$ and $\mu^*(\phi)$ are the effective moduli to be estimated after adding a small portion of the second phase, K_i and μ_i are moduli of the second phase, and P^* and Q^* are geometric factors that depend on the shapes of inclusions of the second phase [Berryman, 1992, Mavko et al., 1998].

Returning to our cases, at the beginning we could treat pure quartz as the host that occupies the whole cubic domain without pores and cracks, and the pore spaces resolved and cracks lost in the imaging process as the second phase to be added into the host of quartz. There are two ways of adding pores and cracks into host according to the DEM: we can add pore spaces first, followed by cracks, or vice verse. In practice, the final effective elastic properties obtained from these two different ways of adding the second phase can be quite different for some cases. The numerical predictions in Table 3.1 can be taken as the intermediate effective properties of rocks after only adding pore spaces. Therefore, starting with these results, we can invert distribution of cracks that should have existed in continuous matrix by using the Kuster-Toksöz model [Kuster and Toksöz, 1974; see details in Appendix D].

3.3.2 Monte-Carlo inversion with the Kuster-Toksöz model

According to the DEM model, the numerical predictions listed in Table 3.1 can be thought of as the intermediate effective moduli of the Berea sandstone by only taking into account pores resolved from the imaging process. Cracks lost in this process can be added into the continuous matrix as the rest of the portion of the second phase defined in the DEM model. Taking the saturated Berea sandstone in the intermediate stage of DEM model as an isotropic and homogeneous elastic block and using the Kuster-Toksöz model, we can invert the distributions of spheroidal cracks with a Monte-Carlo inversion by fitting the laboratory measurements of velocities of P- and S-waves. For the laboratory data, we choose only those for dry and water-saturated cases in Table 3.2 measured by Han [1986]. Since the laboratory data were measured at 40 MPa pressure, we believe most cracks with a smaller aspect ratio ($< 10^{-5}$) are closed by pressure [Toksöz et al., 1976]. Therefore, in the Monte-Carlo inversion, we choose 4 sets of cracks with initial aspect ratios α_0 and maximum concentrations $c_{\max}$, respectively

$$\alpha_0 = \left[(5 \pm 2.5) \times 10^{-2},\ (1 \pm 0.5) \times 10^{-2},\ (5 \pm 2.5) \times 10^{-3},\ (1 \pm 0.5) \times 10^{-3}\right] \quad (3.3)$$

$$c_{\max} = \left[5 \times 10^{-2},\ 5 \times 10^{-3},\ 1 \times 10^{-4},\ 1 \times 10^{-5}\right] \quad (3.4)$$

Note that we allow the values of aspect ratio corresponding to each set of cracks to vary within some specific range as defined above. We ran 100 Monte-Carlo inversions, in each of which 100000 trials were computed. We use L_2-norm to measure the error between the computed P- and S-wave velocities and laboratory measurements for dry and water-saturated cases . The best set of cracks with minimum error was chosen out of these 100 best solutions as the final inverted result. Listed in Table 3.3 are the best solutions for aspect ratio and concentration of cracks after inversion. We can see that adding a small amount of cracks, especially those with small aspect ratios, can

affect elastic properties of rocks significantly. By adding the inverted set of cracks into Berea sandstone according to the DEM and Kuster-Toksöz models, we can obtain the final P- and S-wave velocities for dry: $V_p = 3957$ m/s, $V_s = 2647$ m/s; water: $V_p = 4119$ m/s, $V_s = 2600$ m/s, which are close to the laboratory measurements by Han [1986].

3.3.3 Numerical predictions with cracked digitized matrix

We have discussed the effects of cracks lost on the effective properties of porous medium from a computational approach and inverted a set of cracks with laboratory measurements based on the DEM and Kuster-Toksöz models. To carry out computations on digitized rocks by taking cracks into account, alternatively, we can first add cracks into the host of quartz to soften the matrix of the rock. Then we can saturate the pore spaces resolved in the imaging process and compute the total effective elastic properties at the end. This sequence of adding inclusions or second phase is opposite to what we did in Section 3.3.2. According to the DEM model, the effective properties of composite, which depend on the sequence of adding different inclusions, generally could be different, but can be quite close in some cases.

Saturating the cracks inverted in the previous Section 3.3.2 with dry, water, brine and oil, and adding them into quartz by using the Kuster-Toksöz model, we can obtain the effective elastic properties of the new continuous matrix as listed in Table 3.4. Here we choose properties for brine: $K_{\text{brine}} = 2.51$ GPa, $\mu_{\text{brine}} = 0$ GPa and $\rho_{\text{brine}} = 1040\text{kg/m}^3$; oil: $K_{\text{oil}} = 2.16$ GPa, $\mu_{\text{oil}} = 0$ GPa and $\rho_{\text{oil}} = 890\text{kg/m}^3$ [Winkler, 1985]. Since Berea sandstone is not as clear as Fontainebleau sandstone, saturating brine can change micro-structures of pore spaces by changing the morphology of clay. Therefore we reduce 5% of the shear modulus of quartz when saturating with brine so as to take into account the effect of clay [Toksöz et al., 1976].

Assigning the values of effective elastic properties in Table 3.4 to solid grains of the 3D digitized Berea sandstone shown in red in Figure 3-2, we use the FEM solver to compute the final effective properties for cases saturated with different fluids. The final results are listed in Table 3.5 where we put the computed results side by side

with laboratory measurements of Winkler [1985] and Han [1986] for comparison. The values in percentage below the laboratory data are errors between computed velocities and corresponding laboratory measurements. We can see from these small errors that (1) our newly predicted velocities match laboratory measurements quite well for all four cases; (2) since we inverted the distribution of cracks only with the laboratory measurements by Han [1986] for dry and water-saturated cases, the good match between computed results for these two cases and the laboratory measurements should be within expectation; this also indicates that the sequences of adding inclusions defined by DEM model does not lead to much different results; (3) importantly, by adding cracks inverted from dry and water-saturated cases based on the measurements by Han [1986], we can predict the effective properties of brine and oil-saturated rocks well enough so as to match the laboratory measurements by Winkler [1985]. In Figure 3-4, we conclude the procedure employed above to predict the effective elastic properties of rocks by taking into account cracks lost in the imaging process. Note that the rock we use here has porosity of 19.2%, and we think the inverted results can only apply to rocks with similar porosity.

Table 3.1: Numerical predictions from finite-element simulation for the digitized Berea sandstone without cracks.

	$\langle K \rangle$ (GPa)	$\langle \mu \rangle$ (GPa)	V_p (m/s)	V_s (m/s)
Dry	20.6	20.3	4717	3678
Water	23.0	20.6	4640	2964

Table 3.2: Laboratory measurements of velocities on Berea sandstones with similar porosities at 40 MPa [Winkler, 1985, Han, 1986].(unit: m/s)

	porosity (%)	Dry		Water		Brine		Oil	
		V_p	V_s	V_p	V_s	V_p	V_s	V_p	V_s
Han (1986)	20.3	4040	2620	4150	2510				
Winkler (1985)	19.0	3963	2527			4044	2417	4189	2521

Table 3.3: The set of cracks from Monte-Carlo inversion at 40 MPa.

Aspect Ratio (α)	$[6.62 \times 10^{-2}, 1.36 \times 10^{-2}, 3.13 \times 10^{-3}, 9.09 \times 10^{-4}]$
Concentration (c)	$[4.50 \times 10^{-2}, 1.30 \times 10^{-3}, 3.26 \times 10^{-5}, 5.01 \times 10^{-6}]$

Table 3.4: Effective elastic properties of continuous matrix with cracks included at 40 MPa.

	$\langle K \rangle$ (GPa)	$\langle \mu \rangle$ (GPa)
Dry	24.1	30.3
Water	28.6	31.6
Brine	28.7	30.3
Oil	28.6	31.6

Table 3.5: Comparison of computed effective properties of the 3D digitized Berea sandstone with laboratory data for different fluid saturation at 40MPa. (unit: m/s)

	Computed				Laboratory			
	$\langle K \rangle$ (GPa)	$\langle \mu \rangle$ (GPa)	V_p	V_s	Han (1986)		Winkler (1985)	
					V_p	V_s	V_p	V_s
Dry	13.6	13.9	3989	2624	4040	2620	3963	2527
					-1.27%	0.13%	0.65%	3.81%
Water	17.8	14.9	4085	2569	4150	2521		
					-1.56%	1.9%		
Brine	18.1	14.3	4052	2516			4044	2417
							0.19%	4.08%
Oil	17.7	14.9	4105	2583			4189	2521
							-2.01%	2.46%

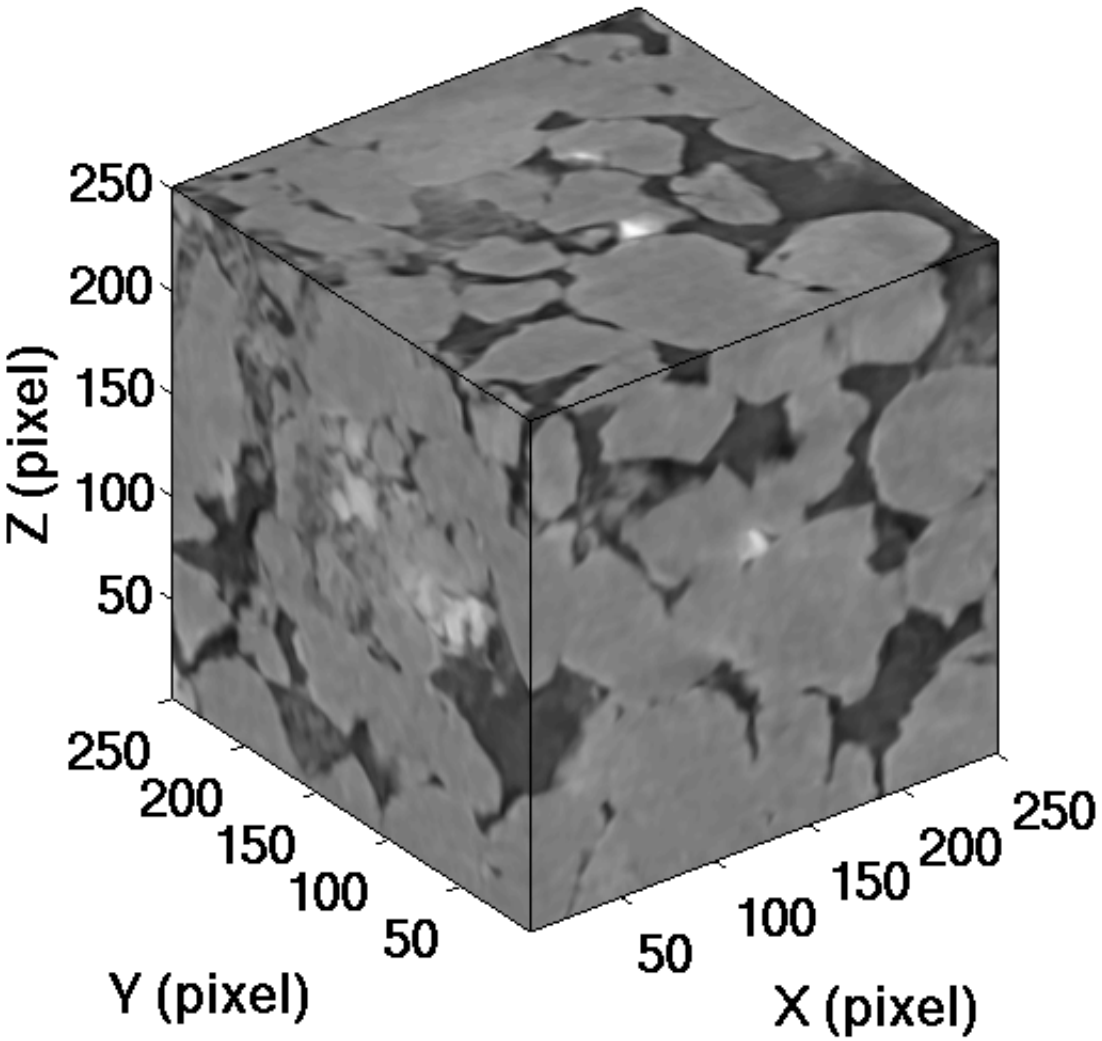

Figure 3-1: Gray scale X-ray CT images for the 250^3 pixels cubic subset of a Berea sandstone.

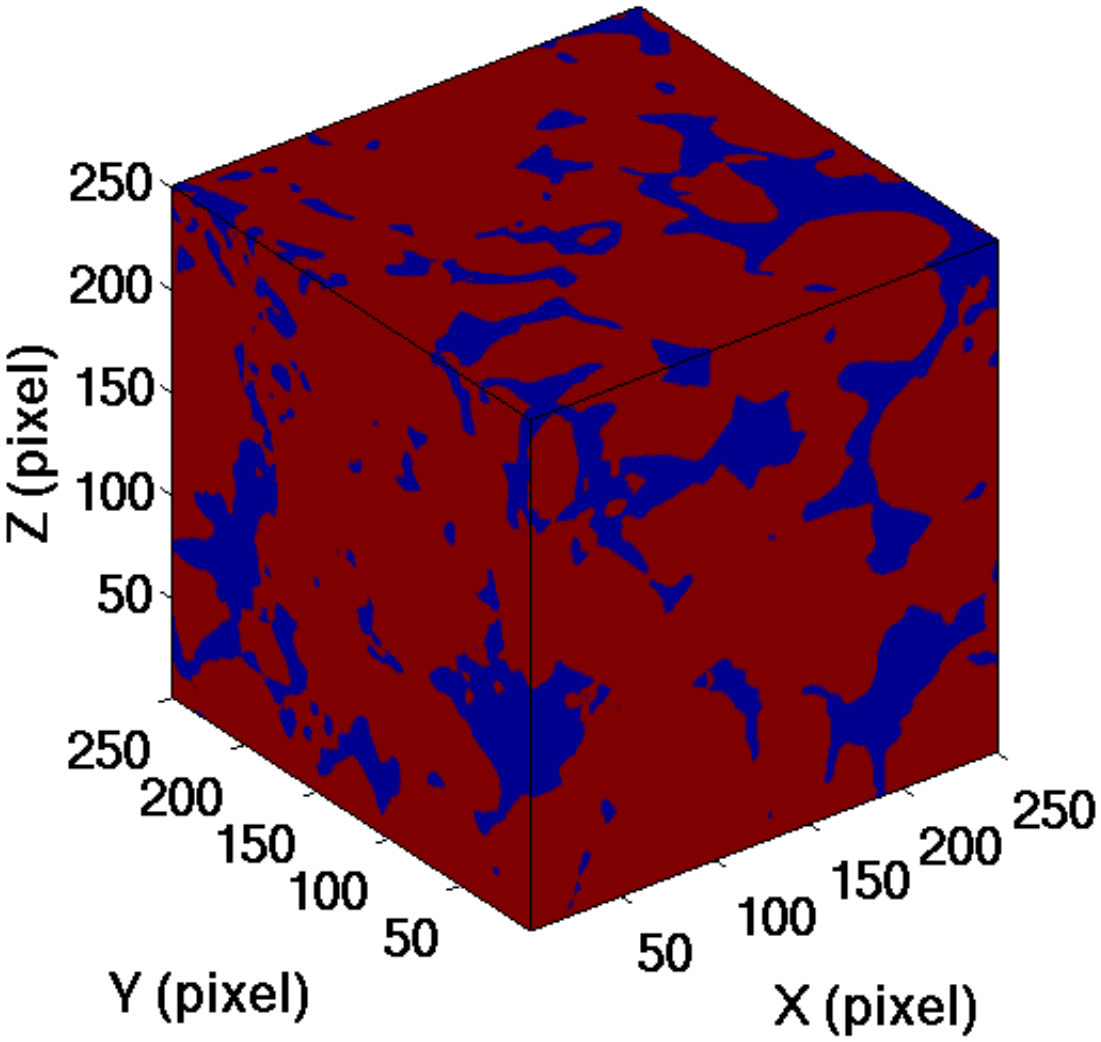

Figure 3-2: Segmented images for the 250^3 pixels cubic subset of a Berea sandstone. Grains are represented in red and pores are in blue.

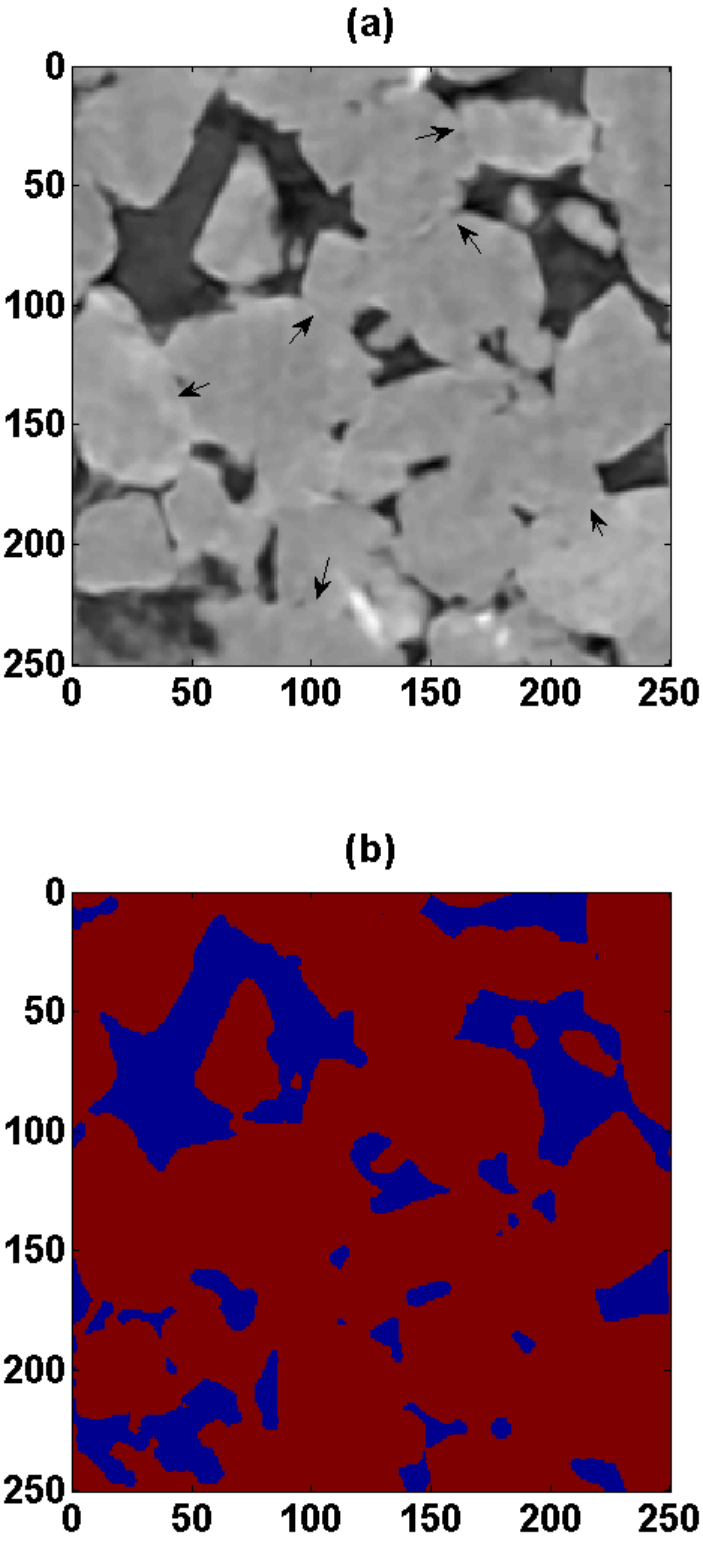

Figure 3-3: 2D slices of digitized Berea sandstone. (a) X-ray CT image in gray scale; (b) segmented image. We can clearly see the loss of cracks between grain contacts due to the imaging process, as indicated by arrows in (a).

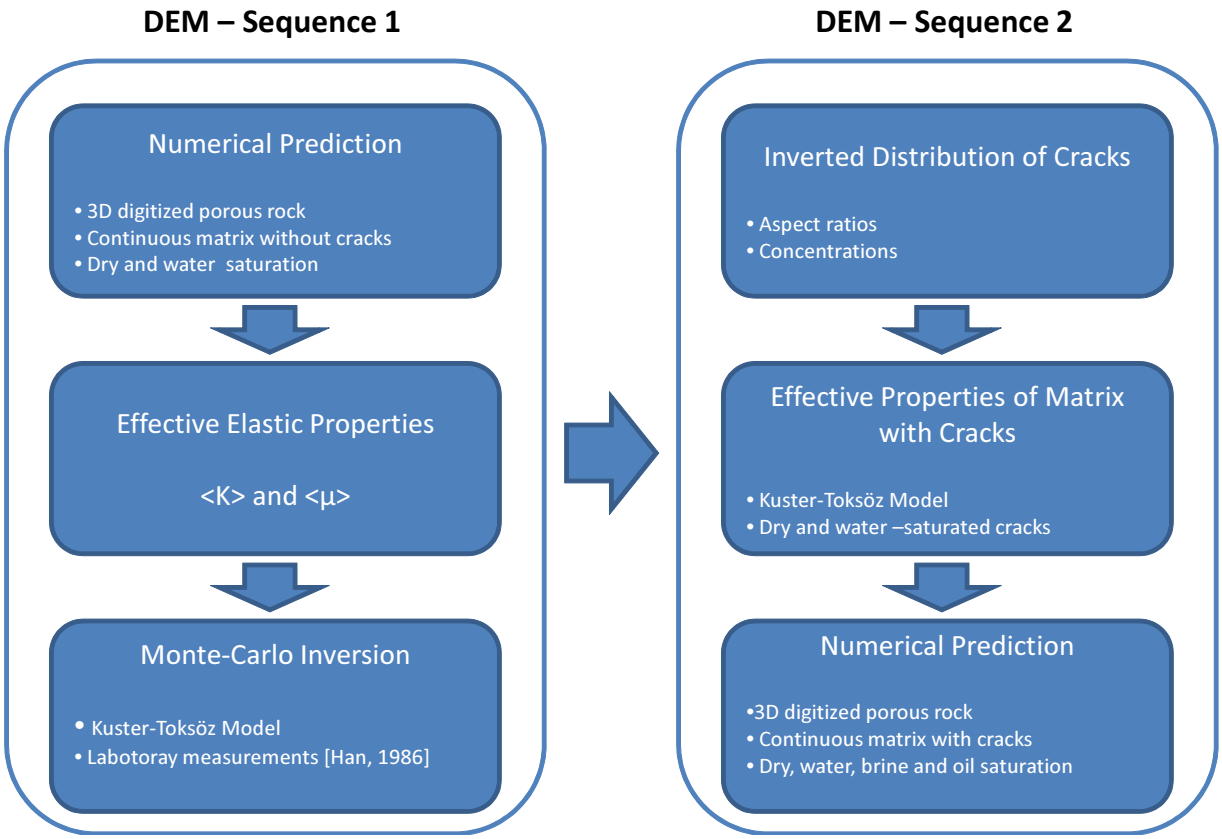

Figure 3-4: Flow chart for the procedure to predict the effective elastic properties of 3D digitized porous rocks with cracked matrix.

Chapter 4

Computation of Seismic Responses to Viscous Fluid in Pores and Cracks

Seismic dispersion and attenuation of porous rocks saturated with fluids have been of interest to geophysicists for many years. Understanding the intrinsic mechanism causing dispersion and attenuation is not only an academic topic but also an industrial one, which can guide us to better analyze the seismic data collected and help to decipher the geological information underneath. Researchers have been carrying out laboratory and field measurements on different types of rocks from small to large scale so as to directly gain observations and build empirical relationships [e.g., Nur and Simmons, 1969, Toksöz et al., 1976, 1979, Winkler and Nur, 1979a, Winkler et al., 1979, Winkler and Nur, 1979b, Murphy, 1982, Winkler and Plona, 1982, Murphy, 1984, Winkler, 1985, Han, 1986, Murphy et al., 1986, Wang and Nur, 1990, Batzle et al., 2006]. Meanwhile, others have been developing mathematical theories and models to explain what have been observed [e.g., Biot, 1956a,b, Walsh, 1965, Kuster and Toksöz, 1974, O'Connell and Budiansky, 1977, Johnston et al., 1979, Gurevich and Lopatnikov, 1991, Berryman, 1992, Dvorkin and Nur, 1993, Dvorkin et al., 1994, 1995, Gurevich et al., 1997, 1999, Gurevich, 2002, Pride and Berryman, 2003a,b, Pride et al., 2004, Muller and Gurevich, 2005, Galvin and Gurevich, 2006, 2007, Gurevich et al., 2008, Müller et al., 2008, Galvin and Gurevich, 2009, Gurevich et al., 2009a,b].

Amongst this work, laboratory experiments that significantly contribute to our

knowledge of the dynamic responses of saturated porous rocks are the most important part. Depending on the frequency range of interest, several different techniques can be used to measure the responses of waves to porous rocks in the laboratory. Pulse-echo [Winkler and Plona, 1982] and ultrasonic pulse transmission [Toksöz et al., 1979] techniques have been used in the laboratory for frequency at the range of megahertz on smaller samples, and the resonant bar technique [Peselnick and Outerbridge, 1961, Tittmann, 1977, Winkler et al., 1979, Winkler and Nur, 1979a] has been employed for frequency at the range of kilohertz and lower, though this requires longer samples. For frequency well off the resonance frequency, stress-strain measurement has been carried out in the laboratory to record the stress-strain behavior of rocks [Gordon and Davis, 1968, McKavanagh and Stacey, 1974, Peselnick and Outerbridge, 1961, Batzle et al., 2006]. Dispersion and attenuation of rocks can be extracted from data measured by these different techniques in different ways. The general observations in the laboratory for sandstones are (1) for dry rocks, velocity and attenuation show little or no frequency dependence; (2) for fluid saturated rocks, velocity increases with frequency while attenuation increases generally with frequency but might drop after some characteristic frequency.

Parallel with the laboratory work, different theories and models have been developed to explain the physics causing such dispersions and attenuations. Biot [1956a, 1956b] developed a theory of wave propagation in saturated porous rocks based on a macroscopic fluid-flow model. In both low- and high-frequency limits, Biot's theory predicts little dispersion and attenuation [Winkler, 1985, Han, 1986, Winkler, 1986, Wang and Nur, 1990]. Mavko and Nur [1975] and O'Connell and Budiansky [1977] proposed squirt-flow models to accommodate pore-scale fluid flow and explain the dispersion and attenuation induced. Based on the Biot and squirt-flow models, Dvorkin and Nur [1993] developed the BISQ (BIot-SQuirt) model to unify the Biot and squirt-flow mechanism. Dvorkin et al. [1994] showed special cases of squirt-flow at low and high frequencies and compared them with the BISQ model. Dvorkin et al. [1995] extended the BISQ model to fully saturated rocks. For heterogeneous rocks, Berryman and Wang [1995, 2000] came up with a double-porosity, dual-permeability

model to capture the reality that stiff spherical pores and compliant cracks are coexistent within one rock. Pride and Berryman [2003a,b] derived a system of equations to describe the linear dynamics of double-porosity and dual-permeability materials in terms of acoustic attenuation and fluid transportation. Pride et al. [2004] proposed a unified theory to treat P-wave attenuation that covers mesoscopic and microscopic scales in sedimentary rocks. Meanwhile, Gurevich and Lopatnikov [1991], Gurevich et al. [1997], Gurevich [2002], Muller and Gurevich [2005], Galvin and Gurevich [2006, 2007], Müller et al. [2008], Galvin and Gurevich [2009], Gurevich et al. [2009a,b] also developed mathematical theories to study wave dispersion and attenuation due to wave-induced fluid flow at the presence of fractures in otherwise porous rocks.

Besides the laboratory experiments and developments of mathematical theories, recently researchers have begun to take advantage of computational techniques to study the effects of fluids on dispersion and attenuation. As described in Chapter 3, Roberts and Garboczi [2000], Arns et al. [2002, 2007], Grechka and Kachanov [2006] and Madadi et al. [2009] studied the static effective elastic properties of dry and fluid-saturated porous rocks with finite-element method (FEM), while Saenger and Shapiro [2002], Saenger et al. [2004a,b, 2006] and Saenger [2008] used finite-difference method (FDM) to study the dynamic effective properties of porous and cracked rocks, in both of which fluid was assumed to be nonviscous. Saenger et al. [2005] extended the finite-difference method with RSG scheme to incorporate the viscous effect of fluid and studied the Biot's effects of synthetic porous rocks with pore scale simulation. Based on Biot's poroelasticity theory [Biot, 1956a,b], Masson et al. [2006], Masson and Pride [2007, 2010] published a series papers about their work on developing a time-domain finite-difference solver to study seismic attenuation and dispersion across all frequencies due to wave-induced fluid flow in rocks with mesoscopic scale heterogeneities. Rubino et al. [2009] studied the same problems for heterogeneous, fluid-saturated porous rocks by solving coupled Biot's equations with the finite-element method in frequency domain.

The low-frequency responses of fluid-saturated porous rocks interest geophysicists the most. Researchers believe that even in the low frequency range such as in the

seismic band, we can still observe non-negligible dispersion and attenuation, which is highly dependent on fluid mobility and the distributions of heterogeneity in rocks [Gurevich et al., 1997, Gurevich, 2002, Pride and Berryman, 2003a,b, Pride et al., 2004, Muller and Gurevich, 2005, Galvin and Gurevich, 2006, 2007, Müller et al., 2008, Galvin and Gurevich, 2009]. Generally, stress-strain measurement has been used either in laboratory experiments or numerical computations to obtain such low-frequency responses [Batzle et al., 2006, Masson et al., 2006, Masson and Pride, 2007, Rubino et al., 2009, Masson and Pride, 2010]. However, limited by the assumptions made in Biot's poroelasticity theory, the low-frequency responses obtained from any computation based on the poroelasticity theory can represent only the Biot-type mechanism. The squirt-flow effect is not included. The porous rocks synthesized statistically as heterogeneous poroelastic media do not preserve the detailed microstructures of pore spaces as well.

In this chapter, we will first demonstrate the particle motion on microscale for a 2D slice of digitized rock so as to intuit from where frequency-dependent seismic responses come; then, introducing the stress-strain calculation, we utilize numerical computation to measure the low-frequency responses of saturated digitized porous rocks and study the effects of viscous fluids on seismic dispersion and attenuation. Since only two phases — solid matrix and fluid inclusion — are considered in our simulation, friction, the dominant mechanism of attenuation in sandstones due to cracks within and between grains, cannot be captured. To compensate for the missing attenuation due to friction and viscous fluid in compliant pores, we further extend the hybrid method introduced in Chapter 3 by utilizing the modified squirt-flow model. The final computed velocities and attenuations for different fluids are compared with laboratory measurements.

4.1 Particle Motion on Microscale

When considering the acoustical properties of granular materials, even "homogeneous" samples exhibit a wide variety of microstructural features capable of influ-

encing wave propagation. Materials such as quartz and clay in a rock sample can be treated as heterogeneities; pores saturated with fluids between them can have different sizes and shapes. In laboratory experiments, seismic waves propagating at high frequencies are more sensitive to these pore-scale features. Particle motion on microscale in the fluid and solid phases controls the dispersion and attenuation of wavefields on macroscale. We begin with the fundamental physics — the particle motions of the fluid and solid phases on microscale, which helps us to understand how seismic waves propagate through porous media, and how microstructural features can modify the signal. To explore this topic, we will carry out a set of numerical experiments with a digitized 2D image of a loose sample of beach sand and show the interactions between fluid and solid on microscale as a function of frequency.

4.1.1 2D digitized sample

In our modeling study, we used a segmented 2D transmission micrograph of a quartz beach sand (San Gregorio, CA), shown in Figure 4-1. The binary model shown has dimensions of 551×496 pixels with the resolution at 2.4 μm per pixel. Since the original sample consisted of a loose arrangement of grains epoxied to a slide, the solid phase (shown in black) is not continuous and the resulting model should be viewed as a suspension. For our modeling study we assume the grains are pure quartz with a density of 2650 kg/m^3 and bulk and shear moduli of 37 and 44 GPa, respectively [Mavko et al., 1998]. We use the properties of water for the liquid phase, with bulk modulus of 2.2 GPa and density of 1000 kg/m^3. In 2D modeling, the effects of fluid viscosity are not explicitly included.

4.1.2 2D numerical modeling

In our numerical modeling, we used the linear solver developed in Chapter 2. Since the RSG approach can effectively incorporate high material contrast, the method is well-adapted for modeling the sharp interfaces between grains and the surrounding pore fluids. For computational purpose, we put water buffer zones around the 2D

model (shown in Figure 4-2) and used a periodic boundary along the vertical direction. A perfectly-matched-layer (PML) absorbing boundary condition was applied at both ends of the sample in the horizontal direction. We modeled a compressional plane wave propagating in the x-direction from the right side of the sample as shown in Figure 4-2. The 2D sample acts like a filter converting the incident wave into a transmitted wave, which is altered by the micro-structures and inclusions of the sample. Since the size and shape of the quartz, pores and channels vary in different scales, frequency-dependent seismic phenomena occur when seismic waves travel through such a sample. For this reason, we considered three sources with three different frequencies - 2.5 MHz, 6.7 MHz and 20 MHz, the equivalent wavelengths of which are on the scales of the larger quartz grains, medium quartz grains, and small inter-grain channels in this sample, respectively.

4.1.3 Relative particle motion

Because water is much more compliant than quartz, the same body force can generate higher perturbations in the water as compared to those in grains, as seen in Figure 4-3. The larger particle motions in water generate a vigorous change of the pressure field, especially at high frequency. As a result, pressure changes in the water affect the solid phase, and cause stress concentrations on the sharp tips and corners of grains. This kind of perturbation and stress concentration contributes to dynamic changes in the mechanical properties of the rock sample during wave propagation. We can see that the velocity field is generally large in narrow channels because a pressure field with relative higher gradient has been developed there. Also shown in Figure 4-3, in the case where a low frequency source is used, the particle motion exhibits more coherent variation — longer wavelengths average over larger regions of the sample. When the center frequency of the source wavelet is increased, the motions of particles become disordered and random, especially in water.

The different responses of particle motion on microscale to different frequencies gives rise to frequency-dependent seismic properties of saturated porous rocks such as velocity dispersion and attenuation. We used relatively high frequencies (way above

1MHz) in numerical modeling where transmission experiments can be carried out on such a small rock sample. Limited by computational resources and the resolution of digitized rocks, the sizes of rocks that can be simulated are usually much smaller than the seismic wavelength of interest. Therefore, the transmission experiment is no longer approximate for numerical modeling and a new numerical calculation needs to be developed for this purpose.

4.2 Seismic Responses of 2D Digitized Rocks

4.2.1 Frequency-dependent velocity and attenuation in 2D

To obtain the frequency-dependent responses of saturated rocks in terms of velocity and attenuation, we have to first determine the complex bulk modulus $K(\omega)$ and shear modulus $\mu(\omega)$ according to the Hooke's law in frequency domain

$$\dot{\boldsymbol{\sigma}}(\omega) = K(\omega)\,\dot{\boldsymbol{\varepsilon}}(\omega)\,\boldsymbol{I} + 2\mu(\omega)\left[\dot{\boldsymbol{\varepsilon}}(\omega) - \frac{1}{3}\dot{\boldsymbol{\varepsilon}}(\omega)\,\boldsymbol{I}\right] \tag{4.1}$$

where $\dot{\boldsymbol{\sigma}}(\omega)$ and $\dot{\boldsymbol{\varepsilon}}(\omega)$ are stress and strain rate tensors, respectively.

Assuming plane strain condition, a 2D modeling is equivalent to a 3D case where no strain out of the plane of modeling is allowed, i.e., where $\dot{\varepsilon}_{yy} = 0$. Under this assumption and from equation (4.1), the 3D elastic bulk modulus $K^{3D}(\omega)$ can be obtained from the relation

$$K^{3D}(\omega) = K^{2D}(\omega) - \frac{1}{3}\mu^{3D}(\omega) \tag{4.2}$$

where 2D bulk modulus $K^{2D}(\omega)$ is determined from a pure compression calculation as shown in Figure 4-5a by

$$K^{2D}(\omega) = \frac{1}{2}\left(\frac{\dot{\sigma}_{xx} + \dot{\sigma}_{zz}}{\dot{\varepsilon}_{xx} + \dot{\varepsilon}_{zz}}\right) \tag{4.3}$$

while Figure 4-5b shows a pure shear calculation, the 3D shear modulus $\mu^{3D}(\omega)$ is obtained by

$$\mu^{3D}(\omega) = \frac{1}{2}\frac{\dot{\sigma}_{xz}}{\dot{\varepsilon}_{xz}} \tag{4.4}$$

Due to the viscous effects of fluids, the bulk and shear moduli exhibit frequency dependence, which causes velocity dispersion and attenuation. In our computation, once we obtain these two frequency dependent moduli, we can easily determine the complex velocities by [Carcione, 2001]

$$V_{P_c}(\omega) = \sqrt{\frac{K^{3D}(\omega) + \frac{4}{3}\mu^{3D}(\omega)}{\bar{\rho}}} \tag{4.5}$$

$$V_{S_c}(\omega) = \sqrt{\frac{\mu^{3D}(\omega)}{\bar{\rho}}} \tag{4.6}$$

where $\bar{\rho}$ is the average bulk density of the saturated porous rock. Following the relations below, we can estimate the equivalent phase velocities by [Carcione, 2001]

$$V_P(\omega) = \left[\mathbf{Re}\left(\frac{1}{V_{P_c}(\omega)}\right)\right]^{-1} \tag{4.7}$$

$$V_S(\omega) = \left[\mathbf{Re}\left(\frac{1}{V_{S_c}(\omega)}\right)\right]^{-1} \tag{4.8}$$

O'Connell and Budiansky [1977] showed that the inverse quality factor Q^{-1} which measures the total energy loss per cycle has to be defined as the ratio of the imaginary and real parts of the complex elastic modulus involved. Represented in term of complex velocities, Q^{-1} for P- and S-waves can be expressed as

$$Q_P^{-1} = \frac{\mathbf{Im}\left(V_{P_c}(\omega)^2\right)}{\mathbf{Re}\left(V_{P_c}(\omega)^2\right)} \tag{4.9}$$

$$Q_S^{-1} = \frac{\mathbf{Im}\left(V_{S_c}(\omega)^2\right)}{\mathbf{Re}\left(V_{S_c}(\omega)^2\right)} \tag{4.10}$$

4.2.2 Stress-strain calculation in 2D

Since the typical size of the digitized rocks we can currently solve for is several orders of magnitude smaller than the seismic wavelength in which we are interested, it is almost computationally impossible to model the full wave propagating through such a tiny chunk of rocks, especially for those at lower frequencies, which can be computationally inefficient. Instead, following Masson and Pride [2007] and Rubino et al. [2009], we utilize a stress-strain calculation to study the seismic responses so as to estimate the velocity dispersion and attenuation. In such a way, it is possible for us to extract information on low-frequency responses from smaller rocks. To obtain the frequency-dependent bulk and shear moduli from 2D rocks, we carry out two independent calculations - pure compression and pure shear calculations as shown in Figure 4-5. In both of these calculations, prescribed velocity or equivalent strain boundary conditions are applied along four edges. The time function for these boundary conditions is chosen to be a sinusoidal wave. However, to ensure that the final measured strain is on the order of 10^{-6} or less as usually observed for seismic waves, we have to modify the sinusoidal velocity boundary conditions to be $\mathbf{v}(t) = A\omega \sin(\omega t)$, the corresponding displacement of which after integration in time has the form of $\mathbf{u}(t) = -A\cos(\omega t)$. Amplitude, A, controls the maximum strain we can achieve in numerical modeling, and angular frequency, ω, specifies the frequency content in which we are interested. We prefer to simulate one frequency at a time so as to raise the signal-to-noise ratio in the results.

In the stress-strain calculation on saturated porous rocks, we actually study the average seismic responses of rocks as a whole. Therefore, during the numerical modeling, we record the average fields of stress and strain rates throughout the whole sample at every time step

$$\langle \dot{\boldsymbol{\sigma}}(t) \rangle = \frac{1}{MNK} \sum \dot{\boldsymbol{\sigma}}(t) \tag{4.11}$$

$$\langle \dot{\boldsymbol{\varepsilon}}(t) \rangle = \frac{1}{MNK} \sum \dot{\boldsymbol{\varepsilon}}(t) \tag{4.12}$$

where MNK is the total number of grids in the finite-difference modeling. Finally, once we obtain these averaged fields, we can use the Fourier transformation (FT) to compute the corresponding responses in frequency domain

$$\dot{\boldsymbol{\sigma}}(\omega) = \mathrm{FT}\left\{\langle \dot{\boldsymbol{\sigma}}(t) \rangle\right\} \tag{4.13}$$

$$\dot{\boldsymbol{\varepsilon}}(\omega) = \mathrm{FT}\left\{\langle \dot{\boldsymbol{\varepsilon}}(t) \rangle\right\} \tag{4.14}$$

In the real computation, the fast Fourier transformation (FFT) is used.

As an example, we apply this stress-strain calculation to an isotropic and homogeneous 2D elastic solid sample. The bulk and shear moduli of this sample are: $K = 37$ GPa and $\mu = 44$ GPa. The size of the sample is 250×250 pixels at resolution of 2.8 μm. Sinusoidal velocity boundary conditions at 10 kHz and 100 kHz are applied, respectively, and a total of 5 cycles is simulated. Shown in Figure 4-6 are the measured time traces of average stress and strain rates from pure compression and shear calculations at 10 kHz. Converting them to frequency domain by FFT and using equations (4.2) - (4.18), we can invert the values for bulk and shear moduli, which are exactly equal to $K^{10\,\mathrm{kHz}} = 37$ GPa and $\mu^{10\,\mathrm{kHz}} = 44$ GPa for responses at such specific frequency content. In the same way, we can also estimate the bulk and shear moduli at 100 kHz, which are also equal to $K^{100\,\mathrm{kHz}} = 37$ GPa and $\mu^{100\,\mathrm{kHz}} = 44$ GPa. As we know, for an elastic solid, we expect to see no velocity dispersion, which gives rises to the same estimated values of bulk and shear moduli at 10 kHz and 100 kHz. Taking one step further, we can estimate the attenuation Q^{-1} for both P- and S-waves by equations (4.9) and (4.10), which give values of Q^{-1} on an order of 10^{-8}, small enough to be considered to be zeros that are reasonable for a pure elastic solid.

This example validates our methodology of using stress-strain calculation to obtain low-frequency responses on very tiny rock samples and provides us a meaningful way to estimate both velocity and attenuation simultaneously. In the following sections, we will use this methodology and the linear solver developed in Chapter 2 to extensively study the seismic responses of saturated porous rocks both in 2D and 3D.

4.2.3 Size effects on numerical results

People studying transportation and static elastic properties of porous rocks have found that the results depend on the total size of the imaged or digitized rocks [Schwartz et al., 1994, Auzerais et al., 1996, Arns et al., 2002]. Theoretically, the larger the size, the better the results will be. However, in reality, limited by computational resources, i.e., computational time and memory storage, we can only work on samples of small size. Therefore, a representative element volume (REV) of rocks that is large enough to cover the variability of the heterogeneity of rocks should be chosen so as to give more consistent results. For problems of dynamic responses of porous rocks, we believe the effects of the size of rocks should be as important as those in problems of transportation and static elastic properties. Therefore, it necessary for us to discuss this issue by extensively carrying out numerical study on samples with variable sizes.

For this purpose, we cut from the 3D X-ray CT images of the Berea sandstone described in Section 3.1.1 40 slices of 2D samples in size of 250×250 pixels, 20 slices in size of 500×500 pixels and 10 slices in size of 1000×1000 pixels, as shown in Figure 4-7. We only choose those slices whose porosities are within range of $19 \sim 20\%$ such that we can utilize the effective elastic properties of the digitized matrix computed in Chapter 3 where a 3D subset of the CT images with porosity of 19.2% is used. As an example, we apply velocity boundary conditions with frequency of 10 kHz along the edges of each slice, and 5 cycles are simulated. We study dry and water-saturated cases at 40 MPa, and the properties of the matrix used are listed in Table 3.4. In the dry case, we choose $V_p = 0.0$ m/s, $V_s = 0.0$ m/s and $\rho = 0.0001$ kg/m^3 for inclusion in pore space, while in the water-saturated case $V_p = 1480.0$ m/s, $V_s = 0.0$ m/s, $\rho = 1000.0$ kg/m^{3}and $\eta_\mu = 0.001\,\mathrm{Pa} \cdot \mathrm{s}$.

During the simulations, we record the time traces of average stress and strain rates, and process them as described previously to estimate the velocity and attenuation. We found that shear velocities of some slices in size of 250×250 pixels are much smaller than others. This is because the size of those 2D samples is not large enough to include enough micro-structures of rocks and thus ensure enough contacts between

grains. As an example, one of the slices is shown in Figure 4-8. We can see that parts A and B of the rock in this slice are only connected through one contact, which is unable to provide enough resistance to the shear. For similar slices whose shear velocities are much smaller, we remove them from the final results shown. In total, 6 slices, 250×250 pixels in size, having this problem are eliminated at the end.

We plot the results in terms of velocity and attenuation in Figure 4-9. From those mean values, we can see that in general velocities of water-saturated cases are larger than those of dry cases, and the same is true for attenuation, where Q^{-1} for water-saturated cases is larger than those for dry cases by at least one order of magnitude. With increasing size of samples, velocities gradually decrease, as does the variation of velocities. While for attenuation, Q^{-1} increases with size of samples, as does the variation; this trend is opposite to that of velocity. The increase of Q^{-1} that is attributed to viscous frictions between fluid and solid for water-saturated case with size can be expected since large samples have much more grain surface in absolute values.

From the Figure 4-9, we conclude that sample size has non-negligible effects on the final results in terms of velocity and attenuation. Limited by our computational resources, we choose the sample of 1000×1000 pixels in size in our study of dynamic responses of rocks in the next section.

4.2.4 Effects of viscosity on frequency-dependent responses

Depending on the viscosities of fluids and micro-structures of porous rocks, fluid mobility can contribute to the equilibrium of pore pressure within rocks differently. For example, if fluid mobility is low, even within the seismic frequency band, pore pressure might remain out of equilibrium; this can be considered in high-frequency regime. It is significant for us to understand the relationships between seismic responses and viscosity and micro-structures. To do so, we choose a 2D sample of 1000×1000 pixels in size with porosity of 19.2% as shown in Figure 4-10; this has exactly the same porosity as the 3D subset of rock described in Chapter 3. Hence, we can use the computed effective elastic moduli listed in Table 3.4 for a matrix saturated with

the corresponding fluids. We apply the stress-strain calculations - pure compression and pure shear - to such 2D sample and simulate dry and fluid-saturated cases with variable viscosities: 0.001 Pa · s, 1 Pa · s and 5 Pa · s. The frequencies studied span from 100 Hz to 10 kHz.

In Figure 4-11 we show the dispersion of P- and S-wave velocities of the 2D sample for different viscosities. We can observe significant frequency and viscosity dependence of the velocities. At a given frequency, especially for those at relatively higher frequencies, velocity increases with increasing viscosity. While for a given viscosity, especially for cases with higher viscosities, velocity significantly increase with frequency as well. These observations are mostly attributed to the contribution of viscosity to the equivalent shear modulus. The maximum dispersion of velocity for P-waves is about 1% and 5% for S-waves, which is close to the dispersion of P-waves observed on the idealized porous medium up to 1 Pa · s as shown in Figure 2-5. From Figure 4-11, we see that the dispersion curves, for both P- and S-waves, shift to lower frequency with increasing viscosity; this indicates that the characteristic frequency (f_c), if there is one for such 2D complex rock, is proportional to the inverse of viscosity, $f_c \sim \eta_\mu^{-1}$. In fact, increasing the viscosity decreases the fluid mobility, which pushes the dispersion, which usually happens at high frequency, to low frequency where pressure in fluid can have enough time to reach equilibrium.

As may be observed in such 2D cases, the velocities for both P- and S-waves computed are much smaller than those predicted from the 3D rock introduced in the previous chapter, since the micro-structures of the 3D rocks cannot be replaced by 2D slices even though plane strain is assumed. The weaker shear rigidity of the 2D samples causes most problems. Limited by the computing resources, we can only carry out the numerical simulations on a 2D sample of reasonable size, i.e. 1000×1000 pixels, to frequencies as low as 100 Hz. For example, the total time step the simulation takes for case with $\eta_\mu = 5\,\text{Pa} \cdot \text{s}$ at 100 Hz is about 100 million per cycle, which takes at least 7 days even though the code has been parallelized.

In Figure 4-12 the dispersion curves of attenuations (Q^{-1}) for both P- and S-waves are shown for different saturations at different frequencies. In fluid-saturated cases,

Q_P^{-1} and Q_S^{-1} generally increase with frequency, but we can see the effects of viscosity of fluid on attenuation. For cases with $\eta_\mu = 0.001\,\mathrm{Pa}\cdot\mathrm{s}$, Q^{-1} is at least 1 or 2 orders of magnitude larger than that of dry cases whether for P- or S-waves. With increase of viscosity, the viscous effect become dominant since the equivalent shear modulus due to the viscosity of fluid in fact lowers the degree of heterogeneity present in such 2D porous rock. In general, Q_S^{-1} is larger than Q_P^{-1} from the computed results; this demonstrates the same trend observed in laboratory measurements [Johnston and Toksöz, 1980]. With increasing viscosity, the attenuations for fluid-saturated cases increase as well. The shift of the attenuation curves to lower frequency with increasing viscosities agrees with the relationships established in mathematical models between velocity dispersion and attenuation, where the shift of the peak of the attenuation curve in frequency should corresponds to the shift of transition part of velocity in frequency.

As we have discussed previously, since we use a 2D sample rather than a 3D sample the computed dispersions of velocity and attenuation cannot be compared to data measured in laboratories. However, we are more interested in demonstrating the dependence of the dispersions of velocity and attenuation on frequency, inclusions and fluid viscosity through such numerical simulations on digitized rocks by capturing the micro-structures of rocks and interactions between fluid and solid explicitly. We indeed observe such dependence and conclude that fluid mobility is the dominant factor to the frequency responses of seismic waves; this agrees with laboratory observations [Batzle et al., 2006].

4.3 Seismic Responses of 3D Digitized Rock

4.3.1 Frequency-dependent velocity and attenuation in 3D

In the 3D case, instead of assuming a plane strain condition, we can directly estimate the bulk modulus $K^{3D}(\omega)$ by

$$K^{3D}(\omega) = \frac{1}{3}\left(\frac{\dot{\sigma}_{xx} + \dot{\sigma}_{yy} + \dot{\sigma}_{zz}}{\dot{\varepsilon}_{xx} + \dot{\varepsilon}_{yy} + \dot{\varepsilon}_{zz}}\right) \tag{4.15}$$

in which a pure compression calculation is applied along six surfaces of the 3D cubic subset as shown in Figure 4-13a.

While the total average shear modulus $\mu^{3D}(\omega)$ is estimated from shear moduli $\mu_{xy}^{3D}(\omega)$, $\mu_{yz}^{3D}(\omega)$ and $\mu_{xz}^{3D}(\omega)$ that are measured independently along three directions as shown in Figures 4-13b to 4-13d. The relationship between these moduli is

$$\mu^{3D}(\omega) = \frac{1}{3}\left(\mu_{xy}^{3D}(\omega) + \mu_{yz}^{3D}(\omega) + \mu_{xz}^{3D}(\omega)\right) \tag{4.16}$$

and the three shear moduli are obtained from

$$\mu_{xy}^{3D}(\omega) = \frac{1}{2}\frac{\dot{\sigma}_{xy}}{\dot{\varepsilon}_{xy}} \tag{4.17}$$

$$\mu_{yz}^{3D}(\omega) = \frac{1}{2}\frac{\dot{\sigma}_{yz}}{\dot{\varepsilon}_{yz}} \tag{4.18}$$

$$\mu_{xz}^{3D}(\omega) = \frac{1}{2}\frac{\dot{\sigma}_{xz}}{\dot{\varepsilon}_{xz}} \tag{4.19}$$

Once we have obtained the frequency-dependent elastic moduli for a 3D sample, we can still use equations (4.5) to (4.10) to estimate the corresponding frequency-dependent velocities and attenuations for P- and S-waves.

4.3.2 Stress-strain calculation in 3D

We can measure the dynamic responses of a 3D sample by carrying out these four stress-strain calculations: one pure compression and three pure shear calculations as shown in Figure 4-13. Prescribed velocity boundary conditions are applied on the surfaces of the 3D cube, accordingly, to which a sinusoidal wave is employed. Single frequency content is simulated separately for each case so as to raise the signal-to-noise ratio in results. During the simulation, we collect the fields of average stress and strain rate in the whole domain as well by equations (4.11) and (4.12), and convert them into frequency domain with equations (4.13) and (4.14).

To benchmark the methodology of measuring average elastic moduli of 3D rocks developed above, we compare the results computed for dry and water-saturated cases on a 3D cubic subset of the digitized Berea sandstone with finite-difference method (FDM) to those computed from finite-element method (FEM) from NIST. We use the same 3D sample described in Chapter 3. According to Table 3.4, we choose the properties of matrix for dry case: $K_{\mathrm{m}}^{\mathrm{dry}} = 24.1$ GPa, $\mu_{\mathrm{m}}^{\mathrm{dry}} = 30.3$ GPa and $\rho_{\mathrm{m}}^{\mathrm{dry}} = 2527.2$ kg/m^3, and water-saturated case: $K_{\mathrm{m}}^{\mathrm{water}} = 28.6$ GPa, $\mu_{\mathrm{m}}^{\mathrm{water}} = 31.6$ GPa and $\rho_{\mathrm{m}}^{\mathrm{dry}} = 2573.5$ kg/m^3, which has already taken cracks inverted into account. The inclusions for dry case are: $K = 0.0$ GPa, $\mu = 0.0$ GPa and $\rho = 0.0001$ kg/m^3, and for water-saturated case are: $K = 2.2$ GPa, $\mu = 0.0$ GPa and $\rho = 1000$ kg/m^3. Note that FEM measures the static responses while FDM measures the dynamic responses. In the modeling with FDM, we use a sinusoidal wave at 100 kHz as the boundary conditions. In Table 4.1, we show the comparison of the effective elastic properties estimated by the finite-element method and the stress-strain calculation with the finite-difference method. We can see that the numerical results computed from these two methods are quite close; this validates our methodology developed. Also we can conclude from the comparison that there is almost no obvious dispersion between velocities at 0 Hz computed by FEM and those at 100 kHz by FDM. We will utilize this stress-strain calculation in the following study for 3D cases.

4.3.3 Laboratory measurements on Berea sandstones

Berea sandstones have been used in laboratory study for a long time and the measured dispersion and attenuation data can be found in many published papers. Johnston and Toksöz [1980] used the transmission technique to measure attenuation for dry and water-saturated Berea sandstones. Assuming a constant Q model, the spectrum of signals within the frequency band of 300 kHz - 600 kHz was fitted so as to estimate the attenuations for P- and S-waves. Winkler [1983, 1985] utilized the pulse echo technique to measure attenuation for P-wave of Berea sandstones saturated with brine. The frequency range considered was 400 kHz and above. Winkler and Nur [1982], Jones and Nur [1983], Murphy et al. [1986] used the resonant bar technique to measure the attenuation of Berea sandstones for water-saturated case at frequencies around 1700 - 3400 Hz. Most recently, Best and Mccann [1995] measured the velocities and attenuations for both P- and S-waves on several similar Berea sandstones for dry and fluid-saturated cases with different viscosities. The physical properties of the Berea sandstones Best and Mccann [1995] used are listed in Table 4.2. In the laboratory experiments, they measured the velocities and attenuations with the pulse echo technique with source at 0.8 MHz for samples under 50 MPa effective pressure, which simulated the in-situ conditions. The physical properties of those fluids are listed Table 4.3, and the measured velocities and attenuations are listed in Table 4.4.

The digitized Berea sandstone used in our study, as described in Chapter 3, has porosity $\sim$ 23.5%, clay content $\sim$ 3.5% and permeability $\sim$ 500 mD, which are similar to those which Best and Mccann [1995] used in their laboratory experiments. Therefore, we can use the data measured by Best and Mccann [1995] as the laboratory measurements to numerically study the viscosity dependent velocity and attenuation with our digitized 3D Berea sandstone.

4.3.4 Viscosity dependence of velocity and attenuation

4.3.4.1 Total attenuation

As pointed out by Toksöz and Johnston [1981], the total attenuation of rocks can be attributed to at least three mechanisms: friction, viscous fluid and scattering as described by expression

$$\frac{1}{Q_{\text{Tot}}} = \frac{1}{Q_{\text{Fri}}} + \frac{1}{Q_{\text{Vis}}} + \frac{1}{Q_{\text{Sca}}} \tag{4.20}$$

where $\frac{1}{Q_{\text{Tot}}}$ is the total attenuation, $\frac{1}{Q_{\text{Fri}}}, \frac{1}{Q_{\text{Vis}}}, \frac{1}{Q_{\text{Sca}}}$ are attenuations due to friction, viscous fluid and scattering, respectively.

Friction usually occurs along cracks or grain contacts both in dry and fluid-saturated cases. It can be described with Coulomb friction and convert seismic energy into heat. Researchers have studied this type of attenuation both mathematically and experimentally [e.g., Walsh, 1965, O'Connell and Budiansky, 1977, Winkler et al., 1979], and concluded that the attenuation due to friction for the dry case is almost constant with frequency, and Q_P^{-1} and Q_S^{-1} are almost the same order of magnitude. In the fluid-saturated case, the friction coefficient between two planes of cracks or grain contacts decreases due to the lubrication effect of fluid so as to increase relative motion between the planes; this can cause higher attenuation due to the friction. Under the vibrations of seismic waves on a rock frame, the fluid saturated in pore space can be driven to flow; this causes attenuation due to the viscous effect of fluid. Usually in rocks, the total pore space is composed of big pores and small cracks. When a wave propagates through rocks, big pores are stiff and hard to deform, while cracks are compliant and easy to deform. Because of the co-existence of stiff and compliant pores in rocks, attenuation due to viscous fluid can be attributed to the Biot type in big pore and the squirt-flow type in cracks. Scattering only comes into play significantly when the frequency reaches the height where the equivalent wavelength of the wave is on the same order of the sizes of pore space or grains. By taking into account the stiff and compliant pores, we can rewrite equation (4.20) as

$$\frac{1}{Q_{\text{Tot}}} = \frac{1}{Q_{\text{Fri}}} + \frac{1}{Q^{\text{s}}_{\text{Vis}}} + \frac{1}{Q^{\text{c}}_{\text{Vis}}} + \frac{1}{Q_{\text{Sca}}} \tag{4.21}$$

where the attenuation due to viscous fluid can be divided into two parts: $\frac{1}{Q^{\text{s}}_{\text{Vis}}}$ due to stiff pores and $\frac{1}{Q^{\text{c}}_{\text{Vis}}}$ due to compliant pores.

In our numerical study, since our solver does not include the physics of friction but only the viscous fluid effect, we are unable to capture the attenuation, $\frac{1}{Q_{\text{Fri}}}$, due to friction loss. Furthermore, as we discussed in Chapter 3, due to the loss of small cracks in the low resolution digitized data, the viscous effect of fluid in small cracks — the squirt-flow effect — cannot be captured as well. Therefore, for the digitized 3D Berea sandstone, only the effects of viscous fluid in big pores and scattering can be simulated by our numerical solver.

4.3.4.2 The modified squirt-flow model

As discussed earlier, the loss of small cracks in the imaging process has significant impact both on the computations of velocity and attenuation. In Chapter 3, we have used the Kuster-Toksöz model to include the lost cracks in the matrix of digitized rocks. As for attenuation, we also need to find another mathematical model to compensate for the contribution of small cracks to the total attenuation through the squirt-flow mechanism.

For this purpose, we choose a new model of squirt-flow dispersion and attenuation developed by Gurevich et al. [2009c], which combines the pressure relaxation approach of Murphy et al. [1986] with the extension of equations of Mavko and Jizba [1991] to arbitrary fluid. The resulting model is consistent with the Gassmann and Mavko-Jizba models at low and high frequencies, respectively. In order to cover a broad band of frequencies, this model can be incorporated into Biot's model to obtain velocity and attenuation at corresponding frequencies. We describe the details of the new model of squirt-flow in Appendix E.

4.3.4.3 Crack inversion

To compute the velocity and attenuation that vary with viscosity of fluid with the 3D digitized Berea sandstone, we first need to invert the distribution of cracks lost during the imaging process as we did in Chapter 3. Instead of only using velocities of P- and S-waves measured for dry and water-saturated cases, we can further take advantage of the attenuation data measured in the laboratory so as to further constrain the inversion for crack distribution.

Since we use the data measured at 50 MPa on Berea sandstones with 7.4% clay content [Best and Mccann, 1995], in the inversion we first have to take clay into account by using the Voigt-Reuss-Hill (VRH) average to compute the averaged elastic properties of the matrix [Mavko et al., 1998], in which we assume quartz and clay are mixed homogeneously. Taking the values of the properties for quartz: $K_{\text{quartz}} = 37.0$ GPa, $\mu_{\text{quartz}} = 44.0$ GPa and $\rho_{\text{quartz}} = 2650$ kg/m^3, and for clay: $K_{\text{clay}} = 25.0$ GPa, $\mu_{\text{clay}} = 9.0$ GPa and $\rho_{\text{clay}} = 2550$ kg/m^3, we obtain the elastic bounds for the mixture of the matrix, where $K \in [35.8, 36.2]$ GPa and $\mu \in [34.6, 41.6]$ GPa. In the VRH average, we usually take the average between the upper and lower bounds as the final results. However, we find that this works for the bulk modulus because the upper and lower bounds of K are so close that the averaged bulk modulus is tightly restricted in a narrow range. Therefore, we take $\overline{K} = 36.0$ GPa. As for shear modulus, we notice that it spans a wide range of values between [34.6, 41.6] GPa. We believe that the elastic properties of clay will be quite different in dry and water-saturated cases, especially for shear modulus. Being filled with water, the shear modulus of clay should decrease. Therefore, we chose $\overline{\mu} = 37.5$ GPa for the dry case, and $\overline{\mu} = 36.0$ GPa for the water-saturated case as the shear moduli for the mixture of matrix. Secondly, in the experiments at 50 MPa, most of the small cracks within and between grains should be closed under such high pressure and cracks with large aspect ratio could be left open. Therefore, in the inversion, we keep cracks with large aspect ratio ($\alpha \sim 10^{-1}$) in the initial guess for the binary structure of crack distribution [Shapiro, 2003].

Following the procedure of Monte-Carlo inversion described in Chapter 3, we can invert the crack distribution for the first round only with the measured velocities of P- and S-waves for dry and water-saturated cases. Using the best results inverted after this round, with the Kuster-Toksöz model or numerical computation we can compute the effective elastic moduli for the dry frame with cracks included: K_{dry} and μ_{dry}. Nonetheless, we have already computed the elastic moduli for the dry frame of rocks containing only stiff pores resolved in the imaging process with no cracks, so we can take them as K_h and μ_h for dry frame bulk and shear moduli of the hypothetical rocks, respectively. We can further refine the inverted cracks within a small range so as to fit only the measured attenuation data of P-waves by using the modified squirt-flow model introduced in Appendix E.

In fact, we find that depending on the initial guess of cracks in the first round inversion, in most cases we are able to end up with a best solution to crack distribution that can fit the measured velocities of P- and S-waves for both dry and water-saturated cases well. However, not all the best solutions obtained in the first round can fit the attenuation data of P-waves. Actually it is critical to include the cracks with large aspect ratio ($\alpha \sim 10^{-1}$) in order to do so. We think two reasons can physically justify the need to include cracks with large aspect ratio. First, cracks with high aspect ratios have the chance to be left open under high pressure. Second, in the squirt-flow mechanism, cracks with small aspect ratios and small porosities, in fact, push the attenuation peak to low frequencies. In order to gain enough attenuations at frequency as high as 0.8 MHz used in experiment, cracks with large aspect ratio are needed. After two rounds of inversion, we obtain the best set of cracks listed in Table 4.5.

4.3.4.4 Computations of velocity and attenuation

In the previous section we mentioned briefly the use of the modified squirt-flow model to estimate the attenuation data of P-waves during inversion. In this section, we will expand this topic and introduce the hybrid method by combining numerical computation with theoretical models so as to compute the velocity and attenuation

with the 3D digitized Berea sandstone.

As discussed before, the loss of small cracks during the imaging process not only has impact on the computation of velocity but also attenuation. By including cracks into the continuous matrix used in numerical computation, we can resolve the issue of velocity computation as describe in Chapter 3. However, as for the attenuation, we have to consider that the total attenuation due to viscous fluid effect consists of two parts: $\frac{1}{Q^{s}_{\mathrm{Vis}}}$ due to stiff pores and $\frac{1}{Q^{c}_{\mathrm{Vis}}}$ due to compliant pores. In our numerical computation, actually we are only able to capture the viscous effects of fluids in stiff pores resolved in the imaging process, $\frac{1}{Q^{s}_{\mathrm{Vis}}}$, but miss the other part attributed to small cracks that affect not only the elastic properties of rocks but also the attenuation. In order to compensate for the missing part of attenuation, $\frac{1}{Q^{c}_{\mathrm{Vis}}}$, we use the modified squirt-flow model with the help of the inverted crack distribution.

By the stress-strain calculation, we can easily compute the attenuations for both P- and S-waves at 0.8 MHz for the different fluids listed in Table 4.3. After gaining all the necessary parameters needed in the modified squirt-flow model, we can also compute the velocities and attenuations for both P- and S-waves at the same frequency for the same fluids. Besides the attenuation due to viscous fluid effect, the friction loss should be included into the total attenuation as well. One simple way to estimate the friction loss is to use the attenuations measured for dry case. However, we believe that the friction loss in fluid-saturated cases should be slightly larger than that in dry case due to the lubrication effect of fluid on planes of cracks. Therefore, the values for attenuations due to friction for both P- and S-waves should be somewhere between attenuations for dry and water-saturated case. We choose $\frac{1}{Q^{P}_{Fri}} = 0.00625$ for P-wave and $\frac{1}{Q^{S}_{Fri}} = 0.02$ for S-wave, respectively.

From the large 3D digitized Berea sandstone with size of $1840 \times 1840 \times 1940$ pixels, we cut a 500^3 pixels cubic subset as shown in Figure 4-14 for the numerical study. This subset has porosity $\sim 20.5\%$, which is close to the samples used by Best and Mccann [1995]. After the crack inversion and numerical computations, we obtain the numerically computed velocities for both P- and S-waves as shown in Figure 4-15, which match the laboratory measurements well. With the modified squirt-flow

model and necessary parameters, we can also estimate the velocities for different fluids theoretically. As shown in Figure 4-16, the theoretically estimated velocities also match the laboratory measurements well. The consistency between the numerically computed and theoretically estimated velocities indicates that (1) the capability of the modified squirt-flow model when hybridized with numerical computation for velocity prediction; (2) the uniqueness of the inversion results for crack distribution should be in high confident level. Furthermore, in Figure 4-17 we show the increase of the bulk and shear moduli of the partially relaxed frame computed from the modified squirt-flow model. The increase of bulk moduli with viscosities of fluids is attributed partially to the increase of the bulk moduli of saturating fluids. However, the increase of the shear moduli is attributed totally to the effects of viscosities of fluids, which is consistent with laboratory observations where increase of dynamic shear modulus is caused by the squirt-flow of viscous fluid in clay [Han, 1986, Khazanehdari and Sothcott, 2003].

In Figure 4-18 we show the attenuations due to the viscous fluid effect and to the friction loss. By saturating the stiff pores of the 500^3 pixels cubic subset of the digitized Berea sandstone with the corresponding fluids in numerical simulations, we can compute the attenuations due to viscous fluid in stiff pores $\frac{1}{Q^s_{\text{Vis}}}$ as shown in Figure 4-18a. With the modified squirt-flow model and necessary parameters, we can predict the attenuations due to viscous fluid in compliant pores as shown in Figure 4-18b. Finally, by adding the attenuations estimated for friction loss, as shown in Figure 4-18c, we can obtain the total attenuations of both P- and S-waves for different fluids as shown in Figure 4-19. These attenuation values match the laboratory measurements as do the velocity data. At frequency of 0.8 MHz, the shortest wavelength of the S-waves is ~ 2 mm, which is still much longer than the heterogeneities due to grains and pore space in the Berea sandstone. Therefore, the attenuation due to scattering is ignored at current study.

By hybridizing the numerical computation with theoretical model and taking into account the cracks lost in the imaging process, we have successfully predicted the velocities and attenuations for a 3D digitized Berea sandstone. Predicted values

match the laboratory data quite well. In this work, we only use the measured velocities of P- and S-waves for dry and water-saturated cases and attenuations of P-waves for different fluids to carry out the inversion for crack distribution. Based on the inverted cracks, we demonstrate the capability of the hybrid method on predicting velocities of P- and S-waves and attenuations of S-waves for cases saturated with other types of fluids. This study also shows the importance of the squirt-flow mechanism on controlling the velocity dispersion and attenuation of porous rocks under saturation.

Table 4.1: Comparison for results of the effective elastic properties estimated by the finite-element method from NIST and the stress-strain calculation with finite-difference method for a 3D cubic subset of the digitized Berea sandstone.

		$\langle K \rangle$ (GPa)	$\langle \mu \rangle$ (GPa)
FEM	Dry	13.6	13.9
	Water	17.8	14.9
FDM	Dry	13.5	14.1
	Water	17.7	15.0

Table 4.2: Physical properties of the Berea sandstones used by Best and Mccann [1995].

Porosity (%)	20.5
Permeability (mD)	519.0
Clay content (%)	7.4
Clay/porosity ratio	0.361
Grain size (μm)	180
Pore diameter (μm)	28.1

Table 4.3: The physical properties of fluids [Best and Mccann, 1995].

Fluid	Viscosity ($Pa \cdot s$)	Density (kg/m^3)	Velocity (m/s)	Bulk Modulus (GPa)
Water	0.001	1000	1483	2.2
Solution 3	0.023	1177	1763	3.658
Solution 4	0.074	1210	1811	3.968
Solution 2	0.456	1242	1868	4.333
Solution 1	0.943	1249	1880	4.414

Table 4.4: Experimental measurements of velocities and attenuations for both P- and S-waves for dry and fluid-saturated cases on Berea sandstones at 0.8 MHz and 50 MPa [Best and Mccann, 1995].

	Dry	Water	Solution 3	Solution 4	Solution 2	Solution 1
Viscosity ($Pa \cdot s$)		0.001	0.02	0.067	0.311	0.765
Vp (m/s)	3935	3913	3964	4064	4111	4074
Vs (m/s)	2571	2394	2331	2444	2445	2438
Q_P	$>$200	133$\pm$62	179$\pm$128	24$\pm$1	33$\pm$3	30$\pm$2
Q_S	109	32$\pm$1	23$\pm$1	27$\pm$1	21$\pm$1	23$\pm$1

Table 4.5: The best set of cracks from Monte-Carlo inversion at 50 MPa.

Aspect Ratio (α)	$[1.07 \times 10^{-1}, 7.94 \times 10^{-2}, 7.73 \times 10^{-3}, 8.36 \times 10^{-4}]$
Concentration (c)	$[3.94 \times 10^{-2}, 1.43 \times 10^{-3}, 3.00 \times 10^{-7}, 4.50 \times 10^{-6}]$

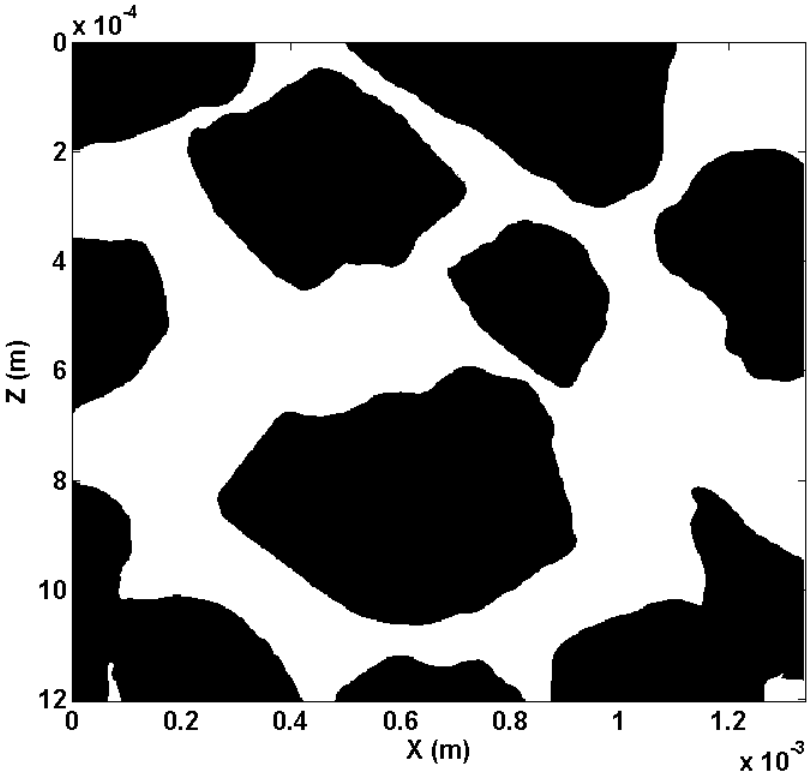

Figure 4-1: A segmented 2D image of a quartz sand sample (San Gregorio, CA). The quartz grains are shown in black. In our simulations, the grains are assumed to be suspended in water.

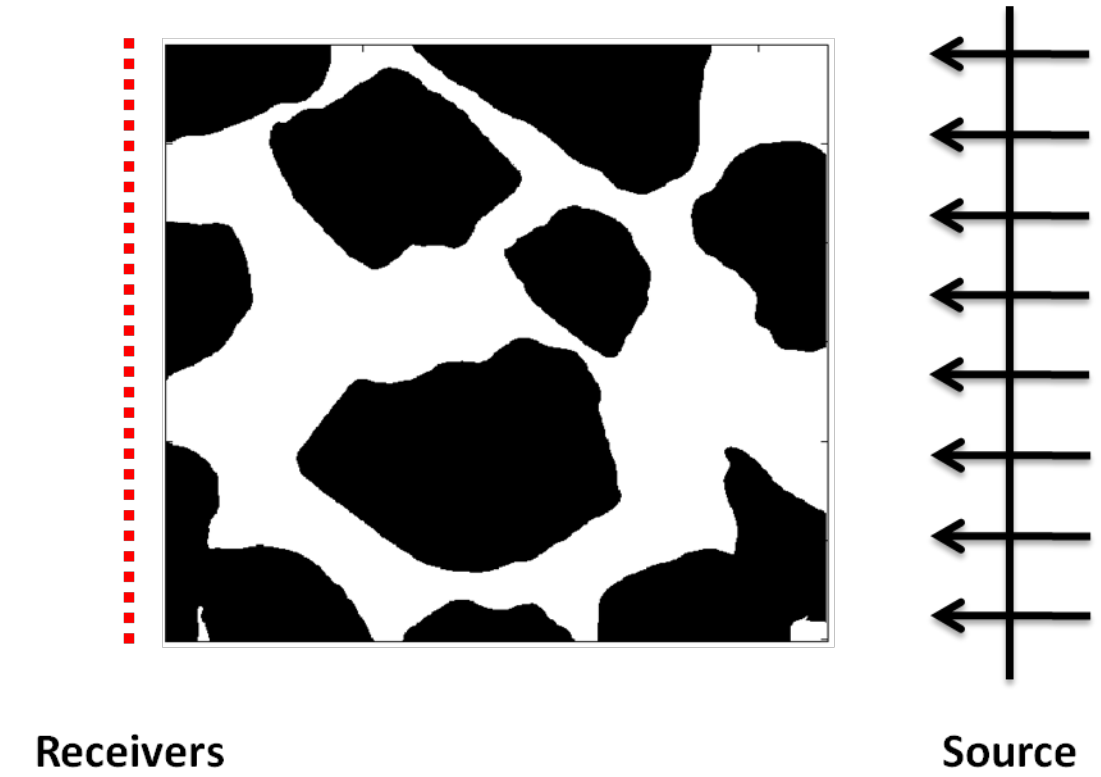

Figure 4-2: The geometry of our numerical experiment in 2D. A compressional plane wave propagates through the sample from the right. One array of receivers (red dotted line) samples the transmitted wave.

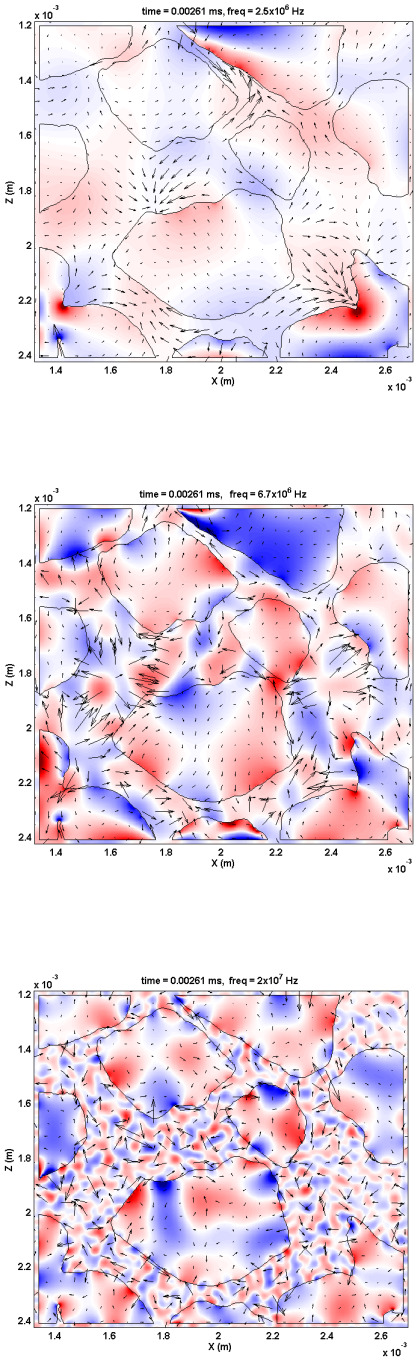

Figure 4-3: Snapshots for pressure and velocity fields of three cases in which sources are at different frequencies — 2.5 MHz, 6.7 MHz and 20 MHz, respectively. Colorful background shows the magnitude of pressure field: blue represents extension and red represents compression. Arrows show the magnitude of the velocity of the particle motion on microscale.

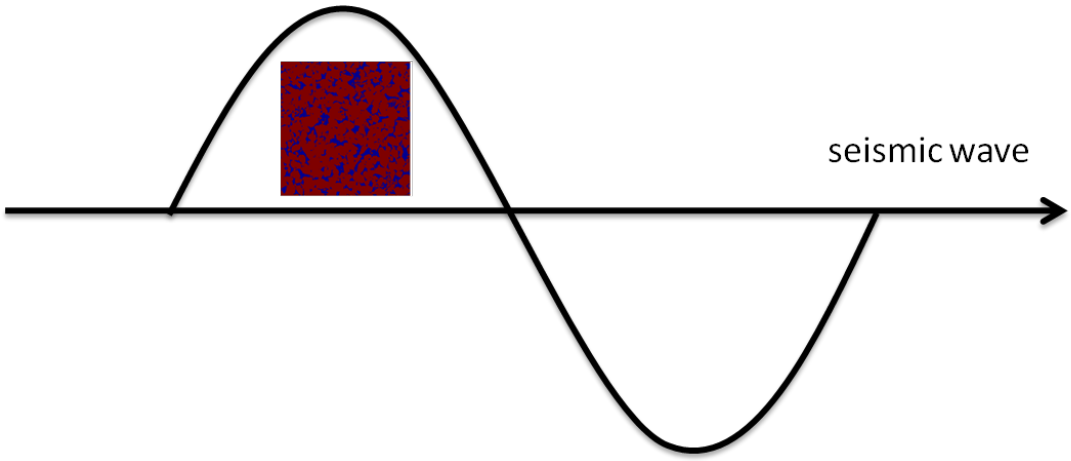

Figure 4-4: Seismic wave propagates through a small chunk of rock. The size of the rock is usually many orders of magnitude smaller than the wavelength of seismic wave investigated.

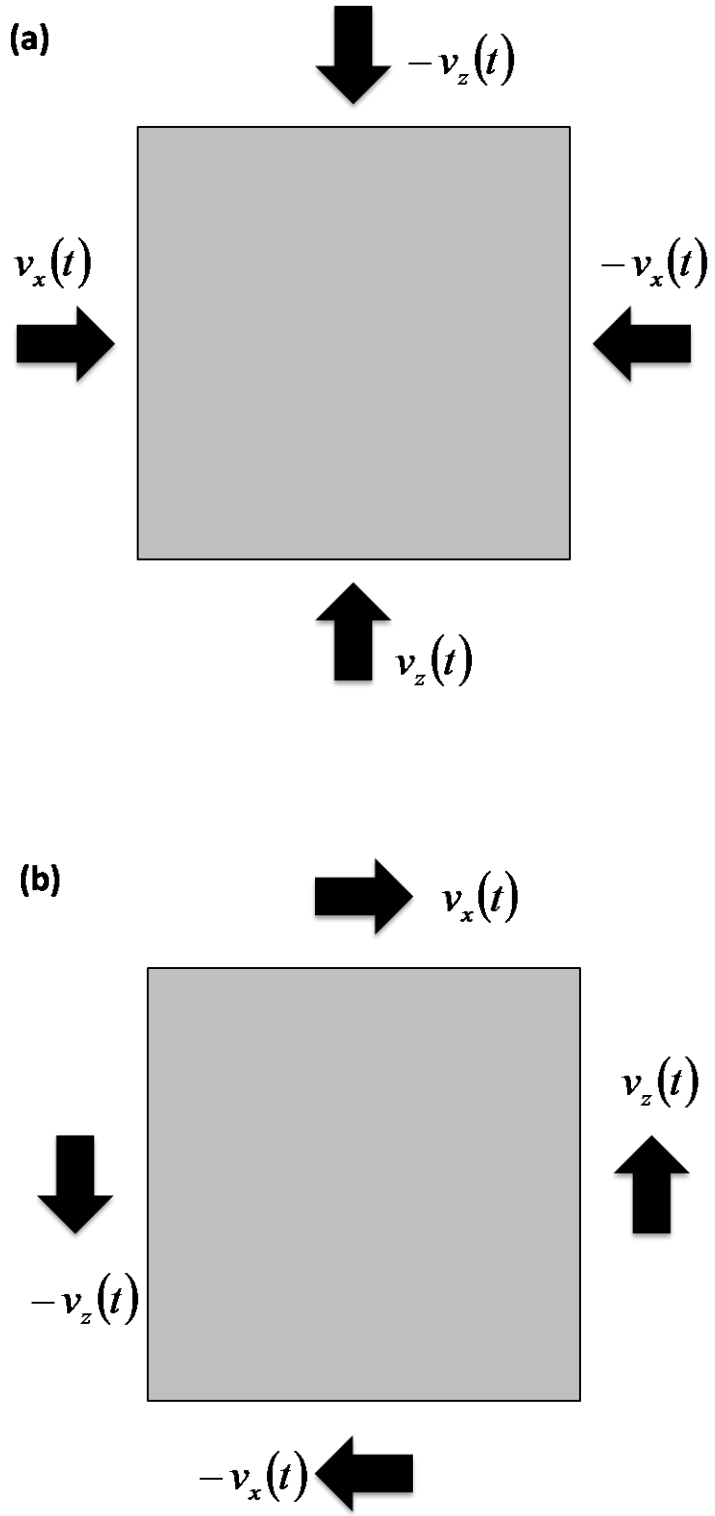

Figure 4-5: Stress-strain calculations on a 2D sample. (a) pure compression calculation; (b) pure shear calculation.

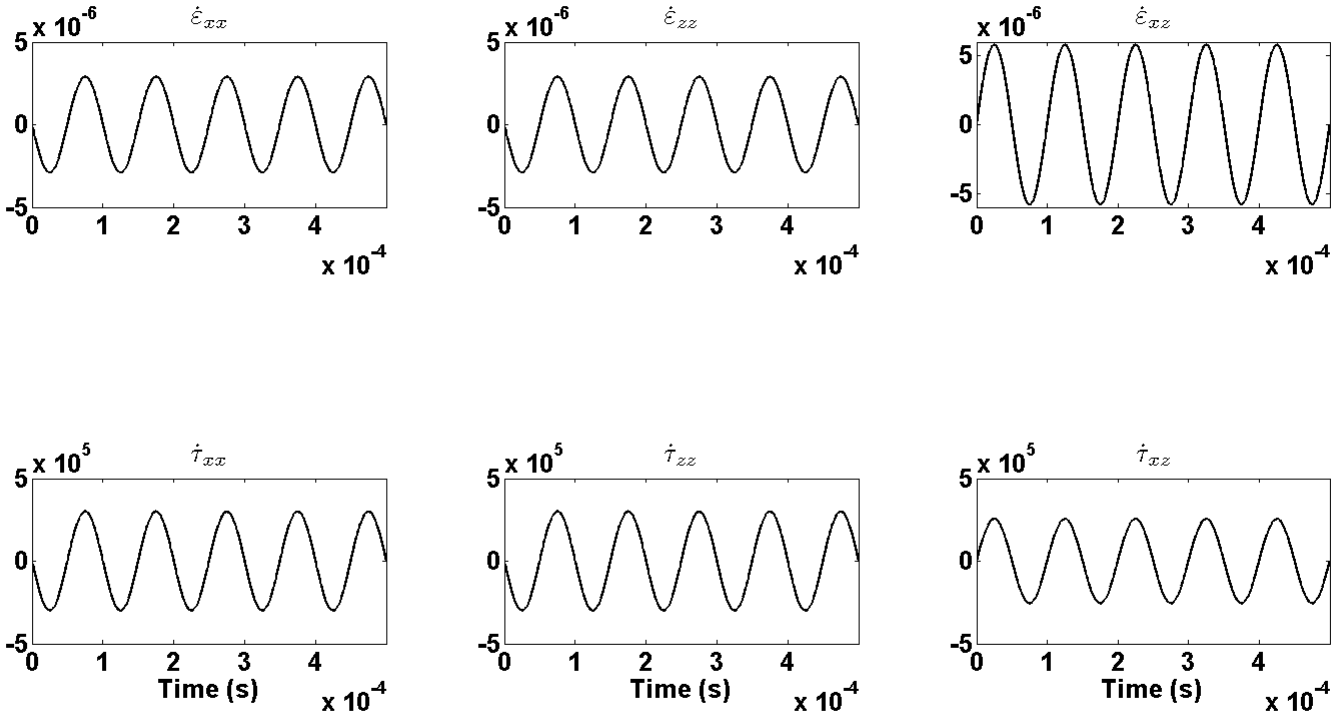

Figure 4-6: Time traces of average stress and strain rates from pure compression and shear calculations for an 2D elastic solid sample at 10 kHz.

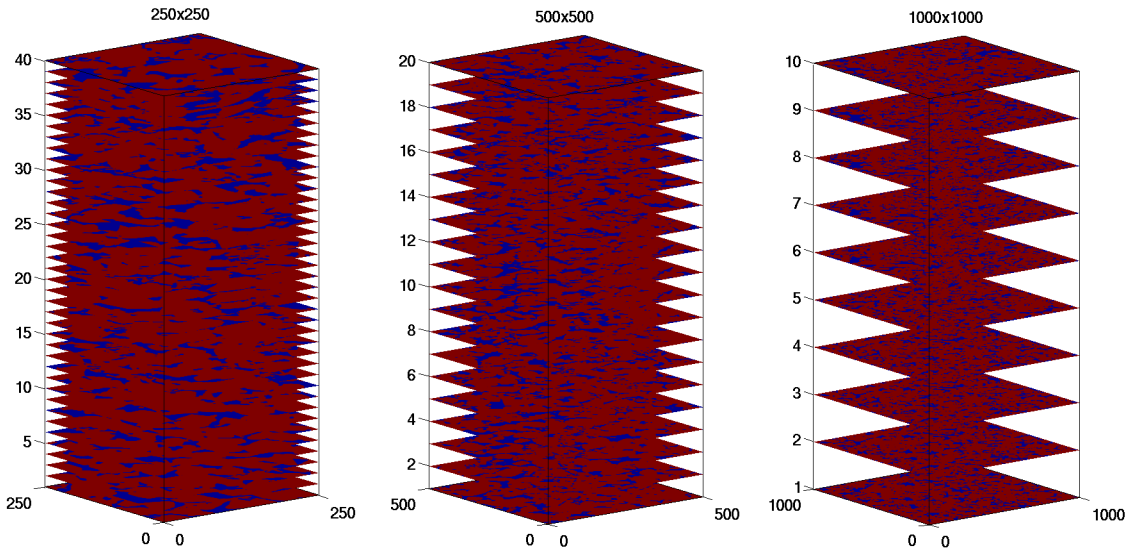

Figure 4-7: 2D slices cut from 3D X-ray CT images in variable sizes.

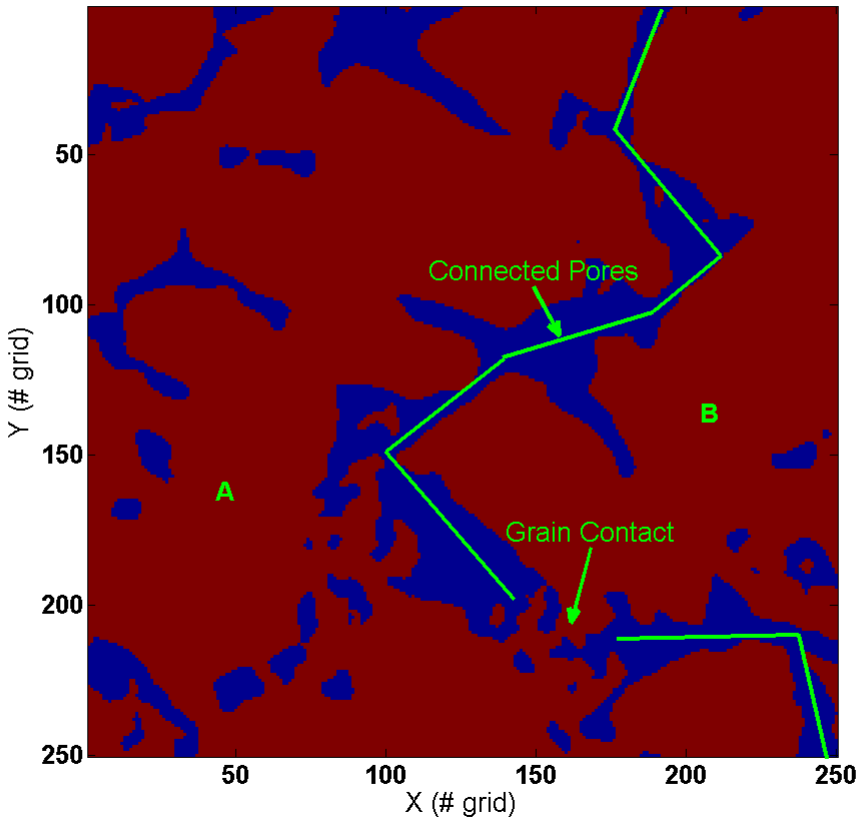

Figure 4-8: A 2D slice in size of 250×250 whose shear velocity is much lower than others. The connected pore spaces are marked with green lines, and the only grain contact linking part A and B is indicated by green arrow.

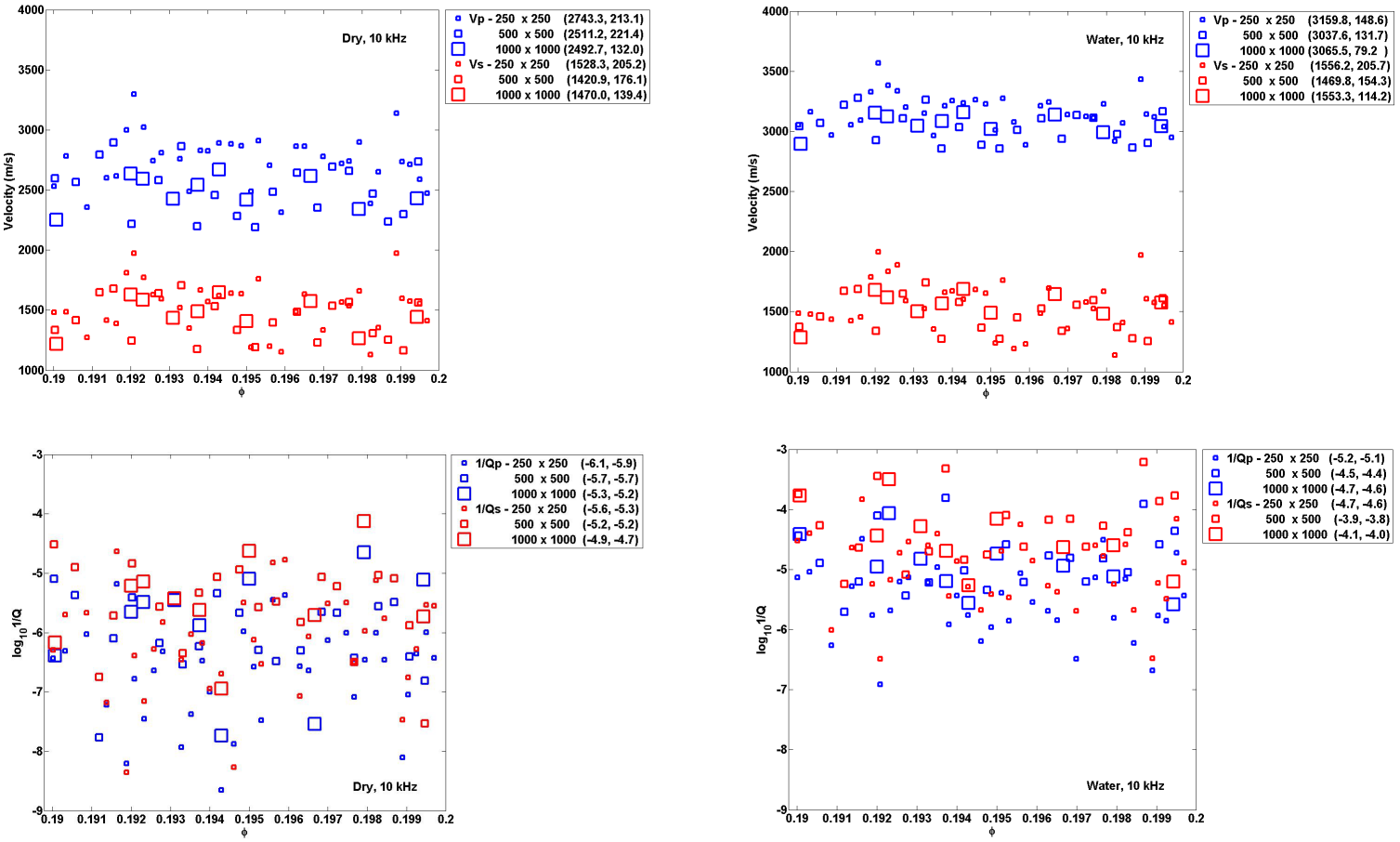

Figure 4-9: Velocities and attenuations of dry and water-saturated cases for variable sizes of 2D slices. Velocity boundary conditions at 10 kHz are applied along edges of each slice. Inside each parenthesis in every legend, the first value is the mean velocity, and the second value is the standard deviation.

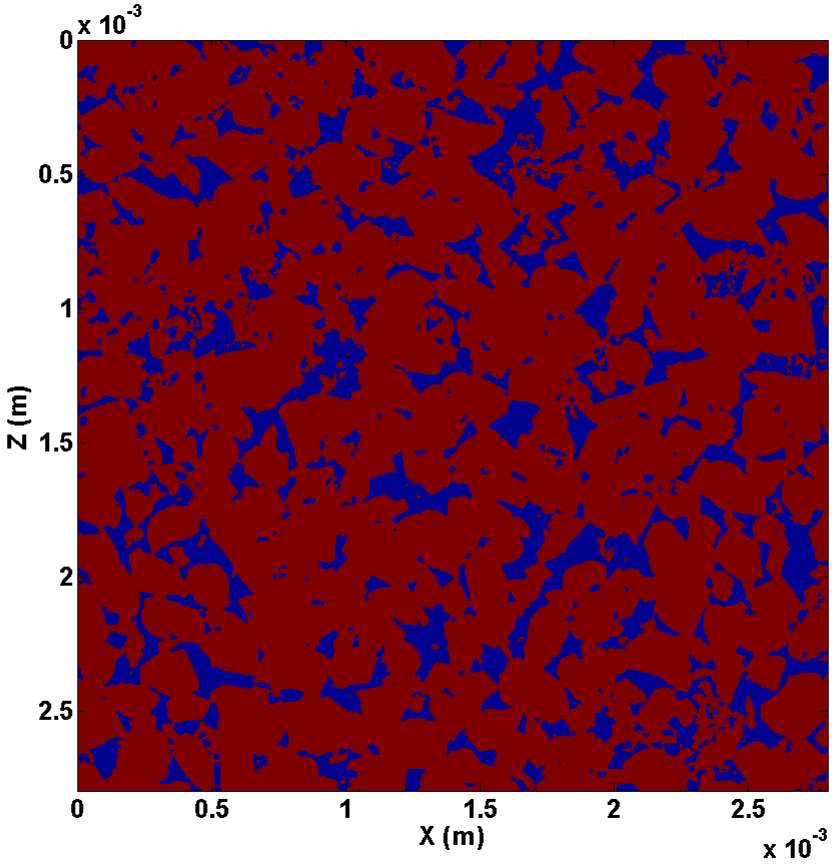

Figure 4-10: 2D sample in size of 1000×1000 with porosity of 19.2%.

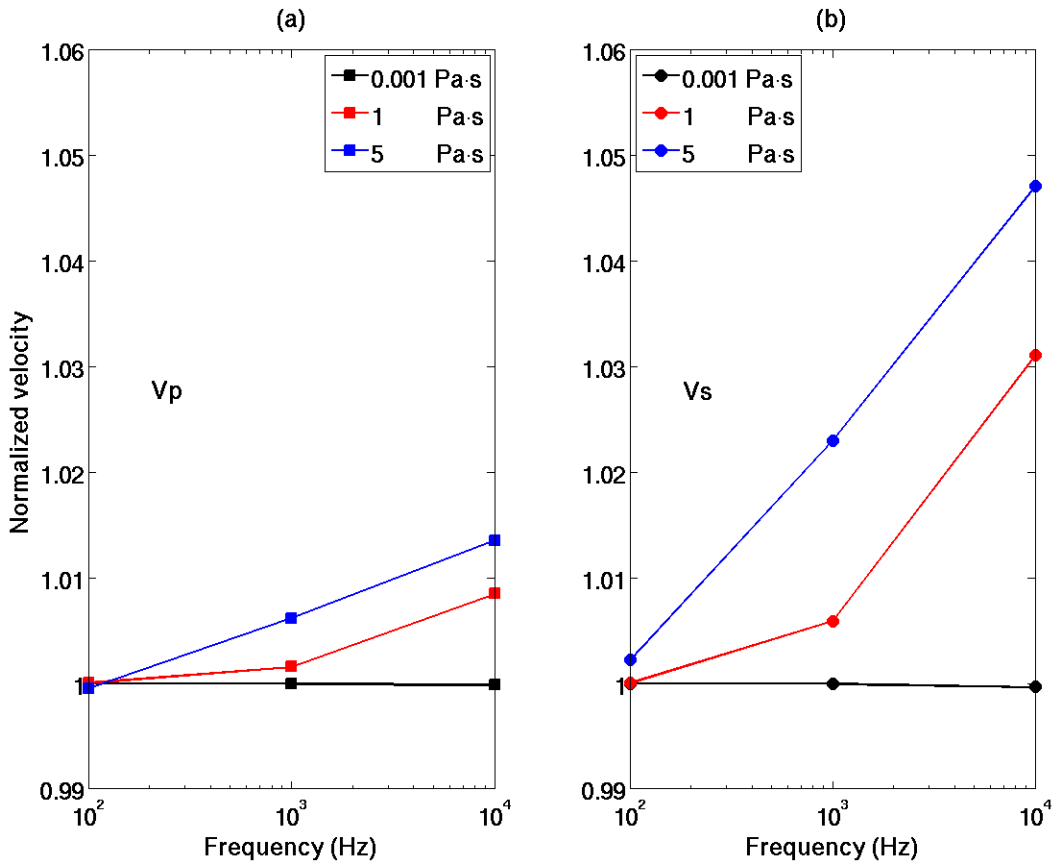

Figure 4-11: Velocity dispersions for P- and S-waves of a 2D digitized Berea sandstone with frequency and viscosity. (a) P-wave velocity (square); (b) S-wave velocity (circle). Frequency varies from 100 Hz to 10 kHz.

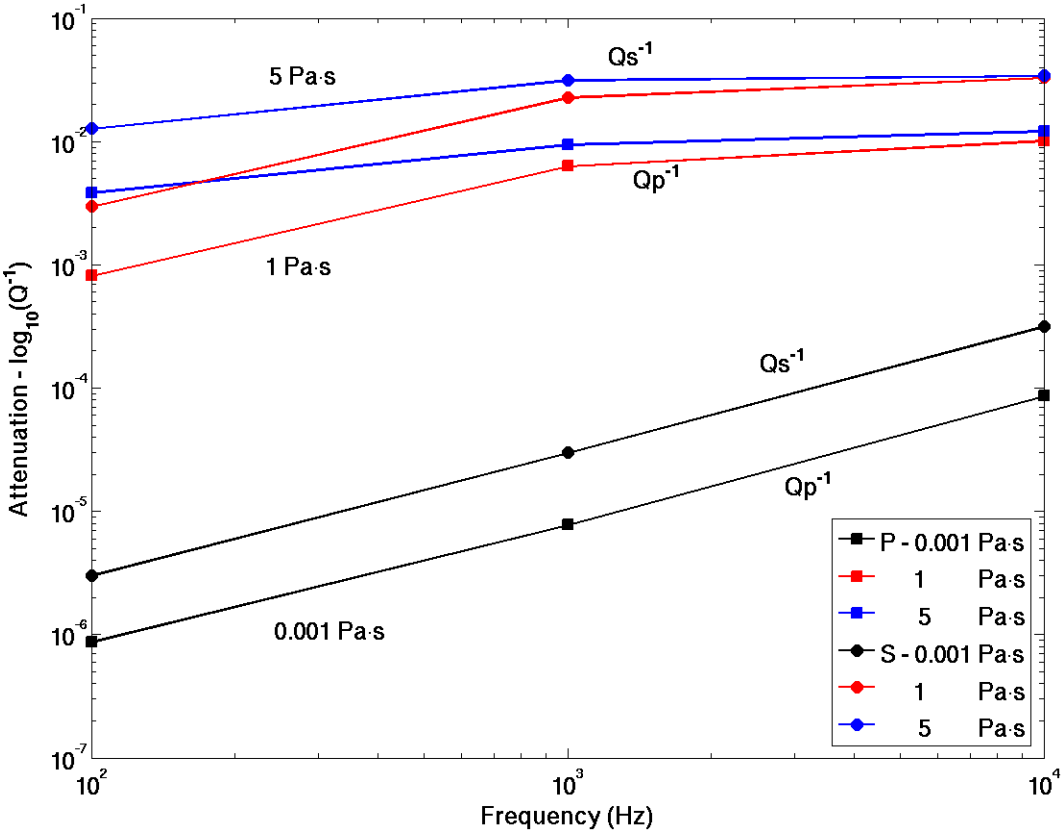

Figure 4-12: Attenuation for P- and S-waves of a 2D digitized Berea sandstone with frequency and viscosity (Q_P^{-1}: square; Q_S^{-1}: circle) . Frequency varies from 100 Hz to 10 kHz. The black, red and blue curves represent computed attenuations for saturating fluids with viscosities of 0.001, 1 and 5 Pa $\cdot$ s, respectively.

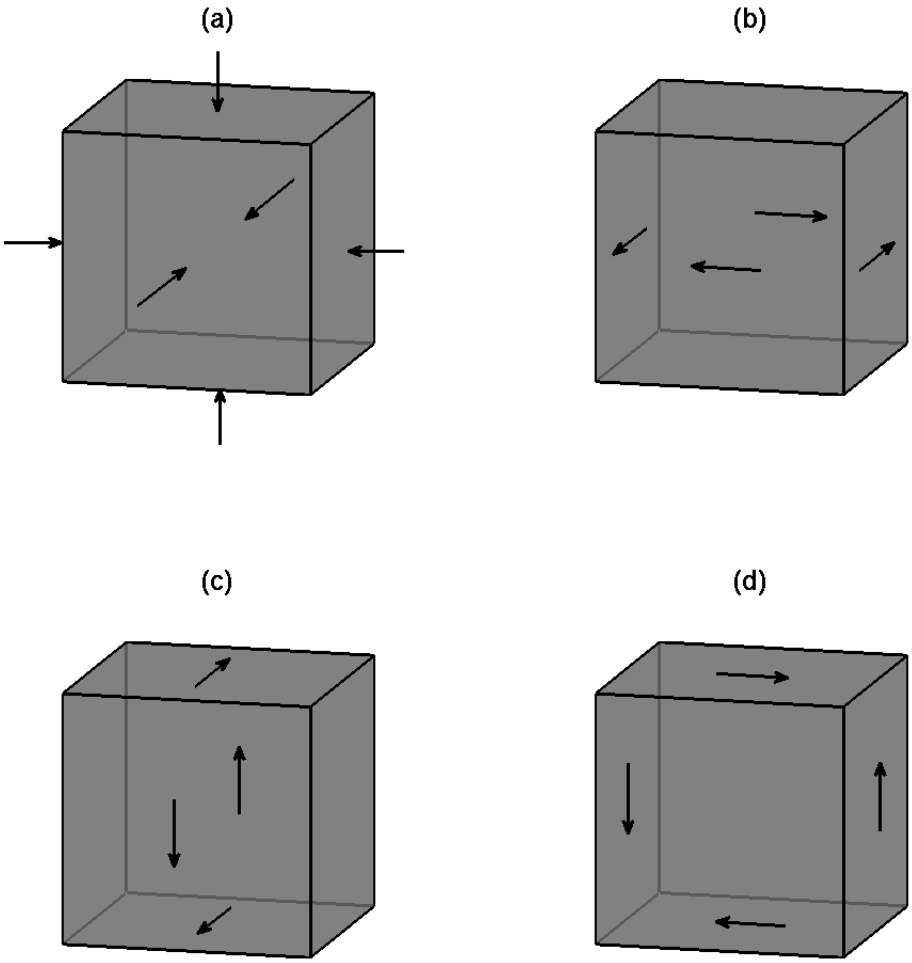

Figure 4-13: Stress-strain calculations on a 3D sample. (a) pure compression calculation; (b) pure shear calculation along xy direction; (c) pure shear calculation along yz direction; (b) pure shear calculation along xz direction.

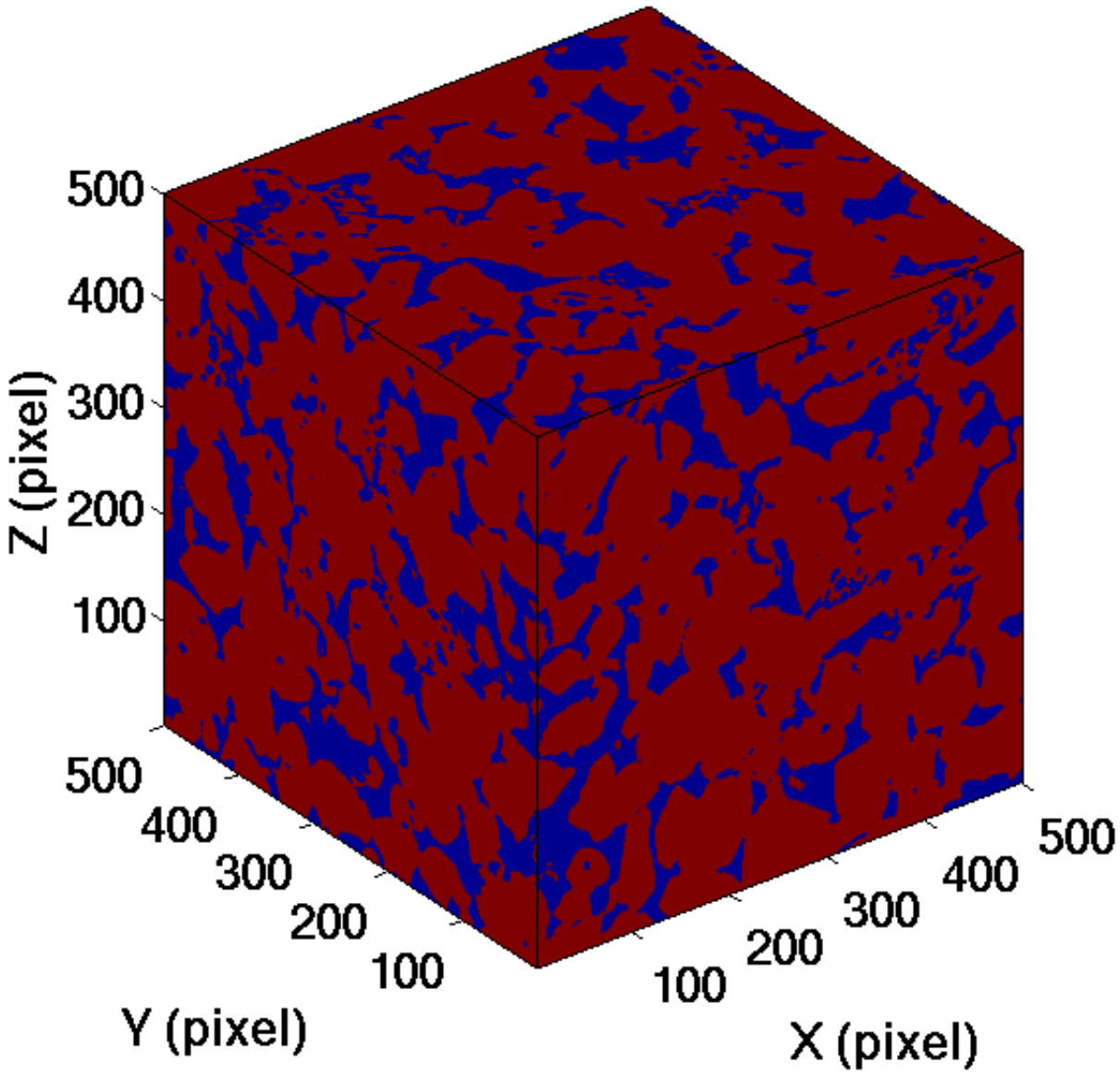

Figure 4-14: Segmented images for a 500^3 cubic subset of the 3D digitized Berea sandstone. Grains are represented in red and pores are in blue.

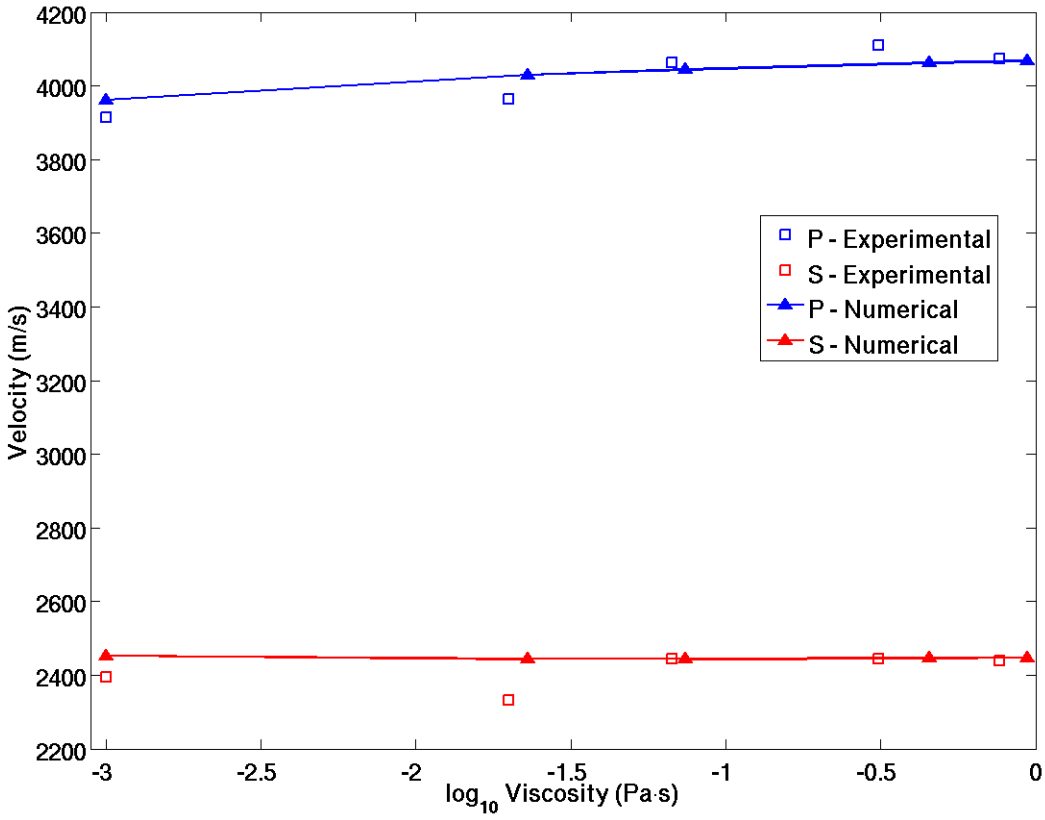

Figure 4-15: Numerically computed velocities of both P- and S-waves on the 500^3 pixels cubic subset of the 3D digitized Berea sandstone for different fluids, which match the laboratory measurements well.

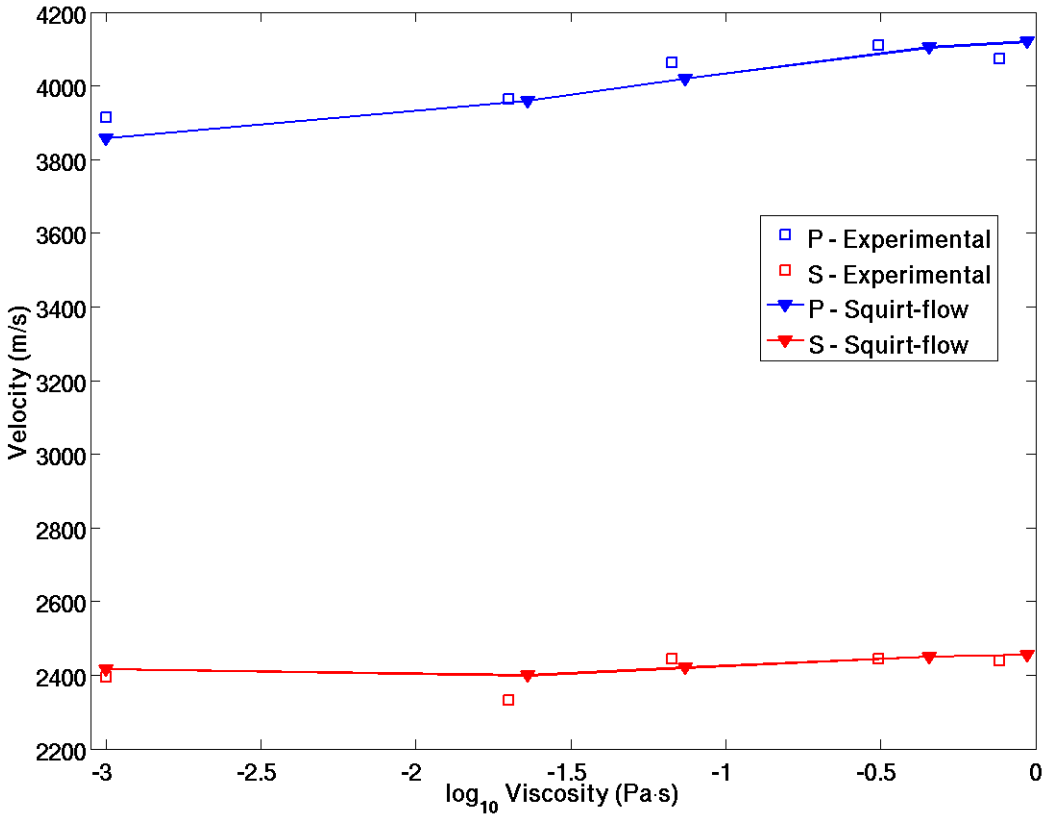

Figure 4-16: Theoretically predicted velocities of both P- and S-waves on the 500^3 cubic subset of the 3D digitized Berea sandstone with the modified squirt-flow model for different fluids, which also match the laboratory measurements well.

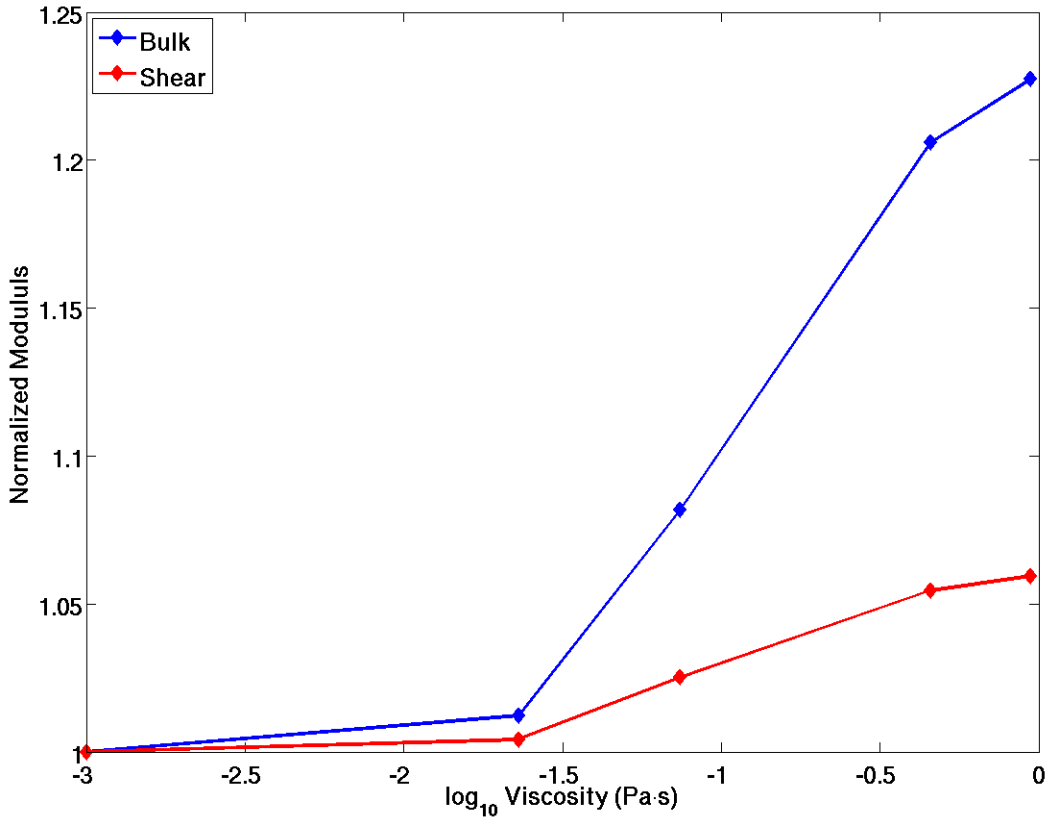

Figure 4-17: Partially relaxed frame bulk and shear moduli predicted from the modified squirt-flow model. The increase of the moduli with viscosities of fluids is consistent with laboratory observations [Han, 1986, Khazanehdari and Sothcott, 2003].

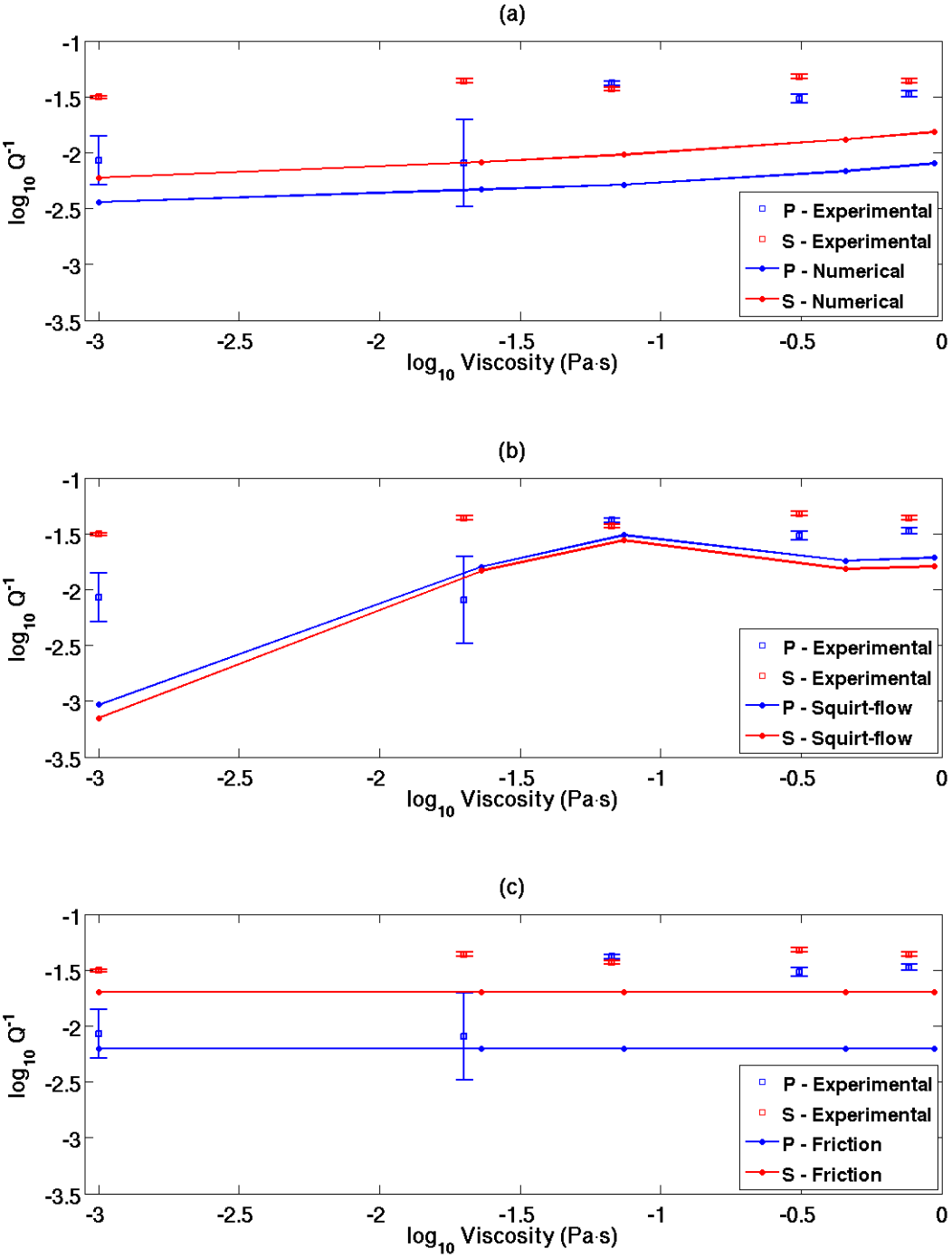

Figure 4-18: Attenuations due to viscous fluid and friction loss. (a) numerically computed attenuations due to viscous fluid in stiff pores; (b) theoretically predicted attenuations due to viscous fluid in compliant pores; (c) attenuations due to friction loss along the surfaces of cracks.

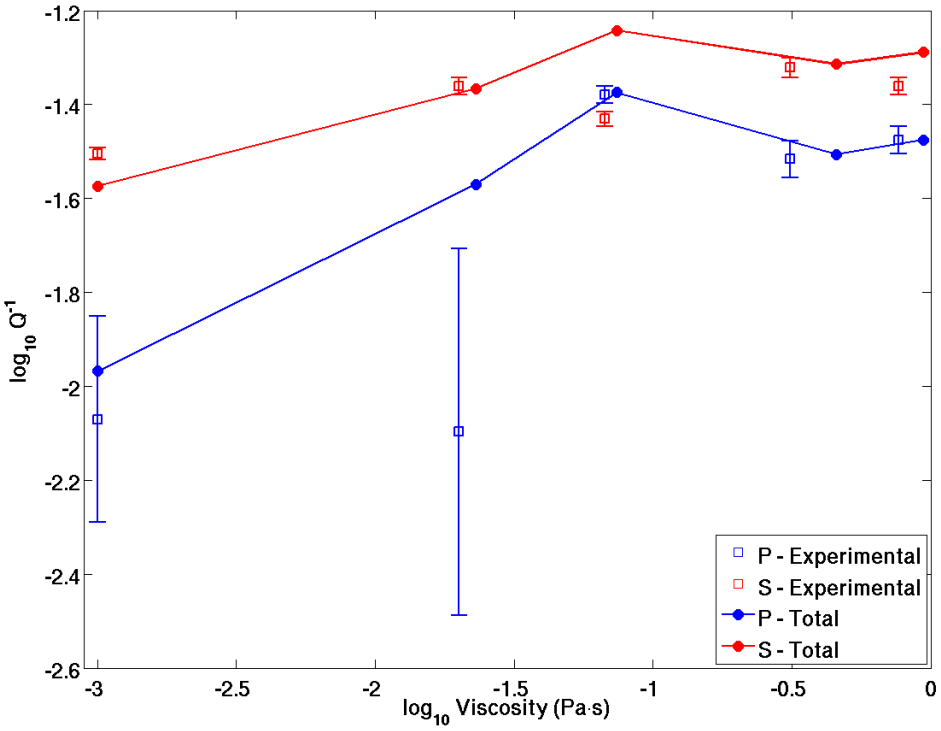

Figure 4-19: Total attenuations of both P- and S-waves of the 3D digitized Berea sandstone for different fluids, which is the sum of the attenuations computed numerically, predicted theoretically and friction loss. The total attenuation matches the laboratory measurements well.

Chapter 5

Conclusions and Future Work

5.1 Conclusions

In this thesis, I studied the effects of wave-induced fluid motion on seismic velocity and attenuation in porous rocks. The goal of this work was to numerically model wave propagation in 3D digitized rocks saturated with fluids and to determine the seismic responses in terms of velocity and attenuation. Numerical modeling provides an efficient way to control the conditions and inputs, which are difficult to accomplish in laboratory experiments. In numerical modeling it is possible to isolate the factors which we believe are important and to simulate their effects on the seismic responses, such as velocities, attenuations and dispersions.

We developed and used a multi-physics solver to simulate the wave propagation in a poroelastic material with Newtonian fluid and high property contrast. A single mathematical form was applied to both the solid and fluid cells, and the use of the rotated-staggered-grid finite-difference scheme allows stable solutions without explicitly and separately handling the solid-fluid boundary conditions. The von Neumann analysis was applied to characterize the numerical stability of the solution in the fluid cells. Asymptotic bounds were found on the stable region for the small-viscosity and large-viscosity cases, but it was noted that typical pore fluids in nature could be considered as the small-viscosity case for stability analysis. Tests on an idealized porous medium consisting of alternating solid and viscous fluid layers show that the

new implementation provides stable results and agrees with analytical solutions both for velocities and attenuations of compressional waves.

Realizing the significant impact of the small cracks lost during the imaging process on the computed effective elastic properties of digitized porous rocks, we developed a Monte-Carlo inversion algorithm to recover the small cracks lost. We hybridized the numerical computation with effective media theories such as the differential effective media theory and the Kuster-Toksöz model. Using these, we can determine the effective elastic properties of rocks saturated with different fluids. In the Monte-Carlo inversion, we only need limited laboratory data of velocities of P- and S-waves such as those measuring dry and water-saturated cases. Once the crack distribution is obtained, we are able to predict the effective elastic properties of rocks saturated with other types of fluids. The inversion results may have uncertainties. However, since we used the elastic moduli computed from the digitized 3D rock as an intermediate step in our hybrid method, we actually captured most of the information about the micro-structures of the rocks. Therefore, the inversion results of cracks based on such digitized 3D rocks should be much more meaningful than those inverted by using a theoretical model alone, which has to invert the whole spectrum of crack distribution — both stiff pores and compliant cracks — rather than small cracks alone as in our inversion.

To study the seismic responses of porous rocks saturated with different types of fluids, I developed the stress-strain calculation to compute the velocity and attenuation of rocks with sizes of which are much smaller than the seismic wavelength of interest. This is critical for numerical simulation because we are always limited by the computational resources available. Therefore, smaller size of rocks is preferred in modeling. In addition to the impact on the velocity, crack is also the dominant factor affecting attenuation of porous rocks. Besides the compensation to velocity, we also developed a methodology to compensate for the attenuation due to the cracks that are lost in the imaging process. In addition to the measured velocities for dry and water-saturated cases, we further utilized the attenuation data of P-waves in the inversion for crack distribution. The modified squirt-flow model had been employed

to compute the attenuation due to small cracks lost. The total attenuation is the sum of the numerically computed attenuation due to the viscous fluid in stiff pores, the theoretically predicted one due to the viscous fluid in compliant pores and the friction loss. The numerically computed and theoretically predicted velocities match the laboratory measurements well, as does the total attenuation. This demonstrates the capability of this proposed method to numerically determine the velocity dispersion and attenuation with the digitized rocks. In summary, the hybrid method to compute the viscosity-dependent velocity and attenuation is:

1. The Voigt-Reuss-Hill average to estimate the effective elastic properties of digitized matrix consisting of different minerals.

2. The Monte-Carlo inversion to estimate the crack distribution, in which two rounds of inversion are carried out. In the first round inversion, using the Kuster-Toksöz model, we fit the laboratory measured velocities of P- and S-waves for dry and water-saturated rocks; in the second round inversion, using the modified squirt-flow model, we fit the measured attenuation data of P-waves for rocks saturated with different fluids to refine the crack distribution obtained in the first round inversion.

3. Compute the final viscosity-dependent velocity and attenuation of saturated rocks with the inverted crack distribution.

Compared to the traditional methods using only theoretical models, such as the BISQ model [Dvorkin and Nur, 1993, Dvorkin et al., 1994, Marketos and Best, 2010], to explain the laboratory measurements, the method using digitized porous rocks with resolved stiff pores has provided much more information about the micro-structures of the rocks. Therefore, the numerical study based on these digitized rocks shows many advantages over those studies using theoretical models alone, even though resolution of the digitized rocks might be low with respect to small features like cracks, since many parameters, such as tortuosity and squirt-flow length etc., used in the theoretical models are hard to physically defined. However, this will not be a problem for

numerical computation with digitized rocks since the 3D data stands on its own and contains these information.

In summary, the contributions made in this thesis are:

1. Developed a multi-physics solver to couple the elastic solid and viscous fluid for seismic wave propagation. The rotated-staggered-grid finite-difference scheme was employed to handle the high material contrast and the complex microstructures of 3D digitized rocks.

2. An "effective media" approach has been combined with the numerical approach to calculate the effective elastic properties of digitized matrix. This hybrid scheme can recover small features, such as cracks, in the digitized matrix of porous rocks that are lost during the imaging process. By using such a hybrid approach, we help resolve the discrepencies observed between numerical results and laboratory measurements and predict the effective elastic properties of saturated porous rocks with a limited number of laboratory measurements.

3. Developed the stress-strain calculation method to compute the seismic properties of saturated porous rock samples whose sizes are much smaller than the seismic wavelength of interest.

4. Incorporated the squirt-flow mechanism into the numerically computed results for accurately calculating the total attenuation, including the contribution of viscous fluid in cracks lost in the imaging process. The extended hybrid approach can predict both the seismic velocities of saturated porous rocks and the attenuations.

5. Attenuation is much more sensitive to the viscosity of the saturating fluid than velocity is, and attenuation due to the viscous fluid in compliant pores is greater than that due to viscous fluid in stiff pores.

5.2 Future Work

The ultimate goal of computational rock physics is to supplement the laboratory experiments with numerical computations. To be able to do so, we first have to guarantee that the numerical solvers are capable of capturing the complex physics, such as friction and viscous fluid effect; second, the resolution of the digitized porous rocks has to be high enough to capture as many small features, which are able to significantly affect the acoustical properties of porous rocks, of the complex micro-structures of rocks as possible; third, with powerful solvers and high resolution digitized data, we also need to have enough computational resources to be able to simulate models with meaningful size and within reasonable time, especially for studying the dynamic seismic responses. Unfortunately, none of the above requirements can be fully fulfilled in my study at the current stage. Therefore, the idea of hybridizing numerical computation with theoretical models is actually a practical approach to study the velocity dispersion and attenuation of porous rocks in 3D digitized data, until we can carry out the pure and brutal-force numerical computation with high resolution 3D digitized rocks in the future.

As mentioned in the title of this thesis, we study the effects of wave-induced fluid motion. However, in the papers published so far on mathematical derivations of wave-induced fluid flow at local scale, such as cracks, I have not observed that the solution of the nonlinear term or the convection term in the Navier-Stokes equation has been included. We understand the difficulty of solving a nonlinear system, but whether it is physically appropriate to drop the nonlinear term is still debatable in some situations. However, researchers studying wave-induced fluid flow on macro-scale with the help of the poroelasticity theory usually assume a Darcy type of fluid flow. It is hard to imagine how fluid can flow on macroscale if it was unable to do so in microscale, but researchers believe that this indeed takes place at frequencies sufficiently low. So far, no laboratory experiment or observation can verify whether wave-induced fluid flow happens or not. If it indeed happens, what is the magnitude of the velocity of such flow? We believe this can be answered by numerical computation at low

frequency on large models since large models can exhibit enough heterogeneities in which high pressure gradient field might be developed. In Appendix F, we developed a nonlinear solver which keeps the nonlinear term in numerical computation to simulate the wave-induced fluid flow for single viscous fluid. We have not seen much difference in results computed from the linear and nonlinear solvers on the same cases tested; this could be due to the small size of the 3D models on which we are able to work, and that the frequencies we are able to simulate are still not low enough. This nonlinear phenomenon related to wave-induced fluid flow needs further investigation, when computational resources become feasible.

In the modeling of the low-frequency responses of porous rocks to viscous fluids, since the period of the seismic wave of interest increases, for a given time stepping Δt, the total time step need to be simulated increases as well. Especially, the increasing of time step becomes significant for frequencies below 100 Hz. One solution to speed up the computation is to take advantages of GPU computing. Shown as an example in Figure 5-1, by simply implementing GPU computing without optimizing the memory usage, we directly gained 6X speed. The computing time will increase further if high resolution digitized data are used in the future. We believe the GPU can make a difference for modeling work with large models at lower frequencies, especially for 3D models and nonlinear problems.

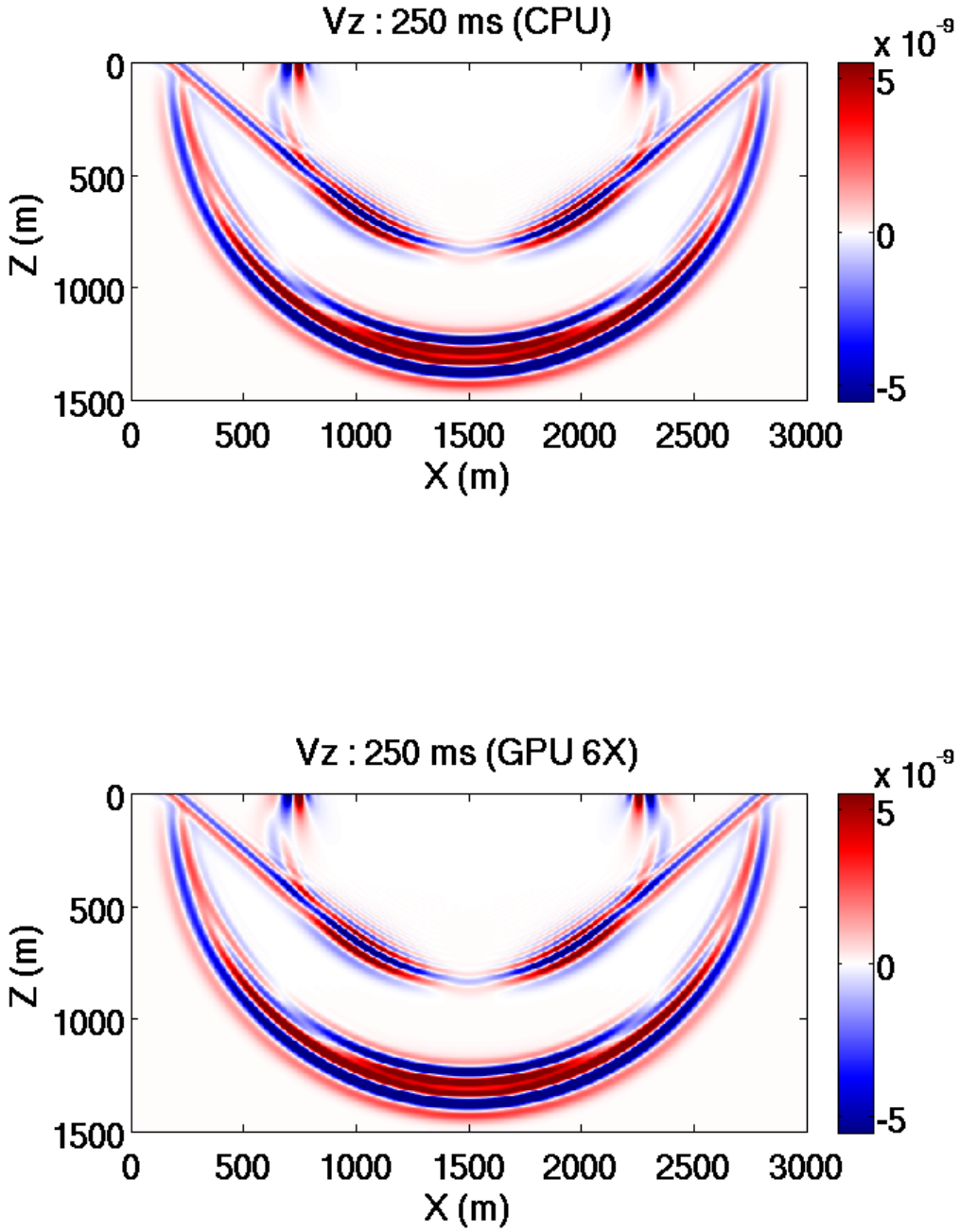

Figure 5-1: Comparison between CPU and GPU computing. The GPU computing is able to gain at least 6X speed from direct implementation.

Appendix A

Rotated-Staggered-Grid Finite-Difference Scheme in 2D and 3D

Saenger et al. [2000] employed a so-called rotated-staggered-grid (RSG) finite-difference scheme to model seismic wave propagating through fractured media where high material contrast exists between solid frame and inclusions (i.e. gas and water). One of the advantages of using RSG scheme is to handle such high contrast because it places all components of the stiffness tensor at the same position within each cell — at the center of each cell. In such way, it avoid averaging shear moduli of neighboring cells for updating shear stresses as does standard-staggered-grid (SSG) scheme [Virieux, 1986], which causes numerical instability. The other advantages of RSG are that it has the same stability criteria for both 2D and 3D cases, which allows to choose larger Δt than SSG does, and it can also handle anisotropy of medium up to triclinic and the problem with free-surface topography as well.

A.1 Finite Difference Scheme in 2D

In a grid with rectangular cells of length $(\Delta x, \Delta z)$ along coordinates (x, z), as shown in Figure A-1, two different sets of variables are defined at corners $(m\Delta x, n\Delta z)$ and

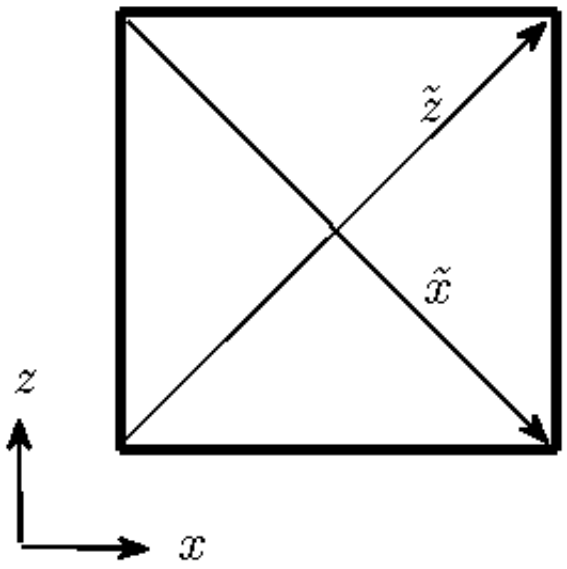

Figure A-1: Rotated coordinate system in 2D.

centers $\left(m\Delta x + \frac{\Delta x}{2}, n\Delta z + \frac{\Delta z}{2}\right)$ of each cell, respectively. To approximate the first-order derivatives $\left(\frac{\partial}{\partial x}, \frac{\partial}{\partial z}\right)_{m+\frac{1}{2},n+\frac{1}{2}}$ at center, one has to choose a set of new derivative direction $(\widetilde{x}, \widetilde{z})$, which can be defined as,

$$\begin{bmatrix} \widetilde{x} \\ \widetilde{z} \end{bmatrix} = \begin{bmatrix} \frac{\Delta x}{\Delta r} & -\frac{\Delta z}{\Delta r} \\ \frac{\Delta x}{\Delta r} & \frac{\Delta z}{\Delta r} \end{bmatrix} \begin{bmatrix} x \\ z \end{bmatrix} \tag{A.1}$$

where $\Delta r = \sqrt{\Delta x^2 + \Delta z^2}$. Let us define

$$\mathbf{T} = \begin{bmatrix} \frac{\Delta x}{\Delta r} & -\frac{\Delta z}{\Delta r} \\ \frac{\Delta x}{\Delta r} & \frac{\Delta z}{\Delta r} \end{bmatrix} \tag{A.2}$$

which is the transformation matrix from basis (x, z) to $(\widetilde{x}, \widetilde{z})$. For case with $\Delta x = \Delta z$, we have

$$\mathbf{T} = \begin{bmatrix} \frac{\sqrt{2}}{2} & -\frac{\sqrt{2}}{2} \\ \frac{\sqrt{2}}{2} & \frac{\sqrt{2}}{2} \end{bmatrix} \tag{A.3}$$

From equations (A.1) and (A.3) and by taking $\mathbf{T}^{-1}$, we can obtain

$$\begin{bmatrix} x \\ z \end{bmatrix} = \begin{bmatrix} \frac{\sqrt{2}}{2} & \frac{\sqrt{2}}{2} \\ -\frac{\sqrt{2}}{2} & \frac{\sqrt{2}}{2} \end{bmatrix} \begin{bmatrix} \widetilde{x} \\ \widetilde{z} \end{bmatrix} \tag{A.4}$$

According to equation (A.4), derivatives in (x, z) can be expressed by a linear combination of derivatives in $(\widetilde{x}, \widetilde{z})$.

$$\frac{\partial}{\partial x} = \frac{\sqrt{2}}{2}\left(\frac{\partial}{\partial \widetilde{z}} + \frac{\partial}{\partial \widetilde{x}}\right) \tag{A.5}$$

$$\frac{\partial}{\partial z} = \frac{\sqrt{2}}{2}\left(\frac{\partial}{\partial \widetilde{z}} - \frac{\partial}{\partial \widetilde{x}}\right) \tag{A.6}$$

In numerical simulation, we must define finite difference operators D_x and D_z to approximate the partial differentiations $\frac{\partial}{\partial x}$ and $\frac{\partial}{\partial z}$ in (x, z). However, for RSG scheme,

the second order operators performed in $(\widetilde{x},\widetilde{z})$ have to be defined first as

$$\begin{aligned} D_{\widetilde{x}}u\left(x,z,t\right) &= \frac{\left[u\left(x+\frac{\Delta x}{2},z-\frac{\Delta z}{2},t\right)-u\left(x-\frac{\Delta x}{2},z+\frac{\Delta z}{2},t\right)\right]}{\sqrt{2}\Delta x} \\ D_{\widetilde{z}}u\left(x,z,t\right) &= \frac{\left[u\left(x+\frac{\Delta x}{2},z+\frac{\Delta z}{2},t\right)-u\left(x-\frac{\Delta x}{2},z-\frac{\Delta z}{2},t\right)\right]}{\sqrt{2}\Delta x} \end{aligned}$$

Then according to equations (A.5) and (A.6), we can have operators D_x and D_z as

$$\begin{aligned} D_x u(x,z,t) &= \frac{1}{2}\left[D_{\widetilde{z}}u\left(x,z,t\right)+D_{\widetilde{x}}u\left(x,z,t\right)\right] \\ D_z u(x,z,t) &= \frac{1}{2}\left[D_{\widetilde{z}}u\left(x,z,t\right)-D_{\widetilde{x}}u\left(x,z,t\right)\right] \end{aligned}$$

A.2 Finite Difference Scheme in 3D

In a grid with cubic cells of length $(\Delta x,\Delta y,\Delta z)$ along coordinates (x,y,z), as shown in Figure A-2, two different sets of variables are defined at corners $(m\Delta x,k\Delta y,n\Delta z)$ and centers $\left(m\Delta x+\frac{\Delta x}{2},k\Delta y+\frac{\Delta y}{2},n\Delta z+\frac{\Delta z}{2}\right)$ of each cell, respectively. To approximate the first-order derivatives $\left(\frac{\partial}{\partial x},\frac{\partial}{\partial y},\frac{\partial}{\partial z}\right)_{m+\frac{1}{2},k+\frac{1}{2},n+\frac{1}{2}}$ at center, one has to choose a set of new derivative directions $\left(\widetilde{d}_1,\widetilde{d}_2,\widetilde{d}_3,\widetilde{d}_4\right)$ along diagonals, which can be defined as,

$$\begin{bmatrix} \widetilde{d}_1 \\ \widetilde{d}_2 \\ \widetilde{d}_3 \\ \widetilde{d}_4 \end{bmatrix} = \begin{bmatrix} \frac{\Delta x}{\Delta l} & \frac{\Delta y}{\Delta l} & \frac{\Delta z}{\Delta l} \\ \frac{\Delta x}{\Delta l} & \frac{\Delta y}{\Delta l} & -\frac{\Delta z}{\Delta l} \\ \frac{\Delta x}{\Delta l} & -\frac{\Delta y}{\Delta l} & \frac{\Delta z}{\Delta l} \\ \frac{\Delta x}{\Delta l} & -\frac{\Delta y}{\Delta l} & -\frac{\Delta z}{\Delta l} \end{bmatrix} \begin{bmatrix} x \\ y \\ z \end{bmatrix} \tag{A.7}$$

where $\Delta l=\sqrt{\Delta x^2+\Delta y^2+\Delta z^2}$. Let us define

$$\widetilde{\mathbf{d}} = \begin{bmatrix} \widetilde{d}_1 \\ \widetilde{d}_2 \\ \widetilde{d}_3 \\ \widetilde{d}_4 \end{bmatrix} \tag{A.8}$$

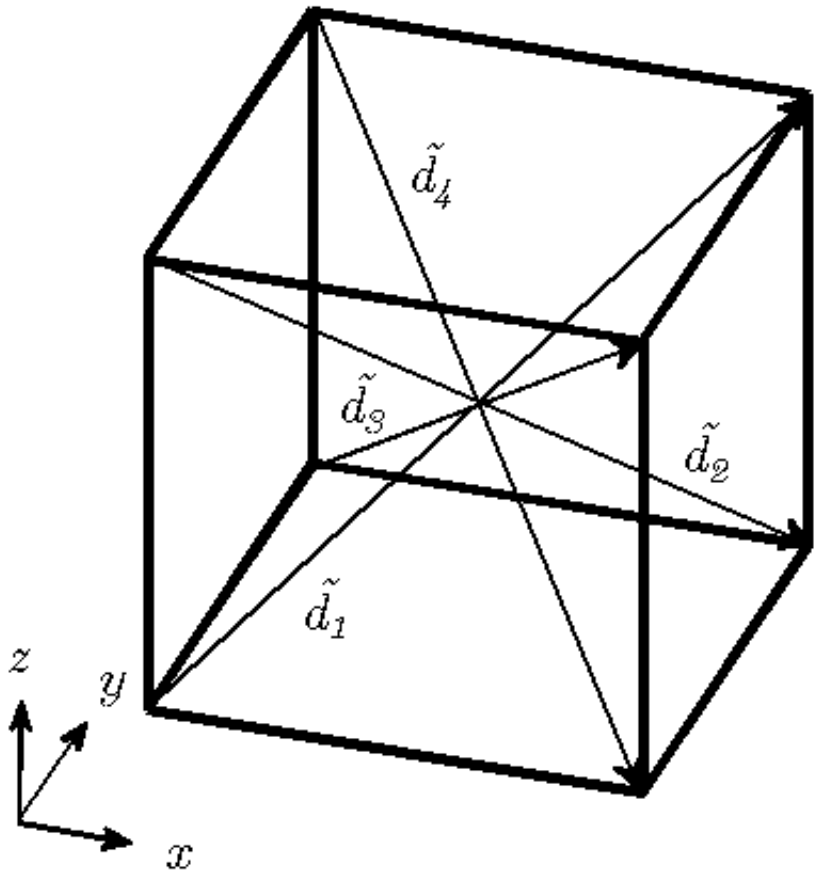

Figure A-2: Rotated coordinate system in 3D.

$$\mathbf{x} = \begin{bmatrix} x \\ y \\ z \end{bmatrix} \tag{A.9}$$

$$\mathbf{T} = \begin{bmatrix} \frac{\Delta x}{\Delta l} & \frac{\Delta y}{\Delta l} & \frac{\Delta z}{\Delta l} \\ \frac{\Delta x}{\Delta l} & \frac{\Delta y}{\Delta l} & -\frac{\Delta z}{\Delta l} \\ \frac{\Delta x}{\Delta l} & -\frac{\Delta y}{\Delta l} & \frac{\Delta z}{\Delta l} \\ \frac{\Delta x}{\Delta l} & -\frac{\Delta y}{\Delta l} & -\frac{\Delta z}{\Delta l} \end{bmatrix} \tag{A.10}$$

such that equation (A.7) can be expressed as

$$\widetilde{\mathbf{d}} = \mathbf{T}\mathbf{x} \tag{A.11}$$

where $\mathbf{T}$ is the transformation matrix from basis (x, y, z) to $\left(\widetilde{d}_1, \widetilde{d}_2, \widetilde{d}_3, \widetilde{d}_4\right)$. For case with $\Delta x = \Delta y = \Delta z$, we have

$$\mathbf{T} = \begin{bmatrix} \frac{\sqrt{3}}{3} & \frac{\sqrt{3}}{3} & \frac{\sqrt{3}}{3} \\ \frac{\sqrt{3}}{3} & \frac{\sqrt{3}}{3} & -\frac{\sqrt{3}}{3} \\ \frac{\sqrt{3}}{3} & -\frac{\sqrt{3}}{3} & \frac{\sqrt{3}}{3} \\ \frac{\sqrt{3}}{3} & -\frac{\sqrt{3}}{3} & -\frac{\sqrt{3}}{3} \end{bmatrix} \tag{A.12}$$

Since $\mathbf{T}$ is not a square matrix, we must multiply $\mathbf{T}^T$ on both sides of equation (A.11). So we can have

$$\mathbf{x} = \left(\mathbf{T}^T\mathbf{T}\right)^{-1}\mathbf{T}^T\widetilde{\mathbf{d}} \tag{A.13}$$

and in explicit form

$$\begin{bmatrix} x \\ y \\ z \end{bmatrix} = \frac{\sqrt{3}}{4}\begin{bmatrix} 1 & 1 & 1 & 1 \\ 1 & 1 & -1 & -1 \\ 1 & -1 & 1 & -1 \end{bmatrix}\begin{bmatrix} \widetilde{d}_1 \\ \widetilde{d}_2 \\ \widetilde{d}_3 \\ \widetilde{d}_4 \end{bmatrix} \tag{A.14}$$

According to equation (A.14), derivatives in (x, y, z) can be expressed by a linear combination of derivatives in $\left(\widetilde{d}_1, \widetilde{d}_2, \widetilde{d}_3, \widetilde{d}_4\right)$.

$$\frac{\partial}{\partial x} = \frac{\sqrt{3}}{4}\left(\frac{\partial}{\partial \widetilde{d}_1} + \frac{\partial}{\partial \widetilde{d}_2} + \frac{\partial}{\partial \widetilde{d}_3} + \frac{\partial}{\partial \widetilde{d}_4}\right) \tag{A.15}$$

$$\frac{\partial}{\partial y} = \frac{\sqrt{3}}{4}\left(\frac{\partial}{\partial \widetilde{d}_1} + \frac{\partial}{\partial \widetilde{d}_2} - \frac{\partial}{\partial \widetilde{d}_3} - \frac{\partial}{\partial \widetilde{d}_4}\right) \tag{A.16}$$

$$\frac{\partial}{\partial z} = \frac{\sqrt{3}}{4}\left(\frac{\partial}{\partial \widetilde{d}_1} - \frac{\partial}{\partial \widetilde{d}_2} + \frac{\partial}{\partial \widetilde{d}_3} - \frac{\partial}{\partial \widetilde{d}_4}\right) \tag{A.17}$$

In numerical simulation, we must define finite difference operators D_x, D_y and D_z to approximate the partial differentiations $\frac{\partial}{\partial x}$, $\frac{\partial}{\partial y}$ and $\frac{\partial}{\partial z}$ in (x, y, z). However, for RSG scheme, second order operators performed in $\left(\widetilde{d}_1, \widetilde{d}_2, \widetilde{d}_3, \widetilde{d}_4\right)$ have to be defined first as

$$D_{\widetilde{d}_1} u(x,y,z,t) = \frac{\left[u\left(x+\frac{\Delta x}{2}, y+\frac{\Delta y}{2}, z+\frac{\Delta z}{2}, t\right) - u\left(x-\frac{\Delta x}{2}, y-\frac{\Delta y}{2}, z-\frac{\Delta z}{2}, t\right)\right]}{\sqrt{3}\Delta x}$$

$$D_{\widetilde{d}_2} u(x,y,z,t) = \frac{\left[u\left(x+\frac{\Delta x}{2}, y+\frac{\Delta y}{2}, z-\frac{\Delta z}{2}, t\right) - u\left(x-\frac{\Delta x}{2}, y-\frac{\Delta y}{2}, z+\frac{\Delta z}{2}, t\right)\right]}{\sqrt{3}\Delta x}$$

$$D_{\widetilde{d}_3} u(x,y,z,t) = \frac{\left[u\left(x+\frac{\Delta x}{2}, y-\frac{\Delta y}{2}, z+\frac{\Delta z}{2}, t\right) - u\left(x-\frac{\Delta x}{2}, y+\frac{\Delta y}{2}, z-\frac{\Delta z}{2}, t\right)\right]}{\sqrt{3}\Delta x}$$

$$D_{\widetilde{d}_4} u(x,y,z,t) = \frac{\left[u\left(x+\frac{\Delta x}{2}, y-\frac{\Delta y}{2}, z-\frac{\Delta z}{2}, t\right) - u\left(x-\frac{\Delta x}{2}, y+\frac{\Delta y}{2}, z+\frac{\Delta z}{2}, t\right)\right]}{\sqrt{3}\Delta x}$$

Then according to equations (A.15) - (A.17), we can have operators D_x, D_y and D_z as

$$D_x u(x,z,t) = \frac{1}{4}\left[D_{\widetilde{d}_1} u(x,y,z,t) + D_{\widetilde{d}_2} u(x,y,z,t) + D_{\widetilde{d}_3} u(x,y,z,t) + D_{\widetilde{d}_4} u(x,y,z,t)\right]$$

$$D_y u(x,z,t) = \frac{1}{4}\left[D_{\widetilde{d}_1} u(x,y,z,t) + D_{\widetilde{d}_2} u(x,y,z,t) - D_{\widetilde{d}_3} u(x,y,z,t) - D_{\widetilde{d}_4} u(x,y,z,t)\right]$$

$$D_z u(x,z,t) = \frac{1}{4}\left[D_{\widetilde{d}_1} u(x,y,z,t) - D_{\widetilde{d}_2} u(x,y,z,t) + D_{\widetilde{d}_3} u(x,y,z,t) - D_{\widetilde{d}_4} u(x,y,z,t)\right]$$

Appendix B

Analytical Solution for the Dispersion and Attenuation of a Compressional Wave in an Idealized Porous Medium

The propagation of a compressional wave in an idealized porous medium with periodically alternating solid and viscous fluid layers denoted by s and f is governed by [Brekhovskikh, 1981, Ciz et al., 2006],

$$\begin{aligned} 4\left(\mu_s-\mu_f\right)^2 K_1K_2+\omega^2\rho_s\left[c^2\rho_s-4\left(\mu_s-\mu_f\right)\right]K_2\tan\frac{\beta_s h_s}{2} \\ +\omega^2\rho_f\left[c^2\rho_f+4\left(\mu_s-\mu_f\right)\right]K_1\tan\frac{\beta_f h_f}{2} \\ -\omega^2\rho_s\rho_f c^2\left[L_1\tan\frac{\beta_f h_f}{2}+L_2\tan\frac{\beta_s h_s}{2}\right] &= 0 \end{aligned} \tag{B.1}$$

where,

$$\begin{aligned} K_1 &= \frac{\omega^2}{c^2}\tan\frac{\beta_s h_s}{2}+\alpha_s\beta_s\tan\frac{\alpha_s h_s}{2} \\ K_2 &= \frac{\omega^2}{c^2}\tan\frac{\beta_f h_f}{2}+\alpha_f\beta_f\tan\frac{\alpha_f h_f}{2} \\ L_1 &= \frac{\omega^2}{c^2}\tan\frac{\beta_s h_s}{2}-\alpha_f\beta_s\tan\frac{\alpha_f h_f}{2} \\ L_2 &= \frac{\omega^2}{c^2}\tan\frac{\beta_f h_f}{2}-\alpha_s\beta_f\tan\frac{\alpha_s h_s}{2} \end{aligned}$$

and where

$$\begin{aligned} \alpha_s^2 &= \omega^2 \left(\frac{1}{c_s^2} - \frac{1}{c^2} \right) \\ \alpha_f^2 &= \omega^2 \left(\frac{1}{c_f^2} - \frac{1}{c^2} \right) \end{aligned}$$

with

$$\begin{aligned} c_s &= \sqrt{\frac{\left(K_s + \frac{4}{3}\mu_s\right)}{\rho_s}} \\ c_f &= \sqrt{\frac{\left(K_f + \frac{4}{3}\mu_f\right)}{\rho_f}} \end{aligned}$$

being the compressional wave velocity in the solid and fluid, respectively, and where

$$\begin{aligned} \beta_s^2 &= \omega^2 \left(\frac{1}{b_s^2} - \frac{1}{c^2} \right) \\ \beta_f^2 &= \omega^2 \left(\frac{1}{b_f^2} - \frac{1}{c^2} \right) \end{aligned}$$

with

$$\begin{aligned} b_s &= \sqrt{\frac{\mu_s}{\rho_s}} \\ b_f &= \sqrt{\frac{\mu_f}{\rho_f}} \end{aligned}$$

being the shear wave velocity in the solid and fluid, respectively.

$$\begin{aligned} \mu_f &= -i\omega\eta \\ K_f &= \lambda_f + \frac{2}{3}\mu_f \end{aligned}$$

h_s and h_f are the thickness of the solid and fluid layers, respectively. c is the speed of the compressional wave propagating in such a system. Once we obtain c, we can

estimate the wave attenuation as,

$$\frac{1}{Q_p} = \frac{\mathrm{Im}\left\{c^{-2}\right\}}{\mathrm{Re}\left\{c^{-2}\right\}} \tag{B.2}$$

Appendix C

Stability Analysis for Linearized Navier-Stokes Equations in 2D

In a 2D case, the linearized Navier-Stokes equations are [Landau and Lifshitz, 1959]:

$$\begin{aligned}
\rho_f \frac{\partial v_x}{\partial t} &= -\frac{\partial p}{\partial x} + \frac{\partial \sigma_{xx}}{\partial x} + \frac{\partial \sigma_{xz}}{\partial z} \\
\rho_f \frac{\partial v_z}{\partial t} &= -\frac{\partial p}{\partial z} + \frac{\partial \sigma_{xz}}{\partial x} + \frac{\partial \sigma_{zz}}{\partial z} \\
\frac{\partial p}{\partial t} &= -K_f \left(\frac{\partial v_x}{\partial x} + \frac{\partial v_z}{\partial z} \right) \\
\sigma_{xx} &= (\eta_\lambda + 2\eta_\mu) \frac{\partial v_x}{\partial x} + \eta_\lambda \frac{\partial v_z}{\partial z} \\
\sigma_{zz} &= \eta_\lambda \frac{\partial v_x}{\partial x} + (\eta_\lambda + 2\eta_\mu) \frac{\partial v_z}{\partial z} \\
\sigma_{xz} &= \eta_\mu \left(\frac{\partial v_x}{\partial z} + \frac{\partial v_z}{\partial x} \right)
\end{aligned} \tag{C.1}$$

where v_i, σ_{ij}, p are the velocity, stress rates and pressure field, K_f, ρ_f, η_μ and η_λ are the bulk modulus, density, shear viscosity and second viscosity of the viscous fluid. In a finite difference scheme, equations (C.1) are approximated as difference equations

using discrete difference operators D_t and D_x (see Appendix A for details),

$$\begin{aligned}
\rho_f D_t v_x &= -D_x p + D_x \sigma_{xx} + D_z \sigma_{xz} \\
\rho_f D_t v_z &= -D_z p + D_x \sigma_{xz} + D_z \sigma_{zz} \\
D_t p &= -K_f \left(D_x v_x + D_z v_z \right) \\
\sigma_{xx} &= \left(\eta_\lambda + 2\eta_\mu \right) D_x v_x + \eta_\lambda D_z v_z \\
\sigma_{zz} &= \eta_\lambda D_x v_x + \left(\eta_\lambda + 2\eta_\mu \right) D_z v_z \\
\sigma_{xz} &= \eta_\mu \left(D_z v_x + D_x v_z \right)
\end{aligned} \tag{C.2}$$

Define the displacement u_x and u_z through relations,

$$\begin{aligned}
v_x &= D_t u_x \\
v_z &= D_t u_z
\end{aligned} \tag{C.3}$$

Then the equations (C.2) can be written in terms of the displacement as

$$\mathbf{A} u = 0 \tag{C.4}$$

where A, a 2×2 matrix operating on displacement vector $u = [u_x, u_z]^T$, is

$$\mathbf{A} = \begin{bmatrix}
\rho_f D_{tt} - K_f D_{xx} & -K_f D_{xz} - \left(\eta_\lambda + \eta_\mu \right) D_{txz} \\
- \left(\eta_\lambda + 2\eta_\mu \right) D_{txx} - \eta_\mu D_{tzz} & \\
 & \\
-K_f D_{xz} - \left(\eta_\lambda + \eta_\mu \right) D_{txz} & \rho_f D_{tt} - K_f D_{zz} \\
 & - \left(\eta_\lambda + 2\eta_\mu \right) D_{tzz} - \eta_\mu D_{txx}
\end{bmatrix} \tag{C.5}$$

In the von Neumann stability analysis, a time-harmonic plane wave is typically assumed,

$$\begin{bmatrix} u_x \left(m, n, l \right) \\ u_z \left(m, n, l \right) \end{bmatrix} = \begin{bmatrix} u_{0x} \\ u_{0z} \end{bmatrix} g(k)^l e^{i(k_x m \Delta x + k_z n \Delta z)} \tag{C.6}$$

where the grid spacing is $(\Delta x, \Delta z)$ and the time increment is Δt. In this analysis,

Δx and Δz are assumed equal. Stability of the numerical calculation requires,

$$|g(k)| \leq 1 \; \forall k \tag{C.7}$$

The values of $g(k)$ are obtained by solving equation (C.4), which requires the determinant of the system of equations to be equal to zero, i.e. $\det(\mathbf{A}) = 0$. The determinant then yields a quartic equation in $g(k)$,

$$g^4 + c_3 g^3 + c_2 g^2 + c_1 g + c_0 = 0 \tag{C.8}$$

where the coefficients c_i are functions of the physical properties of the viscous fluid, grid spacing and time increment defined as

$$\begin{aligned} c_3 &= \beta_{31}\phi - 4 \\ c_2 &= \beta_{22}\phi^2 - \beta_{21}\phi + 6 \\ c_1 &= -\beta_{12}\phi^2 + \beta_{11}\phi - 4 \\ c_0 &= \beta_{02}\phi^2 - \beta_{01}\phi + 1 \end{aligned} \tag{C.9}$$

$$\phi = 1 - \cos(k_x \Delta x)\cos(k_z \Delta x) \tag{C.10}$$

$$\begin{aligned} \beta_{31} &= \frac{2\pi_1 \Delta t^2}{\Delta x^2} + \frac{6\pi_2 \Delta t}{\Delta x^2} + \frac{2\pi_3 \Delta t}{\Delta x^2} \\ \beta_{22} &= \frac{4\pi_1 \pi_2 \Delta t^3}{\Delta x^4} + \frac{8\pi_2^2 \Delta t^2}{\Delta x^4} + \frac{4\pi_2 \pi_3 \Delta t^2}{\Delta x^4} \\ \beta_{21} &= \frac{4\pi_1 \Delta t^2}{\Delta x^2} + \frac{18\pi_2 \Delta t}{\Delta x^2} + \frac{6\pi_3 \Delta t}{\Delta x^2} \end{aligned}$$

$$
\begin{aligned}
\beta_{12} &= \frac{4\pi_1\pi_2\Delta t^3}{\Delta x^4} + \frac{16\pi_2^2\Delta t^2}{\Delta x^4} + \frac{8\pi_2\pi_3\Delta t^2}{\Delta x^4} \\
\beta_{11} &= \frac{2\pi_1\Delta t^2}{\Delta x^2} + \frac{18\pi_2\Delta t}{\Delta x^2} + \frac{6\pi_3\Delta t}{\Delta x^2} \\
\beta_{02} &= \frac{8\pi_2^2\Delta t^2}{\Delta x^4} + \frac{4\pi_2\pi_3\Delta t^2}{\Delta x^4} \\
\beta_{01} &= \frac{6\pi_2\Delta t}{\Delta x^2} + \frac{2\pi_3\Delta t}{\Delta x^2}
\end{aligned}
\tag{C.11}
$$

$$
\begin{aligned}
\pi_1 &= \frac{K_f}{\rho_f} \\
\pi_2 &= \frac{\eta_\mu}{\rho_f} \\
\pi_3 &= \frac{\eta_\lambda}{\rho_f}
\end{aligned}
\tag{C.12}
$$

Equation (C.8) is associated with the four roots of $g = \{\lambda_1, \lambda_2, \lambda_3, \lambda_4\}$ which may be real or complex values. The eigenvalue method [Press et al., 1992] is used to solve this quartic equation, where a Hessenberg matrix is constructed with the coefficients c_i as

$$
\mathbf{H} = \begin{bmatrix} -c_3 & -c_2 & -c_1 & -c_0 \\ 1 & 0 & 0 & 0 \\ 0 & 1 & 0 & 0 \\ 0 & 0 & 1 & 0 \end{bmatrix}
\tag{C.13}
$$

The four roots of equation (C.8) correspond to the four eigenvalues of matrix $\mathbf{H}$. The stability criterion requires the magnitudes of these four roots to be less than one for all k_x and k_z.

Appendix D

Kuster-Toksöz Model for Cracked Medium

In the Kuster-Toksöz model [Kuster and Toksöz, 1974], it assumes long-wavelength approximation and pores of spheres and oblate spheroids randomly distributed in an isotropic and homogeneous host medium.

Let us define properties of medium in terms of bulk modulus K, shear modulus μ and density ρ. (K, μ, ρ) refers to the matrix, $\left(K^{'}, \mu^{'}, \rho^{'}\right)$ refers to the inclusions and $(K^{*}, \mu^{*}, \rho^{*})$ refers to the effective properties of the composite medium. If c is the volume concentration of a set of inclusion with aspect ratio of α, we can have the relationships between these quantities

$$\frac{K^{*}-K}{3K^{*}+4\mu}=\frac{1}{3}\cdot\frac{K^{'}-K}{3K+4\mu}\cdot c\cdot T_{iijj}\left(\alpha\right)$$

$$\frac{\mu^{*}-\mu}{6\mu^{*}\left(K+2\mu\right)+\mu\left(9K+8\mu\right)}=\frac{\mu^{'}-\mu}{25\mu\left(3K+4\mu\right)}\cdot c\cdot\left[T_{ijij}-\frac{1}{3}T_{iijj}\right]$$

$$\rho^{*}=\rho\left(1-c\right)+c\rho^{'}$$

In case of multiple cracks with M sets of aspect ratios saturated with N multiple fluids, the equations above can be easily extended to

$$\frac{K^* - K}{3K^* + 4\mu} = \frac{1}{3}\sum_{n=1}^{N} \frac{K_n^{'} - K}{3K + 4\mu} \cdot \sum_{m=1}^{M} c\left(\alpha_{m,n}\right) \cdot T_{iijj}\left(\alpha_{m,n}\right)$$

$$\frac{\mu^* - \mu}{6\mu^*\left(K + 2\mu\right) + \mu\left(9K + 8\mu\right)} = \sum_{n=1}^{N} \frac{\mu_n^{'} - \mu}{25\mu\left(3K + 4\mu\right)} \sum_{m=1}^{M} c\left(\alpha_{m,n}\right) \cdot \left[T_{ijij}\left(\alpha_{m,n}\right) - \frac{1}{3}T_{iijj}\left(\alpha_{m,n}\right)\right]$$

$$\rho^* = \rho\left(1 - c\right) + \sum_{n=1}^{N} c_n \rho_n^{'}$$

where c_n represents the volume concentration of the nth fluid and $\alpha_{m,n}$ is the mth aspect ratio associated with the nth fluid.

The scalars T_{iijj} and T_{ijij} used are defined as

$$T_{iijj} = \frac{3F_1}{F_2}$$

$$T_{ijij} - \frac{1}{3}T_{iijj} = \frac{2}{F_3} + \frac{1}{F_4} + \frac{F_4F_5 + F_6F_7 - F_8F_9}{F_2F_4}$$

where

$$F_1 = 1 + A\left[\frac{3}{2}\left(g + \phi\right) - R\left(\frac{3}{2}g + \frac{5}{2}\phi - \frac{4}{3}\right)\right]$$

$$F_2 = 1 + A\left[1 + \frac{3}{2}\left(g + \phi\right) - \frac{R}{2}\left(3g + 5\phi\right)\right] + B\left(3 - 4R\right) + \frac{A}{2}\left(A + 3B\right)\left(3 - 4R\right)\left[g + \phi - R\left(g - \phi + 2\phi^2\right)\right]$$

$$F_3 = 1 + \frac{A}{2}\left[R\left(2 - \phi\right) + \frac{\left(1 + \alpha^2\right)}{\alpha^2}g\left(R - 1\right)\right]$$

$$F_4 = 1 + \frac{A}{4}\left[3\phi + g - R\left(g - \phi\right)\right]$$

$$F_5 = A\left[R\left(g+\phi-\frac{4}{3}\right)-g\right]+B\phi\left(3-4R\right)$$

$$F_6 = 1+A\left[1+g-R\left(g+\phi\right)\right]+B\left(1-\phi\right)\left(3-4R\right)$$

$$F_7 = 2+\frac{A}{4}\left[9\phi+3g-R\left(5\phi+3g\right)+B\phi\left(3-4R\right)\right]$$

$$F_8 = A\left[1-2R+\frac{g}{2}\left(R-1\right)+\frac{\phi}{2}\left(5R-3\right)\right]+B\left(1-\phi\right)\left(3-4R\right)$$

$$F_9 = A\left[g\left(R-1\right)-R\phi\right]+B\phi\left(3-4R\right)$$

$$A = \frac{\mu^{'}}{\mu}-1$$

$$B = \frac{1}{3}\left(\frac{K^{'}}{K}-\frac{\mu^{'}}{\mu}\right)$$

$$R = \frac{3\mu}{3K+4\mu}$$

$$\phi = \frac{\alpha}{\left(1-\alpha^2\right)^{3/2}}\left[\arccos\left(\alpha\right)-\alpha\left(1-\alpha^2\right)^{1/2}\right]$$

$$g = \frac{\alpha^2}{1-\alpha^2}\left(3\phi-2\right)$$

Appendix E

The Modified Model of Squirt-Flow Dispersion and Attenuation

E.1 Generalized Mavko-Jizba Model

Mavko and Jizba [1991] proposed a quantitative model for squirt-flow and predicted the dispersion in granular rocks. The important contributions of the work of Mavko and Jizba [1991] are the expressions for the so-called unrelaxed bulk and shear moduli of the frame, which are computed assuming the stiff pores are dry but compliant pores are filled with a fluid. However, the unrelaxed moduli go to infinity for dry or gas-saturated case, which is physically invalid. Gurevich et al. [2009b] developed alternative expressions for ultrasonic moduli using the discontinuity formalism of Sayers and Kachanov [1991], which reduce to the expressions of Mavko and Jizba [1991] for the fluid-saturated case, but are also valid for gas-saturated case. The work of Gurevich et al. [2009b] assumes a statistically continuous distribution of cracks in rocks, and takes a volume average of the whole cracks no matter the orientations or the compliance of each set of cracks. The expression linking the unrelaxed moduli of frame and the compliances of cracks are

$$\frac{1}{K_{uf}} = \frac{1}{K_h} + sB_N \tag{E.1}$$

$$\frac{1}{\mu_{uf}} = \frac{1}{\mu_h} + \frac{4}{15}sB_N + \frac{2}{5}sB_T \tag{E.2}$$

where K_{uf} and μ_{uf} are the unrelaxed bulk and shear moduli, K_h and μ_h are the dry bulk and shear moduli of a hypothetical rock without the compliant pores, B_N and B_T are the normal and shear compliance of each plane discontinuity of cracks with s surface to volume ratio of all cracks. However, assuming the binary distribution of cracks in rocks [Toksöz et al., 1976, Shapiro, 2003], we can come up with relationships from equations (E.7) and (E.8)

$$\frac{1}{K_{uf}} = \frac{1}{K_h} + \sum_i s_i B_N^i \tag{E.3}$$

$$\frac{1}{\mu_{uf}} = \frac{1}{\mu_h} + \frac{4}{15}\sum_i s_i B_N^i + \frac{2}{5}\sum_i s_i B_T^i \tag{E.4}$$

where B_N^i and B_T^i are the normal and shear compliance of the ith set of cracks with s_i surface to volume ratio. Each set of cracks is assumed statistically homogeneously distributed in rocks. Equations (E.2) to (E.8) are valid for rocks in which compliant pores are either dry or fluid-saturated. For a dry rock, we have

$$\frac{1}{K_{\text{dry}}} = \frac{1}{K_h} + \sum_i s_i B_{N,\text{dry}}^i \tag{E.5}$$

$$\frac{1}{\mu_{\text{dry}}} = \frac{1}{\mu_h} + \frac{4}{15}\sum_i s_i B_{N,\text{dry}}^i + \frac{2}{5}\sum_i s_i B_{T,\text{dry}}^i \tag{E.6}$$

where $B_{N,\text{dry}}^i$ and $B_{T,\text{dry}}^i$ are the dry normal and shear compliance of the ith set of cracks. In the fluid-saturated case, the shear stresses are negligible up to the characteristic frequency of viscous shear relaxation and shear compliance of cracks is independent of fluid, so that $B_T = B_{T,\text{dry}}$. Subtracting equation (E.1) from equation (E.3) and equation (E.2) from equation (E.4) gives

$$\frac{1}{K_{\text{dry}}} - \frac{1}{K_{uf}} = \sum_i s_i \left(B_{N,\text{dry}}^i - B_N^i\right) \tag{E.7}$$

$$\frac{1}{\mu_{\text{dry}}} - \frac{1}{\mu_{uf}} = \frac{4}{15}\sum_i s_i \left(B^i_{N,\text{dry}} - B^i_N\right) \tag{E.8}$$

Substituting equation (E.7) into equation (E.8), we still obtain the same relation for dry shear modulus $\mu_{\text{dry}}(P)$ at a given pressure P as Gurevich et al. [2009b] have in original Mavko-Jizba equation

$$\frac{1}{\mu_{\text{dry}}(P)} - \frac{1}{\mu_{uf}(P)} = \frac{4}{15}\left(\frac{1}{K_{\text{dry}}(P)} - \frac{1}{K_{uf}(P)}\right) \tag{E.9}$$

Equation (E.5) indicates that, by sequentially adding different set of dry cracks into dry frame of a hypothetical rock without the compliant pores, we actually continue updating the dry frame so as to obtain the final dry bulk modulus of the cracked rock. The contribution from the ith set of dry cracks to final dry bulk modulus of the rock is equal to $s_i B^i_{N,\text{dry}}$. We can express the equation (E.5) in an alternative way as

$$\frac{1}{K_{\text{dry}}} = \frac{1}{K_h} + \sum_{j\neq i} s_j B^j_{N,\text{dry}} + s_i B^i_{N,\text{dry}} \tag{E.10}$$

which isolate the contribution from the ith set of dry cracks. If we define $\overline{K}^i_h$, the equivalent dry bulk modulus of a hypothetical rock without including the ith set of dry cracks, as

$$\frac{1}{\overline{K}^i_h} = \frac{1}{K_h} + \sum_{j\neq i} s_j B^j_{N,\text{dry}} \tag{E.11}$$

then we can have equation (E.10) written as

$$\frac{1}{K_{\text{dry}}} = \frac{1}{\overline{K}^i_h} + s_i B^i_{N,\text{dry}} \tag{E.12}$$

Following the derivation of Gurevich et al. [2009b], we can obtain the relation for the unrelaxed bulk modulus of cracked rocks at a given pressure P,

$$\frac{1}{K_{uf}(P)} = \frac{1}{K_h} + \sum_i \frac{1}{\frac{1}{\frac{1}{K_{\text{dry}}(P)} - \frac{1}{\overline{K}^i_h}} + \frac{1}{\left(\frac{1}{K_f} - \frac{1}{K_g}\right)\phi^i_c(P)}} \tag{E.13}$$

where K_f and K_g are bulk moduli of the fluid and of the material of the solid grains, ϕ_c^i is the porosity of the ith set of compliant cracks.

With the equations (E.13) and (E.9), we can estimate the unrelaxed bulk and shear moduli of rocks where fluid fills the compliant pores but stiff pores are dry so as to take into account the squirt-flow effect. Most parameters used in these two equations can be obtained in laboratory measurement, while only the equivalent dry bulk modulus of a hypothetical rock, $\overline{K}_h^i$, needs to be estimated. Assuming we know the distribution of the binary sets of cracks in a rock and the dry bulk modulus of frame under really high pressure $P > P_h$, by adding the other jth sets of cracks into the dry frame, where $j \neq i$, we can estimated $\overline{K}_h^i$ for the ith set of cracks by the numerical computation or theoretical models such as the Kuster-Toksöz model or other effective media theories.

E.2 The Modified Squirt-Flow Model

The unrelaxed moduli derived in the previous section are high-frequency moduli. To obtain the frequency-dependent moduli due to the squirt-flow dispersion requires additional information about the compliant pores. As proposed by Murphy et al. [1986] and Gurevich et al. [2009c], we can assume a particular configuration of pore space: a compliant pore described as a disk-like gap between two grains links to a toroidal stiff pore as shown in Figure E-1. The gap has radius a and thickness h. The impact of this gap on effective elastic property is determined by the additional effective stiffness K^* of the gap due to the presence of fluid, which can be defined as

$$K^* = \frac{\triangle F}{-\triangle h} \tag{E.14}$$

where $\triangle F$ is the acoustic force exerted by fluid onto the gap wall, and $\triangle h$ is the uniaxial dynamic loading or displacement under such force. The force can be obtained by integrating the pressure over surface S_g of the gap

$$\Delta F = \int_{S_g} p\left(r\right) dS \tag{E.15}$$

For a sinusoidal loading $\triangle h \exp\left(i\omega t\right)$, the pressure developed inside gap can be obtained as a solution to the equation

$$\frac{d^2p}{dr^2} + \frac{1}{r}\frac{dp}{dr} + k^2 p = C \tag{E.16}$$

where r is radial coordinate, and k is the wavenumber defined by $k^2 = -i\omega h_0 D/K_f$, $D = 12\eta/h_0^3$ is the viscous resistance, η is dynamic viscosity of the fluid and $C = i\omega D \triangle h$. Solving the equation (E.16) with the boundary condition at the edge of the gap $p|_{r=a} = 0$, we can have solution of pressure field

$$p = \frac{C}{k^2}\left[1 - \frac{J_0\left(kr\right)}{J_0(ka)}\right] \tag{E.17}$$

Combining this solution with equations (E.14) and (E.15) leads to expression for the effective stiffness

$$K^* = \pi a^2 \left[1 - \frac{2J_1\left(ka\right)}{kaJ_0\left(ka\right)}\right] \frac{K_f}{h_0} \tag{E.18}$$

At low frequency limit $k \to 0$ and thus $K^* = 0$. However, at high frequency limit, equation (E.18) gives

$$K^* = \frac{\pi a^2}{h_0} K_f \tag{E.19}$$

This is the unrelaxed effective stiffness of gap when fluid in gap has no time to escape from the gap to stiff pore within the half-period of the wave. The effective stiffness at a given frequency in equation (E.18) is actually computed from unrelaxed effective stiffness in (E.19) for a modified fluid with a frequency dependent bulk modulus

$$K_f^* = \left[1 - \frac{2J_1\left(ka\right)}{kaJ_0\left(ka\right)}\right] K_f \tag{E.20}$$

Substituting this equivalent fluid bulk modulus into equation (E.13), we can have

the partially relaxed bulk modulus

$$\frac{1}{K_{pf}(P)} = \frac{1}{K_h} + \sum_i \frac{1}{\frac{1}{\frac{1}{K_{\text{dry}}(P)} - \frac{1}{K_h^i}} + \frac{1}{\left(\frac{1}{K_f^*} - \frac{1}{K_g}\right)\phi_c^i(P)}} \tag{E.21}$$

thus the partially relaxed shear modulus in equation (E.9) by substituting $K_{pf}(P)$ for $K_{uf}(P)$

$$\frac{1}{\mu_{\text{dry}}(P)} - \frac{1}{\mu_{pf}(P)} = \frac{4}{15}\left(\frac{1}{K_{\text{dry}}(P)} - \frac{1}{K_{pf}(P)}\right) \tag{E.22}$$

Because the equivalent fluid bulk modulus in equation (E.20) is frequency dependent, so are the partially relaxed bulk and shear moduli, which gives us the velocity dispersion and attenuation due to the squirt-flow taking place in cracks. By using either Gassmann's or Biot's equations, we can compute the saturated moduli of porous rocks which is frequency dependent as well. If the frequency is low compared with Biot's characteristic frequency, Gassmann's model is used by substituting K_{pf} for the frame modulus, while keeping μ_{pf} as the saturated shear modulus. However, if the frequency is higher than Biot's characteristic frequency, Biot's model is used instead.

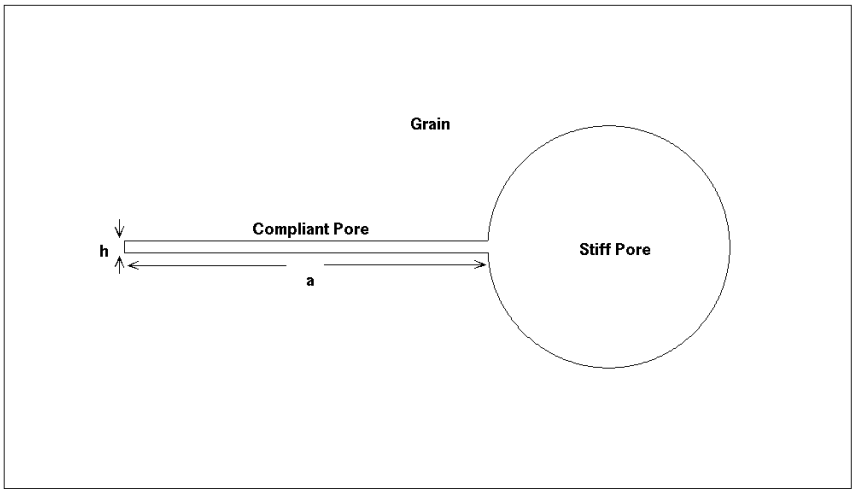

Figure E-1: Schematic configuration for the squirt-flow model: Axisymmetric section through the model.

Appendix F

Nonlinear Solver for Single Phase Viscous Fluid

Seismic propagation in porous and permeable media usually produces different particle motion in fluid and solid, the relative motion of which gives rise to seismic attenuation. At very high frequencies, motions in fluid consist of vibrations around equilibrium, while at low frequencies fluid flow takes place in pores due to the local pressure gradient. Biot [1956a, 1956b] developed a theory to study the seismic attenuation in fluid-saturated porous media at low- and high- frequencies, which considered the coupling between fluid and solid at macroscale. However, the theory underestimates the attenuation observed in real data [Nur and Simmons, 1969, Winkler, 1985, Murphy et al., 1986, Wang and Nur, 1990]. Theories to account for more seismic energy loss other than Biot's loss have been developed. Mavko and Nur [1979], O'Connell and Budiansky [1977], Murphy et al. [1986], Dvorkin and Nur [1993], Dvorkin et al. [1994, 1995] proposed a mechanism to account for the fluid flow at microscale - the "squirt-flow", where fluid is squeezed out of cracks into open pores by high pressure due to compressional waves. White [1975], Pride and Berryman [2003a,b], Pride et al. [2004] modeled the wave-induced fluid flow in model where mesoscopic heterogeneity due to lithological variations or due to patches of different immiscible fluids is considered. In this type of model, compressional waves squeeze compliant part of the media and drive fluid flow to stiff part. The wave-induced

fluid flow at different scales – "macroscopic", "mesoscopic" and "microscopic" – plays an important role in attenuating seismic wave energy. Though theoretical models can be developed to understand the effect of wave-induced fluid flow on velocity and attenuation, their applications are limited on real rocks for the sake of simplified assumptions about the geometry of porous media. Recently, with the developments of computational techniques and power, it becomes possible to numerically study the seismic wave propagating in fluid-saturated porous media with the help of digitized rocks. Saenger et al. [2005] studied Biot's effect in digitized porous rocks numerically where they used the general Maxwell model to approximate the viscous effect of fluid. However, this model only considers the Biot's effect approximately. In order to study the mechanism of seismic attenuation due to fluid flow at three different scales, a model fully coupling fluid and solid has to be developed and solved numerically on digitized rocks representing the complex pore structures of real rocks.

As discussed in Chapter 2, we have developed a coupled and unified model to govern the fluid and solid, which is able to take into account the interaction between viscous compressible fluid and solid. However, ignoring the nonlinear convection term in the Navier-Stokes equations, we have linearized the system in fluid domain, which is appropriate for fluid with small velocities induced by passing seismic wave. Linearizing the Navier-Stokes equations is an approach people have taken to study wave propagation in viscous fluid [Lighthill, 2002] and derive mathematical models for the squirt-flow phenomenon [Mavko and Nur, 1979, Murphy et al., 1986]. However, according to local velocity field, fluid particles physically move from one position to another, in which convection plays an important role, especially when velocity is large. Therefore, it is necessary to keep the convection term in numerical modeling, and leave physics to decide how much effect convection can have on the results. Actually, Greenshields and Weller [2005] kept the convection term in their modeling of pressure wave propagating in an artery, and Käser and Dumbser [2008] studied wave propagation in moving water by considering convection due to background velocity field.

In this chapter, we first review the governing equations for both fluid and solid.

Second, following the work of Käser and Dumbser [2008], we will show how to treat the convection term under the assumption of small perturbation. Then we will introduce the numerical method - upwind scheme - to handle the convection in numerical solver. Finally, we will demonstrate an example of the nonlinear solver on modeling wave propagating in moving fluid.

F.1 Governing Equations

Considering a medium consisting of a porous elastic matrix filled with a compressible Newtonian fluid, it is convenient to describe the coupled system with an unified system of governing equations. We take the classical way by using velocity-stress formulation to describe the fluid and solid domains. For wave propagating in purely elastic medium, the equations are

$$\rho_s \frac{\partial \mathbf{v}}{\partial t} = \nabla \cdot \boldsymbol{\sigma} + \mathbf{f} \tag{F.1}$$

$$\frac{\partial \boldsymbol{\sigma}}{\partial t} = \lambda \mathbf{tr}\left(\dot{\boldsymbol{\varepsilon}}\right)\mathbf{I} + 2\mu\dot{\boldsymbol{\varepsilon}} \tag{F.2}$$

$$\dot{\boldsymbol{\varepsilon}} = \frac{1}{2}\left(\nabla\mathbf{v} + (\nabla\mathbf{v})^{\mathbf{T}}\right) \tag{F.3}$$

where $\mathbf{v}$ is the velocity vector, $\boldsymbol{\sigma}$ and $\dot{\boldsymbol{\varepsilon}}$ are stress tensor and strain rate tensor, ρ_s, λ and μ are the density and Lamé elastic constants of the solid phase.

For wave propagating in viscous fluid, the equations from the fundamental equations of fluid dynamics [Landau and Lifshitz, 1959] are given by

$$\frac{\partial \rho_f}{\partial t} + \nabla \cdot (\rho_f \mathbf{v}) = 0 \tag{F.4}$$

$$\rho_f \left(\frac{\partial \mathbf{v}}{\partial t} + (\mathbf{v} \cdot \nabla)\,\mathbf{v}\right) = \nabla \cdot \boldsymbol{\sigma} + \mathbf{f} \tag{F.5}$$

$$\boldsymbol{\sigma} = -p\mathbf{I} + \boldsymbol{\tau} \tag{F.6}$$

$$\boldsymbol{\tau} = \eta_\lambda \mathbf{tr}\,(\dot{\boldsymbol{\varepsilon}})\mathbf{I} + 2\eta_\mu \dot{\boldsymbol{\varepsilon}} \tag{F.7}$$

where p and $\boldsymbol{\tau}$ are pressure and deviatoric stress tensor, ρ_f, η_μ and η_λ are the density, shear and second viscosity coefficients of the fluid phase. In both solid and fluid domain, the vector $\mathbf{f}$ is the volumetric force.

F.2 Treatment of Convection Term in Fluid Domain

As we have known that strain induced by passing seismic wave usually has magnitude of $10^{-7} - 10^{-6}$, we can assume small density, velocity, pressure and viscous stresses perturbation for acoustic wave propagating in viscous fluid. Therefore, we can introduce decompositions

$$\rho_f = \rho_{f0} + \rho_f^{'},\ \mathbf{v} = \mathbf{v_0} + \mathbf{v}^{'},\ p = p_0 + p^{'},\boldsymbol{\tau} = \boldsymbol{\tau}_0 + \boldsymbol{\tau}^{'} \tag{F.8}$$

where $\rho_f^{'}$, $\mathbf{v}^{'}$, $p^{'}$ and $\boldsymbol{\tau}^{'}$are small density, velocity, pressure and viscous stresses perturbations corresponding to background density ρ_{f0}, velocity $\mathbf{v_0}$, pressure p_0 and viscous stresses $\boldsymbol{\tau}_0$. Under assumption of small perturbation, perturbations of these quantities are much smaller than the background state, i.e., $\rho_f^{'} \ll \rho_{f0}$, $p^{'} \ll p_0$.

Furthermore, for the case we are interested in, seismic wave length is much larger than pore space of porous rocks. Hence, we can assume that the background fluid in pores is incompressible, i.e., ρ_{f0} is constant in space and time. According to the conservation of mass in equation (F.4), this leads to

$$\nabla \cdot \mathbf{v}_0 = 0 \tag{F.9}$$

First we need to derive partial differential equation for perturbed pressure field $p^{'}$. Expanding equation (F.4), we can have

$$\frac{\partial \rho_f}{\partial t} + \mathbf{v} \cdot \nabla \rho_f + \rho_f \nabla \cdot \mathbf{v} = 0 \tag{F.10}$$

Based on these assumptions, we can simplified the conservation equation (F.4) with the help of equations (F.8) and (F.9). Note that under such small perturbation assumptions, quantities of the fluctuations are so small that their products can be ignored. After some mathematical manipulations, we can obtain

$$\frac{\partial \rho_f^{'}}{\partial t} + \mathbf{v} \cdot \nabla \rho_f^{'} + \rho_{f0} \nabla \cdot \mathbf{v}^{'} = \mathbf{0} \tag{F.11}$$

For an isentropic fluid, pressure perturbation $p^{'}$ can be linked to perturbation of density $\rho_f^{'}$ by equation of state [Landau and Lifshitz, 1959]

$$p^{'} = c_p^2 \rho_f^{'} \tag{F.12}$$

where c_p is wave speed in fluid, and defined as

$$c_p^2 = \frac{K}{\rho_f} \tag{F.13}$$

where K is the bulk modulus of fluid.

Using equation (F.8), neglecting $\rho_f^{'}$ against ρ_{f0}, and substituting equation (F.12) into equation (F.11), we have the final equation for the pressure perturbation

$$\frac{\partial p^{'}}{\partial t} + \mathbf{v} \cdot \nabla p^{'} + K \nabla \cdot \mathbf{v}^{'} = \mathbf{0} \tag{F.14}$$

From equation (F.14), we can see that this degrades back to pressure equation for linear acoustic wave propagation as in equation (2.6) if the second term, convection term, is ignored.

Second, we need to derive the governing equation for velocity perturbation $\mathbf{v}^{'}$. Because of the existence of a background state, we actually assume it satisfies

$$\frac{\partial \mathbf{v_0}}{\partial t} + (\mathbf{v_0} \cdot \nabla)\, \mathbf{v_0} = -\frac{\nabla p_0}{\rho_0} + \frac{1}{\rho_0} \nabla \cdot \boldsymbol{\tau}_0 \tag{F.15}$$

Using assumptions in equation (F.8) and substituting equation (F.15) into equation (F.5), we can simplify the governing equation

$$\frac{\partial \mathbf{v}^{'}}{\partial t} + (\mathbf{v} \cdot \nabla)\, \mathbf{v}^{'} = -\frac{\nabla p^{'}}{\rho_0} + \frac{1}{\rho_0} \nabla \cdot \boldsymbol{\tau}^{'} + \mathbf{f} - \left(\mathbf{v}^{'} \cdot \nabla\right) \mathbf{v_0} \tag{F.16}$$

from which we can see an additional source term $\left(\mathbf{v}^{'} \cdot \nabla\right) \mathbf{v_0}$ is introduced. For small velocity perturbation or constant (or zero) background velocity field, we can drop out the source term in equation (F.19), which gives

$$\frac{\partial \mathbf{v}^{'}}{\partial t} + (\mathbf{v} \cdot \nabla)\, \mathbf{v}^{'} = -\frac{\nabla p^{'}}{\rho_0} + \frac{1}{\rho_0} \nabla \cdot \boldsymbol{\tau}^{'} + \mathbf{f} \tag{F.17}$$

Through these mathematical manipulations, the movement of fluid, or fluid convection, is preserved via fluid velocity in $\mathbf{v} \cdot \nabla p^{'}$ and $(\mathbf{v} \cdot \nabla)\, \mathbf{v}^{'}$, respectively. For cases starting with initial state where $v_0 = p_0 = \boldsymbol{\tau}_0 = 0$, we have $v = v^{'}$, $p = p^{'}$ and $\boldsymbol{\tau} = \boldsymbol{\tau}^{'}$. Hence, equations (F.11) and (F.17) can be further simplified as

$$\frac{\partial p^{'}}{\partial t} + \mathbf{v}^{'} \cdot \nabla p^{'} + K \nabla \cdot \mathbf{v}^{'} = \mathbf{0} \tag{F.18}$$

$$\frac{\partial \mathbf{v}^{'}}{\partial t} + \left(\mathbf{v}^{'} \cdot \nabla\right) \mathbf{v}^{'} = -\frac{\nabla p^{'}}{\rho_0} + \frac{1}{\rho_0} \nabla \cdot \boldsymbol{\tau}^{'} + \mathbf{f} \tag{F.19}$$

Combining equations (F.18) and (F.19) with equation (F.7), we finally obtain a close system of equations with which we can describe the fluid dynamics in viscous fluid domain.

F.3 Upwind Scheme for Solving Convection

Adequate numerical methods to solve advection equation have been studied for many years in fluid/gas dynamics so as to accurately handle shocks or other discontinuities existing in solutions [e.g., Godunov, 1959, van Leer, 1979, Roe, 1981, Harten, 1983, Toro, 1997]. Pursuing high order accuracy of the numerical scheme is always the effort researchers aim at, especially if sharp discontinuities present. The most

recent development is the WENO scheme [Harten et al., 1987, Shu and Osher, 1988, 1989, Shu et al., 1992], which achieves 5th order accuracy in space. As for our problem of wave propagating in viscous fluid, generally smooth wave field is generated. Hence, scheme with lower order accuracy should be applicable. Within these available schemes, upwind scheme [LeVeque, 2007] is the better one to use because it is so easy to implement and the computational cost is low.

In general, an advection equation has the basic form as in equations (F.18) and (F.19) as

$$\frac{\partial \mathbf{v}}{\partial t} + (\mathbf{v} \cdot \nabla)\, \mathbf{v} = 0 \tag{F.20}$$

in which information of $\mathbf{v}$ is carried with velocity $\mathbf{v}$ itself and evolves in time. Because the velocity $\mathbf{v}$ is a vector, the motion itself under the control of convection is asymmetric. Depending on the direction of motion, information should move accordingly.

To approximate the $(\mathbf{v} \cdot \nabla)\, \mathbf{v}$ in equation (F.20), upwind scheme uses one-sided finite difference scheme. Depending on direction of local velocity field, it might choose backward or forward finite differencing. As an example, we only consider 2D case where $\mathbf{v}(x, z) = (u(x, z), w(x, z))$. For velocity component u in x direction, equation (F.20) becomes

$$\frac{\partial u}{\partial t} + u u_x + w u_z = 0 \tag{F.21}$$

Asymmetric approximation to u_x can be

$$D_x^+ u \approx \frac{U_{i+1,j} - U_{i,j}}{\Delta x} \tag{F.22}$$

$$D_x^- u \approx \frac{U_{i,j} - U_{i-1,j}}{\Delta x} \tag{F.23}$$

where Δx is the spacing between finite difference grid, $U_{i,j}$ is the discrete values of u approximated in finite difference, and D_x^+ and D_x^- are forward and backward differencing operators, respectively. The same rules apply to spatial derivative of u

in z direction

$$D_z^+ u \approx \frac{U_{i,j+1} - U_{i,j}}{h} \tag{F.24}$$

$$D_z^- u \approx \frac{U_{i,j} - U_{i,j-1}}{h} \tag{F.25}$$

As we can see that, if $u > 0$, the solution moves to positive direction along x, while if $u < 0$ it moves to the negative direction. In the same way, solution moves to positive direction along z if $w > 0$, while if $w < 0$ it moves to negative direction as well. It is best to acknowledge these asymmetry by using one-sided difference in the appropriate directions. Coupling one of these approximations with forward differencing in time, we can have methods for solving the advection equation

$$U_{i,j}^{n+1} = U_{i,j}^n - \Delta t \left[\left(\left[U_{i,j}^n \right]^+ D_x^- u + \left[U_{i,j}^n \right]^- D_x^+ u \right) + \left(\left[W_{i,j}^n \right]^+ D_z^- u + \left[W_{i,j}^n \right]^- D_z^+ u \right) \right] \tag{F.26}$$

where $U_{i,j}^n$ and $W_{i,j}^n$ are velocity of (u, w) on grid (i, j) at time step n, and also we define

$$\left[U_{i,j}^n \right]^+ = \max \left(U_{i,j}^n, 0 \right)$$

$$\left[U_{i,j}^n \right]^- = \min \left(U_{i,j}^n, 0 \right)$$

$$\left[W_{i,j}^n \right]^+ = \max \left(W_{i,j}^n, 0 \right)$$

$$\left[W_{i,j}^n \right]^- = \min \left(W_{i,j}^n, 0 \right)$$

Besides the Courant-Friedrichs-Lewy (CFL) stability criterion we have to satisfy, equation (F.26) has to satisfy another stability condition to make it stable only if

$$\left|\frac{\max(u,w)\cdot\Delta t}{\Delta x}\right| < 1 \tag{F.27}$$

To extend this into 3D case, we only need to work on direction y in the same fashion. Nothing much complicated will be involved at end.

F.4 Numerical Example

To demonstrate the capability of our nonlinear solver on solving wave propagation in moving fluid, we take the classical 2D test as did Käser and Dumbser [2008]. As shown in Figure F-1, the 2D model consists of two homogeneous fluid and solid half-spaces where the viscous fluid half-space is on top of an elastic solid half-space with a plane interface. A compressional point source is excited in fluid domain. A snapshot of the velocity component w is plotted at time $t = 0.185$s in Figure F-2a for case of the fluid at rest where $v_0 = 0$ m/s. We can clearly see (a) direct and (b) reflect acoustic wave in fluid, and (c) transmitted P-wave and (d) converted S-wave in solid. Along interface, clear refracted head wave (e) and (f) are generated, and Scholte wave (g) can be observed as well. Compared to the symmetric pattern of wave field in Figure F-2a, the wave field developed in case of the moving fluid with $u_0 = 500$ m/s is asymmetric due to the motion of fluid as shown in Figure F-2b.

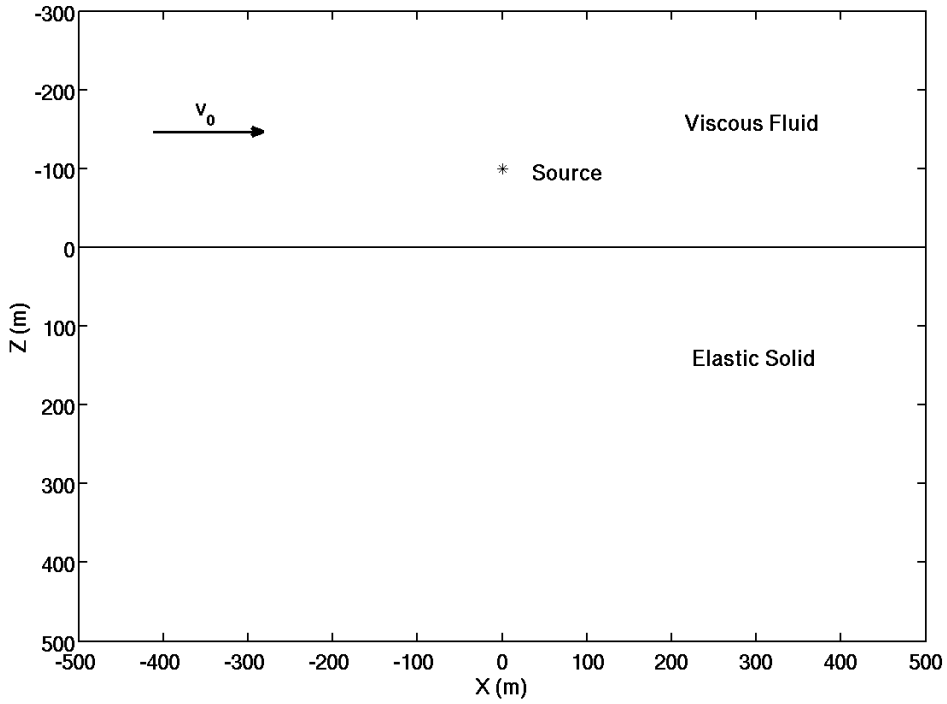

Figure F-1: A 2D model consists of two homogeneous fluid and solid half-spaces.

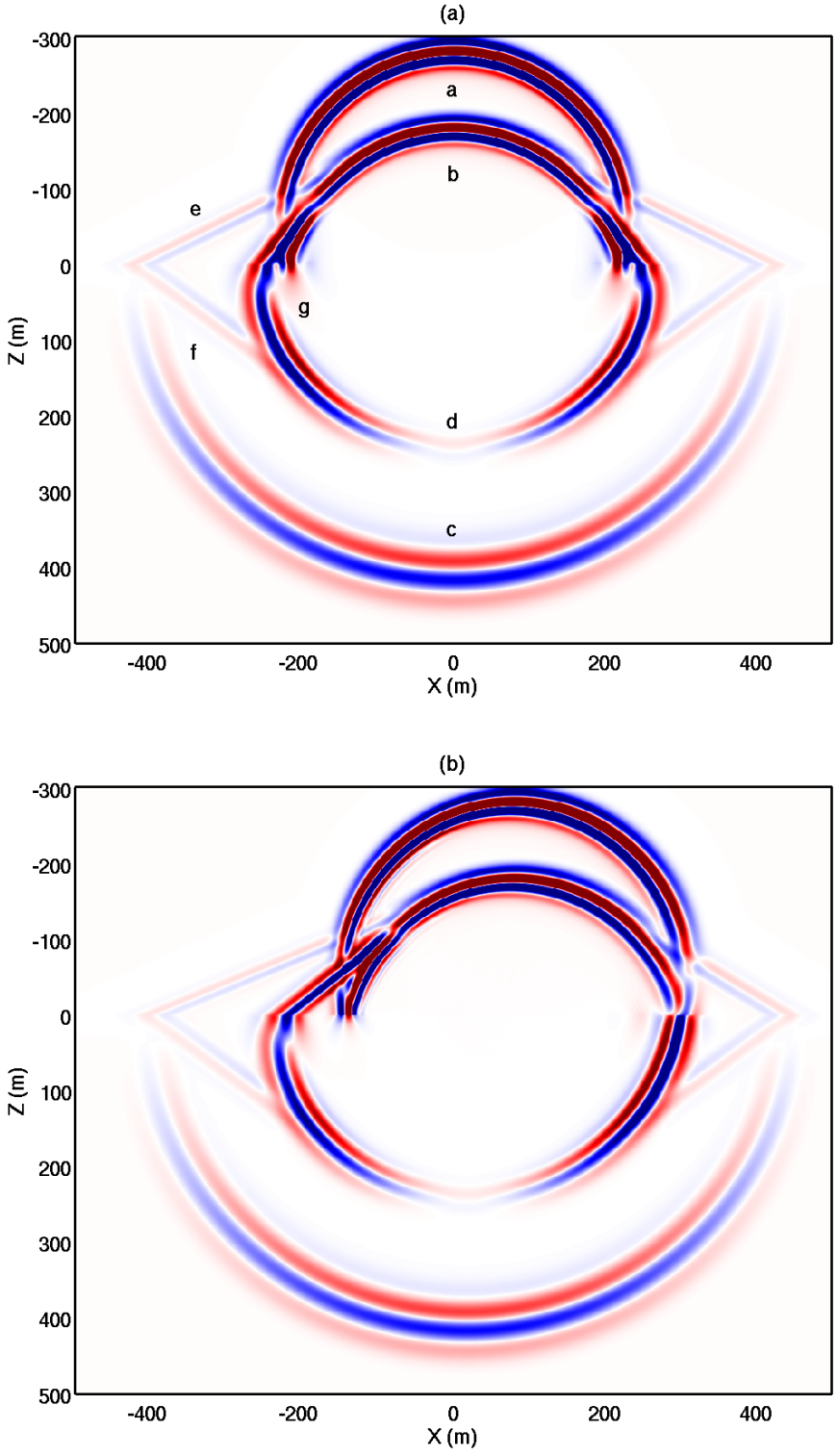

Figure F-2: Snapshot of the velocity component w at time $t = 0.185$ s. (a) fluid is at rest ($v_0 = 0$ m/s); (b) fluid is moving with $u_0 = 500$ m/s.

Bibliography

L Adam, M Batzle, and I Brevik. Gassmann's fluid substitution and shear modulus variability in carbonates at laboratory seismic and ultrasonic frequencies. *Geophysics*, 71(6):F173–F183, NOV-DEC 2006. ISSN 0016-8033. doi: 10.1190/1.2358494.

CH Arns. *The influence of morphology on physical properties of reservoir rocks*. PhD thesis, University of New South Wales,Sydney, Australia, 2002.

CH Arns, MA Knackstedt, WV Pinczewski, and EJ Garboczi. Computation of linear elastic properties from microtomographic images: Methodology and agreement between theory and experiment. *Geophysics*, 67(5):1396–1405, SEP-OCT 2002. ISSN 0016-8033. doi: 10.1190/1.1512785.

CH Arns, M Madadi, AP Sheppard, and MA Knachstedt. Linear elastic properties of granular rocks derived from X-ray CT images. *SEG Expanded Abstract*, pages 1711–1714, 2007.

FM Auzerais, J Dunsmuir, BB Ferreol, N Martys, J Olson, TS Ramakrishnan, DH Rothman, and LM Schwartz. Transport in sandstone: A study based on three dimensional microtomography. *Geophysical Research Letters*, 23(7):705–708, APR 1 1996. ISSN 0094-8276.

ML Batzle, DH Han, and R Hofmann. Fluid mobility and frequency-dependent seismic velocity - Direct measurements. *Geophysics*, 71(1):N1–N9, JAN-FEB 2006. ISSN 0016-8033. doi: 10.1190/1.2159053.

JG Berryman. Single-scattering approximations for coefficients in Biot equations of poroelasticity. *Journal of The Acoustical Society of America*, 91(2):551–571, FEB 1992. ISSN 0001-4966.

JG Berryman and HF Wang. The elastic coefficients of double-porosity models for fluid transport in jointed rock. *Journal of Geophysical Research-Solid Earth*, 100 (B12):24611–24627, DEC 10 1995. ISSN 0148-0227.

JG Berryman and HF Wang. Elastic wave propagation and attenuation in a double-porosity dual-permeability medium. *International Journal of Rock Mechanics and Mining Sciences*, 37(1-2):63–78, JAN-FEB 2000. ISSN 0148-9062.

AI Best and C Mccann. Seismic attenuation and pore-fluid viscosity in clay-rich reservoir sandstones. *Geophysics*, 60(5):1386–1397, SEP-OCT 1995. ISSN 0016-8033.

MA Biot. Theory of propagation of elastic waves in a fluid saturated porous solid. I. Low frequency range. *Journal of The Acoustical Society of Amecia*, 28(2):168–178, 1956a. ISSN 0001-4966.

MA Biot. Theory of propagation of elastic waves in a fluid saturated porous solid. II. High frequency range. *Journal of The Acoustical Society of Amecia*, 28(2):179–191, 1956b. ISSN 0001-4966.

LM Brekhovskikh. *Waves in Layered Media.* Academic, New York, 1981.

J Carcione. *Wave fields in real media: Wave propagation in anisotropic, inelastic and porous media.* Pergamon Press, 2001.

R Ciz, EH Saenger, and B Gurevich. Pore scale numerical modeling of elastic wave dispersion and attenuation in periodic systems of alternating solid and viscous fluid layers. *Journal of The Acoustical Society of Amecia*, 120(2):642–648, AUG 2006. ISSN 0001-4966. doi: 10.1121/1.2216687.

J Dvorkin and A Nur. Dynamic poroelasticity: A unified model with the squirt and the Biot mechanisms. *Geophysics*, 58(4):524–533, APR 1993. ISSN 0016-8033.

J Dvorkin, R Nolenhoeksema, and A Nur. The squirt-flow mechanism: Macroscopic description. *Geophysics*, 59(3):428–438, MAR 1994. ISSN 0016-8033.

J Dvorkin, G Mavko, and A Nur. Squirt flow in fully saturated rocks. *Geophysics*, 60(1):97–107, JAN-FEB 1995. ISSN 0016-8033.

H Emmerich and M Korn. Incorporation of attenuation into time-domain computations of seismic wave fields. *Geophysics*, 52(9):1252–1264, SEP 1987. ISSN 0016-8033.

BP Flannery, HW Deckman, WG Roberge, and KL Damico. 3-D X-ray microtomography. *Science*, 237(4821):1439–1444, SEP 18 1987. ISSN 0036-8075.

JT Fredrich, B Menendez, and TF Wong. Imaging the pore structure of geomaterials. *Science*, 268(5208):276–279, APR 14 1995. ISSN 0036-8075.

RJ Galvin and B Gurevich. Interaction of an elastic wave with a circular crack in a fluid-saturated porous medium. *Applied Physics Letters*, 88(6), FEB 6 2006. ISSN 0003-6951. doi: 10.1063/1.2165178.

RJ Galvin and B Gurevich. Scattering of a longitudinal wave by a circular crack in a fluid-saturated porous medium. *International Journal of Solids and Structures*, 44 (22-23):7389–7398, NOV 2007. ISSN 0020-7683. doi: 10.1016/j.ijsolstr.2007.04.011.

RJ Galvin and B Gurevich. Effective properties of a poroelastic medium containing a distribution of aligned cracks. *Journal of Geophysical Research-Solid Earth*, 114, JUL 15 2009. ISSN 0148-0227. doi: 10.1029/2008JB006032.

EJ Garboczi. Finite element and finite difference programs for computing the linear electric and linear elastic properties of digital images of random materials. Technical report, National Institute of Standards and Technology, 1998.

EJ Garboczi and AR Day. Algorithm for computing the effective linear elastic properties of heterogeneous materials - 3-D results for composites with equal phase Poisson ratios. *Journal of The Mechanics and Physics of Solids*, 43(9):1349–1362, SEP 1995. ISSN 0022-5096.

CG Giannopapa and G Papadakis. Linear stability analysis and application of a new solution method of the elastodynamic equations suitable for a unified fluid-structure-interaction approach. *Journal of Pressure Vessel Technology*, 130(3): 031303–1–8, AUG 2008. ISSN 0094-9930. doi: 10.1115/1.2937764. Pressure Vessels and Piping Conference of the American-Society-of-Mechanical-Engineers, Denver, CO, JUL 17-21, 2005.

SK Godunov. A defference scheme for numerical computation of discontinuous solutions of equations of fluid dynamics. *Mathematics Sbornik*, 47:271–306, 1959.

RB Gordon and LA Davis. Velocity and attenuation of seismic waves in imperfectly elastic rock. *Journal of Geophysical Research*, 73(12):3917–3935, 1968. ISSN 0148-0227.

V Grechka and M Kachanov. Effective elasticity of rocks with closely spaced and intersecting cracks. *Geophysics*, 71(3):D85–D91, 2006.

CJ Greenshields and HG Weller. A unified formulation for continuum mechanics applied to fluid-structure interaction in flexible tubes. *International Journal for Numerical Methods in Engineering*, 64(12):1575–1593, NOV 28 2005. ISSN 0029-5981. doi: 10.1002/nme.1409.

B Gurevich. Effect of fluid viscosity on elastic wave attenuation in porous rocks. *Geophysics*, 67(1):264–270, JAN-FEB 2002. ISSN 0016-8033.

B Gurevich and S Lopatnikov. Elastic attenuation in nonhomogeneous porous materials. In *Soil Dynamics and Earthquake Engineering V*, pages 235–247, 1991. ISBN 1-85312-153-3.

B Gurevich, VB Zyrianov, and SL Lopatnikov. Seismic attenuation in finely layered porous rocks: Effects of fluid flow and scattering. *Geophysics*, 62(1):319–324, JAN-FEB 1997. ISSN 0016-8033. Workshop on Effective Media Concepts for Seismic Wave Propagation, KARLSRUHE, GERMANY, JAN 22-23, 1995.

B Gurevich, O Kelder, and DMJ Smeulders. Validation of the slow compressional wave in porous media: Comparison of experiments and numerical simulations. *Transport in Porous Media*, 36(2):149–160, AUG 1999. ISSN 0169-3913.

B Gurevich, K Osypov, R Ciz, and D Makarynska. Modeling elastic wave velocities and attenuation in rocks saturated with heavy oil. *Geophysics*, 73(4):E115–E122, JUL-AUG 2008. ISSN 0016-8033. doi: 10.1190/1.2940341.

B Gurevich, M Brajanovski, RJ Galvin, TM Muller, and J Toms-Stewart. P-wave dispersion and attenuation in fractured and porous reservoirs - poroelasticity approach. *Geophysical Prospecting*, 57(2):225–237, MAR 2009a. ISSN 0016-8025. doi: 10.1111/j.1365-2478.2009.00785.x.

B Gurevich, D Makarynska, and M Pervukhina. Ultrasonic moduli for fluid-saturated rocks: Mavko-Jizba relations rederived and generalized. *Geophysics*, 74(4):N25–N30, JUL-AUG 2009b. ISSN 0016-8033. doi: 10.1190/1.3123802.

B. Gurevich, D. Makarynska, M. Pervukhina, and O. B. De Paula. A new squirt-flow model for elastic wave attenuation and dispersion in fluid-saturated rocks. In Ling, HI and Smyth, A and Betti, R, editor, *Poro-Mechanics IV*, pages 700–705, 2009c. ISBN 978-1-60595-006-8. 4th Biot Conference on Poromechanics, New York, NY, JUN 08-10, 2009.

DH Han. *Effects of porosity and clay content on acoustic properties of sandstones and unconsolidated sediments: Ph.D. thesis.* PhD thesis, Stanford University, 1986.

A Harten. High resolution schemes for hyperbolic conservation laws. *Journal of Computational Physics*, 49(3):357–393, 1983. ISSN 0021-9991.

A Harten, B Engquist, S Osher, and SR Chakravarthy. Uniformly high order accurate essentially non-oscillatory schemes .III. *Journal of Computational Physics*, 71(1): 231–303, FEB 1987. ISSN 0021-9991.

JA Hudson. Overall properties of a cracked solid. *Mathematical Proceedings of The Cambridge Philosophical Society*, 88(SEP):371–384, 1980. ISSN 0305-0041.

DH Johnston and MN Toksöz. Ultrasonic P and S wave attenuation in dry and saturated rocks under pressure . *Journal of Geophysical Research*, 85(NB2):925–936, 1980. ISSN 0148-0227.

DH Johnston, MN Toksöz, and A Timur. Attenuation of seismic-waves in dry and saturated rocks. 2. Mechanisms. *Geophysics*, 44(4):691–711, 1979. ISSN 0016-8033.

T Jones and A Nur. Velocity and attenuation in sandstone at elevated temperatures and pressures. *Geophysical Research Letter.*, 10(2):140–143, 1983. ISSN 0094-8276.

J Khazanehdari and J Sothcott. Variation in dynamic elastic shear modulus of sandstone upon fluid saturation and substitution. *Geophysics*, 68(2):472–481, MAR-APR 2003. ISSN 0016-8033. doi: 10.1190/1.1567213.

MA Knackstedt, S Latham, M Madadi, A Sheppard, T Varslot, and CH Arns. Digital rock physics: 3D imaging of core material and correlations to acoustic and flow properties. *The Leading Edge*, 28(1):28–33, 2009. doi: 10.1190/1.3064143.

M Käser and M Dumbser. A highly accurate discontinuous Galerkin method for complex interfaces between solids and moving fluids. *Geophysics*, 73(3):T23–T35, MAY-JUN 2008. ISSN 0016-8033. doi: 10.1190/1.2870081.

GT Kuster and MN Toksöz. Velocity and attenuation of seismic-waves in two-phase media: Part I. Theoretical formulation. *Geophysics*, 39(5):587–606, 1974. ISSN 0016-8033.

LD Landau and EM Lifshitz. *Fluid Mechnics*. Pergamon Press, 1959.

RJ LeVeque. *Finite difference methods for ordinary and partial differential equations: Steady-state and time-dependent problems*. SIAM, 2007.

J Lighthill. *Waves in fluids*. Cambridge University Press, 2002.

M Madadi, AC Jones, CH Arns, and MA Knackstedt. 3D imaging and simulation of elastic properties of porous materials. *Computing in Science & Engineering*, 11(4): 65–73, JUL-AUG 2009. ISSN 1521-9615.

G Marketos and AI Best. Application of the BISQ model to clay squirt flow in reservoir sandstones. *Journal of Geophysical Research-Solid Earth*, 115, JUN 23 2010. ISSN 0148-0227. doi: 10.1029/2009JB006495.

YJ Masson and SR Pride. Poroelastic finite difference modeling of seismic attenuation and dispersion due to mesoscopic-scale heterogeneity. *Journal of Geophysical Research -Solid Earth*, 112(B3):B03204, MAR 13 2007. ISSN 0148-0227. doi: 10.1029/2006JB004592.

YJ Masson and SR Pride. Finite-difference modeling of Biot's poroelastic equations across all frequencies. *Geophysics*, 75(2):N33–N41, 2010. doi: 10.1190/1.3332589.

YJ Masson, SR Pride, and KT Nihei. Finite difference modeling of Biot's poroelastic equations at seismic frequencies. *Journal of Geophysical Research -Solid Earth*, 111 (B10):B10305, OCT 14 2006. ISSN 0148-0227. doi: 10.1029/2006JB004366.

G Mavko and D Jizba. Estimating grain-scale fluid effects on velocity dispersion in rocks. *Geophysics*, 56(12):1940–1949, DEC 1991. ISSN 0016-8033.

G Mavko and A Nur. Melt squirt in asthenosphere. *Journal of Geophysical Research*, 80(11):1444–1448, 1975. ISSN 0148-0227.

G Mavko, T Mukerji, and J Dvorkin. *The rock physics handbook*. Cambridge University Press, 1998.

GM Mavko and A Nur. Wave attenuation in partially saturated rocks. *Geophysics*, 44(2):161–178, 1979. ISSN 0016-8033.

B McKavanagh and FD Stacey. Mechanical hysteresis in rocks at low strain amplitudes and seismic frequencies. *Physics of The Earth and Planetary Interiors*, 8(3): 246 – 250, 1974. ISSN 0031-9201. doi: DOI:10.1016/0031-9201(74)90091-0.

TM Müller, B Gurevich, and SA Shapiro. Attenuation of Seismic Waves Due to Wave-Induced Flow and Scattering in Randomly Heterogeneous Poroelastic Continua. In Renata Dmowska, editor, *Earth Heterogeneity and Scattering Effects on Seismic Waves*, volume 50 of *Advances in Geophysics*, pages 123 – 166. Elsevier, 2008. doi: doi:10.1016/S0065-2687(08)00005-8.

TM Muller and B Gurevich. Wave-induced fluid flow in random porous media: Attenuation and dispersion of elastic waves. *Journal of the Acoustical Society of America*, 117(5):2732–2741, MAY 2005. ISSN 0001-4966. doi: 10.1121/1.1894792.

WF Murphy. Effects of partial water saturation on attenuation in massilon sandstone and vycor porous-glass. *Journal of the Acoustical Society of America*, 71(6):1458–1468, 1982. ISSN 0001-4966.

WF Murphy. Acoustic measures of partial gas saturation in tight sandstones. *Journal of Geophysical Research*, 89(NB13):1549–1559, 1984. ISSN 0148-0227.

WF Murphy, KW Winkler, and RL Kleinberg. Acoustic relaxation in sedimentary rocks: Dependence on grain contacts and fluid saturation. *Geophysics*, 51(3):757–766, 1986. doi: 10.1190/1.1442128.

A Nur and G Simmons. The effect of viscosity of a fluid phase on velocity in low porosity rocks. *Earth and Planetary Science Letters*, 7(2):99–108, 1969. ISSN 0012-821X.

RJ O'Connell and B Budiansky. Viscoelastic properties of fluid-saturated cracked solids. *Journal of Geophysical Research*, 82(36):5719–5735, 1977. ISSN 0148-0227.

L Peselnick and WF Outerbridge. Internal friction in shear and shear modulus of solenhofen limestone over a frequency range of 10 to seventh power cycles per second. *Journal of Geophysical Research*, 66(2):581–588, 1961. ISSN 0148-0227.

WH Press, SA Teukolsky, WT Vetterling, and BP Flannery. *Numerical Recipes in C*. Cambridge University Press, London, 1992.

SR Pride and JG Berryman. Linear dynamics of double-porosity dual-permeability materials. I. Governing equations and acoustic attenuation. *Physical Review E*, 68 (3, Part 2), SEP 2003a. ISSN 1063-651X. doi: 10.1103/PhysRevE.68.036603.

SR Pride and JG Berryman. Linear dynamics of double-porosity dual-permeability materials. II. Fluid transport equations. *Physical Review E*, 68(3, Part 2), SEP 2003b. ISSN 1063-651X. doi: 10.1103/PhysRevE.68.036604.

SR Pride, JG Berryman, and JM Harris. Seismic attenuation due to wave-induced flow. *Journal of Geophysical Research-Solid Earth*, 109(B1), JAN 14 2004. ISSN 0148-0227. doi: 10.1029/2003JB002639.

AP Roberts and EJ Garboczi. Elastic properties of model porous ceramics. *Journal of The American Ceramic Society*, 83(12):3041–3048, DEC 2000. ISSN 0002-7820.

PL Roe. Approximate Riemann solvers, parameter vectors, and difference schemes. *Journal of Computational Physics*, 43(2):357–372, 1981. ISSN 0021-9991.

JG Rubino, CL Ravazzoli, and JE Santos. Equivalent viscoelastic solids for heterogeneous fluid-saturated porous rocks. *Geophysics*, 74(1):N1–N13, JAN-FEB 2009. ISSN 0016-8033. doi: 10.1190/1.3008544.

EH Saenger and SA Shapiro. Effective velocities in fractured media: a numerical study using the rotated staggered finite-difference grid. *Geophysical Prospecting*, 50(2):183–194, MAR 2002. ISSN 0016-8025.

EH Saenger, N Gold, and SA Shapiro. Modeling the propagation of elastic waves using a modified finite-difference grid. *Wave Motion*, 31(1):77–92, JAN 2000. ISSN 0165-2125.

EH Saenger, OS Kruger, and SA Shapiro. Effective elastic properties of randomly fractured soils: 3D numerical experiments. *Geophysical Prospecting*, 52(3):183–195, MAY 2004a. ISSN 0016-8025.

EH Saenger, OS Kruger, and SA Shapiro. Numerical considerations of fluid effects on wave propagation: Influence of the tortuosity. *Geophysical Research Letters*, 31 (21), NOV 13 2004b. ISSN 0094-8276. doi: 10.1029/2004GL020970.

EH Saenger, SA Shapiro, and Y Keehm. Seismic effects of viscous Biot-coupling: Finite difference simulations on micro-scale. *Geophysical Research Letters*, 32(14): L14310, JUL 26 2005. ISSN 0094-8276. doi: 10.1029/2005GL023222.

EH Saenger, OS Krueger, and SA Shapiro. Effective elastic properties of fractured rocks: Dynamic vs. static considerations. *International Journal of Fracture*, 139 (3-4):569–576, JUN 2006. ISSN 0376-9429. doi: 10.1007/s10704-006-0105-4.

EH Saenger, R Ciz, OS Krueger, SM Schmalholz, B Gurevich, and SA Shapiro. Finite-difference modeling of wave propagation on microscale: A snapshot of the work in progress. *Geophysics*, 72(5, Suppl. S):SM293–SM300, SEP-OCT 2007. ISSN 0016-8033. doi: 10.1190/1.2753552.

Erik H. Saenger. Numerical methods to determine effective elastic properties. *International Journal of Engineering Science*, 46(6):598–605, JUN 2008. ISSN 0020-7225. doi: 10.1016/j.ijengsci.2008.01.005.

CM Sayers and M Kachanov. A simple technique for finding effective elastic constants of cracked solids for arbitrary crack orientation statistics. *International Journal of Solids and Structures*, 27(6):671–680, 1991. ISSN 0020-7683.

LM Schwartz, F Auzerais, J Dunsmuir, N Martys, DP Bentz, and S Torquato. Transport and diffusion in three-dimensional composite media. *Physica A*, 207(1-3): 28–36, JUN 1 1994. ISSN 0378-4371. 3rd International Conference on Electrical Transport and Optical Properties of Inhomogeneous Media (ETOPIM 3), GUANAJUATO, MEXICO, AUG 09-13, 1993.

SA Shapiro. Elastic piezosensitivity of porous and fractured rocks. *Geophysics*, 68 (2):482–486, MAR-APR 2003. ISSN 0016-8033. doi: 10.1190/1.1567215.

CW Shu and S Osher. Efficient implementation of essentially non-oscillatory shock capturing schemes. *Journal of Computational Physics*, 77(2):439–471, AUG 1988. ISSN 0021-9991.

CW Shu and S Osher. Efficient implementation of essentailly non-oscillatory shock capturing scheme. II. *Journal of Computational Physics*, 83(1):32–78, JUL 1989. ISSN 0021-9991.

CW Shu, TA Zang, G Erlebacher, D Whitaker, and S Osher. High-order ENO schemes applied to two- and three-dimensional compressible flow. *Applied Numerical Mathematics*, 9(1):45–71, JAN 1992. ISSN 0168-9274.

P Spanne, JF Thovert, CJ Jacquin, WB Lindqust, KW Jones, and PM Adler. Synchrotron computed microtomography of porous-media - Topology and transports. *Physical Review Letters*, 73(14):2001–2004, OCT 3 1994. ISSN 0031-9007.

ES Sprunt and WF Brace. Direct observation of microcavities in crystalline rocks. *International Journal of Rock Mechanics and Mining Sciences*, 11(4):139–150, 1974. ISSN 0148-9062.

BR Tittmann. Internal-friction measurements and their implications in seismic Q structure models of crust. *Transactions-American Geophysical Union*, 58(8):826, 1977. ISSN 0002-8606.

MN Toksöz and DH Johnston. *Seismic wave attenuation*. 2. Society of Exploration Geophysics, 1981.

MN Toksöz, CH Cheng, and A Timur. Velocities of seismic waves in porous rocks. *Geophysics*, 41(4):621–645, 1976. ISSN 0016-8033.

MN Toksöz, DH Johnston, and A Timur. Attenuation of seismic-waves in dry and saturated rocks. 1. Laboratory measurements. *Geophysics*, 44(4):681–690, 1979. ISSN 0016-8033.

EF Toro. *Riemann solvers and numerical methods for fluid dynamics, a practical introduction*. Springer-Verlag,Berlin, 1997.

Bram van Leer. Towards the ultimate conservative difference scheme. V. A second-order sequel to Godunov's method. *Journal of Computational Physics*, 32(1):101–136, 1979. ISSN 0021-9991. doi: DOI:10.1016/0021-9991(79)90145-1.

J Virieux. P-SV wave propagation in heterogeneous media: Velocity-stress finite-difference method. *Geophysics*, 51(4):889–901, 1986. doi: 10.1190/1.1442147.

JB Walsh. Effect of cracks on the compressibility of rock. *Journal of Geophysical Research*, 70(2):381–389, 1965. ISSN 0148-0227.

ZJ Wang and A Nur. Dispersion analysis of acoustic velocities in rocks. *Journal of the Acoustical Society of America*, 87(6):2384–2395, JUN 1990. ISSN 0001-4966.

ZJ Wang, WK Hirsche, and G Sedgwick. Seismic velocities in carbonates rocks. *Journal of Canadian Petroleum Technology*, 30(2):112–122, MAR-APR 1991. ISSN 0021-9487.

JE White. Computed seismic speeds and attenuation in rocks with partial gas saturation. *Geophysics*, 40(2):224–232, 1975. ISSN 0016-8033.

K Winkler and A Nur. Pore fluids and seismic attenuation in rocks. *Geophysical Research Letters*, 6(1):1–4, 1979a. ISSN 0094-8276.

K Winkler and A Nur. Attenuation and velocity in dry and water-saturated massilon sandstone. *Geophysics*, 44(3):336, 1979b. ISSN 0016-8033.

K Winkler, A Nur, and M Gladwin. Friction and seismic attenuation in rocks. *Nature*, 277(5697):528–531, 1979. ISSN 0028-0836.

KW Winkler. Frequency dependent ultrasonic properties of high-porosity sandstones. *Journal of Geophysical Research*, 88(NB11):9493–9499, 1983. ISSN 0148-0227.

KW Winkler. Dispersion analysis of velocity and attenuation in Berea sandstone. *Journal of Geophysical Research*, 90(NB8):6793–6800, 1985. ISSN 0148-0227.

KW Winkler. Estimates of velocity dispersion between seismic and ultrasonic frequencies. *Geophysics*, 51(1):183–189, JAN 1986. ISSN 0016-8033.

KW Winkler and A Nur. Seismic attenuation - Effects of pore fluids and frictional sliding. *Geophysics*, 47(1):1–15, 1982. ISSN 0016-8033.

KW Winkler and TJ Plona. Technique for measuring ultrasonic velocity and attenuation spectra in rocks under pressure. *Journal of Geophysical Research*, 87(NB13): 776–780, 1982. ISSN 0148-0227.

MRJ Wyllie, AR Gregory, and LW Gardner. Elastic wave velocities in heterogeneous and porous media. *Geophysics*, 21(1):41–70, 1956. doi: 10.1190/1.1438217.

MRJ Wyllie, AR Gregory, and GHF Gardner. An experimental investigation of factors affecting elastic wave velocities in porous media. *Geophysics*, 23(3):459–493, 1958. doi: 10.1190/1.1438493.